Outstanding properties of epitaxial graphene grown from silicon carbide substrate

by

Amira Ben Gouider Trabelsi

Thesis

Submitted in partial fulfillment of the requirements for the award of

Doctor of Philosophy of Loughborough University

© by **Amira Ben Gouider Trabelsi**
(2018)

To my Mother

Title: Outstanding properties of epitaxial graphene grown from silicon carbide substrate

Abstract

In this thesis a study of outstanding properties of epitaxial graphene on SiC were carried out involving Raman spectroscopy, AFM, UFM, XPS, Photoelectric effect and electrical resistivity.

Epitaxial graphene was grown from a semi-insulating on-axis 6H (000-1) or 4H-SiC (000-1) substrate. Epitaxial growth is based on Si atoms sublimation from the SiC substrate bulk. We used the basics of epitaxial graphene growth; however small details were changed. This allowed the growth of various layers, new features and new properties.

X-ray photoelectron spectroscopy ‘‘XPS’’ was used to identify the different components forming within the graphene – substrate system. The graphene layer number is evidenced by XPS. Atoms percentages in the grown graphene layer were determined. Furthermore, the oxidation of the graphene layers was clearly distinguished.

Atomic force microscopy “AFM” was carried out to study the topography response of the graphene sample. This distinguishes any morphological changes of the graphene layer. The size, orientation and regularity of the layers terraces were determined. For the first time, new features such as: island, bubbles and domes of graphene layers were identified. The nature of these features was determined using ultra force microscopy “UFM”.

High-resolution micro-Raman (Jobin Yvon HR LabRAM) was employed to illustrate all the revealed properties. Nonetheless, it illustrates the doping, defects, disorder, number of layers and phonon-plasmon coupling of epitaxial graphene. These properties were carefully demonstrated based on local Raman mapping.

The findings of these investigations indicate the formation of various types of epitaxial graphene layers. These latest could have various forms with new electrical properties. This was illustrated using a comparative study to mechanical properties of epitaxial graphene island. In fact, new charge distribution was found across these features. These findings also differs from other electrical properties found in flat graphene layers. These latest shows

electroneutrality of charge distribution between graphene – SiC substrate. Here, Phonons-plasmons coupling in epitaxial graphene – SiC substrate system were illustrated. On other hand, epitaxial graphene properties were not limited to the graphene layers flatness. In fact, new photoresponse of epitaxial graphene under violet light was revealed. Here, photo resistance increase during to epitaxial graphene morphology.

Acknowledgements

I wish to thank my supervisor Professor. Feodor V Kusmartsev for his excellent guidance during the course of the project and his precious help through all the stages of my research, his support has by far exceeded my expectations.

I would also like to thank Dr Marat Gaifullin for supporting me and provided me with advice to succeed and fulfil my research. Also, I would thank him for the long hours of help in Lab. I extend my thanks to Dr Olga Kusmartseva for her tremendous help and advice, without her continuous effort my research could not have been conducted.

I am particularly grateful to Dr Anna Kusmarseva for her valued assistance. Thanks to be address to Mikael Forester for his support during my PhD and collaboration. Also, thanks for Brian Dennis and Phil Sutton for the technical assistance and support with the Lab.

Many thanks to my mother, my father, my sister and brother for their love and support which stays an eternal debt for me. Not to forget my friends Dr Samir El Khawaja and his Familly, Dr Nebil and his family, Amjaad and her Mum, Hana, Sara and Ann in Loughborough for their encouragement and help.

Introduction……………………………………………………………………………..14
Chapter 1: Epitaxial graphene properties………………………………….…18
I- Introduction ……………………………………………………………………19
II- Fundamental properties of graphene ………………………..……………..20
II-1- Crystal structure…………………………………..……………………...20
II-2- Electronic Structure…………………………………..………………..21
❖ Exceptional behaviour at the vicinity of K and K'……….………23
❖ Half-integer quantum Hall effect………………………………....26
II-3- Mechanical properties of graphene………………………………………27
II-4- Vibrational properties ………………………………......…………..….27
II-5- Photoeffect……………………………………………………………...…28
III- Epitaxial graphene……………………………………………………..……29
III-1- Silicon carbide (SiC) substrate……………..…………………………..29
III-1-1- SiC structural properties ………………………………………….30
III-1-2-Applications………………………………..…………………...31
III-2- Graphitization from SiC…………………………………………..………32
III-2-1 Graphene on SiC face terminated Si……………………...……..32
❖ Structural properties ………………………………………….....32
❖ 6R3-SiC phase properties……………………………………33
❖ Epitaxial growth of carbon layers……………………………34
❖ Electronic structure……………………………………………34
❖ Transport properties…………………………………………35
III-2-2- Graphene on SiC face terminated C: SiC ………………36
❖ Structural properties…………………………………………36
❖ Electronic properties…………………………………………36
❖ Transport properties of the system………………….………37
IV- Applications………………………………………………………………37
V- conclusion…………………………………………..…………………………38
References :……………………………………………………………………………39
Chapter II: Characterization technique……………………………………..43
I- Introduction………………………………………………………………………44

II- Graphene surface analysis……………………………………..………………44
1 optical microscopy…………………………………..…………………………44
2- Atomic Force Microscopy (AFM)…………………………….…………………45
II-2- 1 Principle of the AFM………………………….……………………45
3- Ultrasonic force microscopy (UFM)………………………………………………47
II-3-1- Principle of the UFM…………………………………...………47
4- Raman Spectroscopy……………………………………………………………48
II-4-1- Principal……………………………………..…………….48
❖ Classical description of the Raman phenomenon………………..…………………………….………………49
❖ The quantum mechanical description of the Raman ……………………………………………………49
a- First order Raman effect……………………………………...51
b- Second order Raman effect……………………………………53
c- Raman polarization effect……………………….……………..53
d- Experimental set up……………………….…………………..54
II-5- Photoelectric effect…………………………………………………………………56
II-5-1- Principal……………………………………………………………56
II-5-2- Experimental set up……………………………..………………57
III- Conclusion…………………………………………………………………………57
References:……………………………………………………………………………..58
Chapter 3: Graphene Localisation: Mechanical and electrical properties variation …………………………..……………………………………………60
I- Introduction……………………………….………..………………………………..61
II- Raman spectra...61
1- Silicon Carbide…………………………………………………….................61
❖ SiC polytypes 61
❖ Raman Spectrum of SiC..61
2- Graphene Raman spectra……………………………………..………………62
III- Mechanical properties investigation...64
1- Epitaxial graphene macro-island...64
2- Strain distribution analysis……………………………………………….…………66

3- Strain effect……………………………………………………………………..………67

3-1- Temperature effect on a formation of strain in epitaxial graphene ……………………………………………………………………………..69

3-2- Estimation of the strain effect on graphene modes………………..……….70

IV- Electrical properties...75

1- Surface morphology: epitaxial graphene nano-domes and macro-bubbles…………………………………………………………………….75

❖ AFM measurements..75

❖ UFM measurements……………………………………………..….77

V- EGS properties……………………………………………………………........79

1- Raman mapping Localisation of EGS..79

2- Capacitor effect on epitaxial graphene bubble…..........................…………..82

3- Charge distribution in epitaxial graphene bubbles..82

4- Quantum capacitance…………...84

VI- Conclusion…..……..…87

References……...……...88

Chapter 4 : Phonons plasmons coupling……………………………….…….…92

I- Introduction……………………………………………………………………....93

II- Plasma in the solid state: characteristic and property…………………..…93

1- Low coupling……………………………………………………………..………93

1-1Screening Length...95

1-2 Plasma Frequency…………………………………………………………95

1-3 Dielectric Function…………………………………………………………96

III- Inelastic scattering and plasmons…………………………………………..97

1- Diffusion of light by electron plasmas in semiconductors……………………..…98

1-1 Dynamic structure factor……………………………………..…………….99

1-2 Phonon-plasmon coupling……………………………………….…………99

IV- Study of the substrate-graphene interface………………………………101

1- Raman spectroscopy investigation……………………………………….…..101

2- Phonon - Plasmon couplings…………………………………………………102

3. Graphene self-doping…………………………………………………...…..107

V- Conclusion………………………………………………………………..……..109

References..110
Chapter 5: Epitaxial graphene new photo-responses in the visible domain..113
I- Introduction..113
II- Epitaxial graphene contamination: oxidation and defects localisation..113
1- XPS measurements..113
2- Atomic Force Microscopy..116
3- Raman mapping investigation..118
III- Photo response of epitaxial graphene..119
1- Epitaxial graphene photoresistance "EGP"..119
2- Effect interpretation..121
3- Temperature Dependent Resistance Measurements..125
4- Photovoltage "PV"..126
5- Magnetic dependence of photo resistance decay..127
IV- Conclusions..129
References 130
Conclusion..132
Publications List..135

Introduction

Introduction

Nano materials are captivating from the fundamental point of view. Particularly, graphene ranks highly as a promising material. Graphene has exceptional electron transport properties such as the "pseudo-relativistic" nature of quasi-particles near the Fermi level. Its quantum effects or those related to the object surface may dominate the system behavior. This affects its physical, optical, electrical and mechanical properties. Graphene appears as a material of choice for future electronic and optic applications, including conventional components such as high frequency analogue devices, and devices in emerging fields such as spintronics, terahertz oscillators, and single-molecule gas sensors [1].

In this frame comes our research. From theoretical point of view graphene was already known since 1947 via PR Wallace studies [1]. However, its growth dates from 2004. This was based mainly on two methods: graphite exfoliation and graphitization of silicon carbide crystal (SiC). A third method, Chemical vapor deposition (CVD), was developed later in 2007. These approaches have revealed the fundamental aspects of this material. Our work, beginning immediately after the first experimental achievements, had a goal of probing epitaxial graphene properties changes under specific conditions. This is based on a comparative study to ideal graphene properties and ordinary epitaxial graphene. This may open door for future applications.

The present manuscript consists of five chapters. The first is a general introduction to epitaxial graphene. We present the different physical properties of epitaxial graphene. We also recalled the polarity effect on the grown epitaxial graphene from silicon carbide substrate.

In the second chapter, we will detail the main surface characterization techniques used in this thesis. These characterization techniques are mainly: conventional optical microscopy, Raman spectroscopy, Atomic Force Microscopy "AFM", Ultrasonic Force Microscopy "UFM". On other hands, we present photo-effect. Through some theoretical background, we will see their relevance, and highlight their potency and limitations in relation to the magnitude of the layer of graphene (≈ A °, which is of the order of the size of a carbon atom). Indeed, the information provided to the carbon planes of the characterization in terms of numbers, shapes and dimensions.

For the third chapter, we will be interested in Raman spectroscopy. Indeed, Raman spectroscopy remains a powerful tool for rapid and non-destructive characterization of different materials such as silicon carbide. In particular, this characterization technique ensured the analysis of the different properties of graphene as: defects, the number of layers,

the stress effect. Particularly, we will show the relevance of this technique in distinguishing epitaxial graphene properties. Indeed, based on Raman mappings, we located for the first time epitaxial graphene layers. We identified the change of mechanical or electrical properties associated to localisation of epitaxial graphene.

In the fourth chapter, we recall the basic concepts of plasma physics in the solid state and explain their role in the creation of capacity effect to graphene - substrate interface. We present some characteristics of plasma in the solid state such as the plasma frequency and the dielectric constant. Principally, we studied the inelastic scattering of light by plasmas in semiconductors. We investigate phonon - plasmon coupling in graphene - silicon carbide "SiC" substrate interface. Indeed, we revealed a new non destructive technique in determining the density of charge.

In the fifth chapter, for the first time, we discussed new photo responses in epitaxial graphene grown on 6H-SiC face terminated carbon (6H-SiC (000-1)). We have examined epitaxial graphene photoresistance light illumination. We specify the particular wavelength inducing new photoresponse such as; photovoltage and photo resistance. We argue the localised new photoresponse using a wide range of measurement techniques were used: X-ray photoelectron spectrometry, atomic force microscopy, Raman spectroscopy, and magneto-photoresistance decay analyses. Also, we investigated magnetic effect to demonstrate our found.

References:

[1] P.R. Wallace, Phys. Rev., 71, 622, (1947).

Chapter 1:

Epitaxial graphene properties

I. Introduction

Carbon "C" is a chemical element with atomic number Z (Z = 6). In the ground state, the electronic configuration of its electrons is written C = $1s^2$ $2s^2$ $2p^2$. The electrons of an atom are distributed in different orbital according to an increasing energy order, first filling the low energy orbital. The valence electrons of carbon are located around a nucleus on two quantum levels (n = 2). The two electrons of the 1s state are formed with the nucleus of the carbon atom. The electronic structure of the last energy level of the carbon atom comprises two electrons paired on the 2s level and two single electrons on the 2p level. The electron of the orbital p may have different orientations, in all directions of space. The orbital p can take three different directions correspond respectively to m = -1, 0, +1, where we denote the axis of these three orientations in the space P_x, P_y, P_z.

In the presence of numerous carbon atoms, the initial wave functions combine linearly and form hybrid orbital. These orbital differ from those of an isolated carbon atom. Indeed, the four valence electrons form four covalent bonds one bond σ and three bonds Π with the nearest carbon atoms [1]. This provides the carbon atoms structures of different dimensions having various physical and chemical properties. This gives rise to three types of hybridization defining a large family of crystals defined from the mixture of the wave functions of these four. These hybridizations are respectively sp^1, sp^2, sp^3, defined by:

- sp^1: the 2s orbital mixes with one of a single 2p orbital (2px, 2py, 2pz).
- sp^2: the 2s orbital mixes with two 2p orbital (2px 2py, 2px 2pz, 2py 2pz).
- sp^3: the 2s orbital mixes with three 2p orbital.

For graphene it is sp^2 hybridization, where the orbital of the two atoms form four new sp^2 orbital [2]. Three of these orbital are arranged in trigonal way in the plane px, py forming in between an angle of 120 °. While the fourth link is oriented in the pz direction perpendicular to the plane px, py (Figure 1).

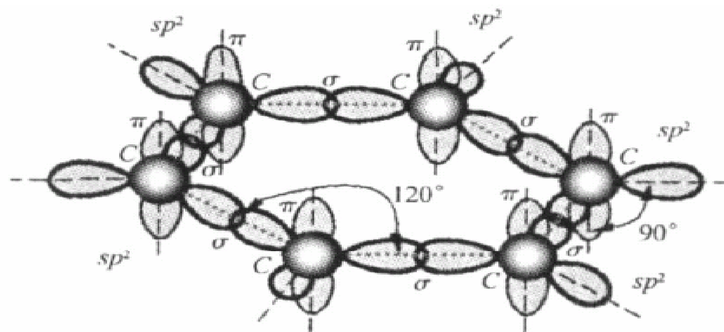

Figure 1: Illustration of sp^2 hybridization in graphene involving an s orbital with P_x and P_y orbital [2].

In this chapter, we describe the structural, optical and electrical properties of epitaxial graphene as well as its applications.

II- Fundamental properties of graphene

Graphene is the latest allotropes of the carbon family "C" [3]. It is a single graphite plane, where the carbon atoms are arranged in a honeycomb latices (Figure 2). Graphene is characterized with specific structural and electronic properties. It presnts the only two-dimensional form of carbon allotropes. In fact, the existence of two-dimensional crystals contradicts with the harmonic approximation defined at a temperature " T " greater than absolute zero given the destruction of order at great distances by thermal fluctuations. Thus, all two-dimensional system is thermodynamically unstable. This assumption verified by Landau and Peirls shows that ideal graphene can not exist [4, 5]. Actually, the existence of a two-dimensional system requires a three-dimensional space. This last could exist based on the undulation of the graphene layer as well as the substrates underneath which both provide a stability to the structural. This condition is experimentally verified by graphene which justifies its existence.

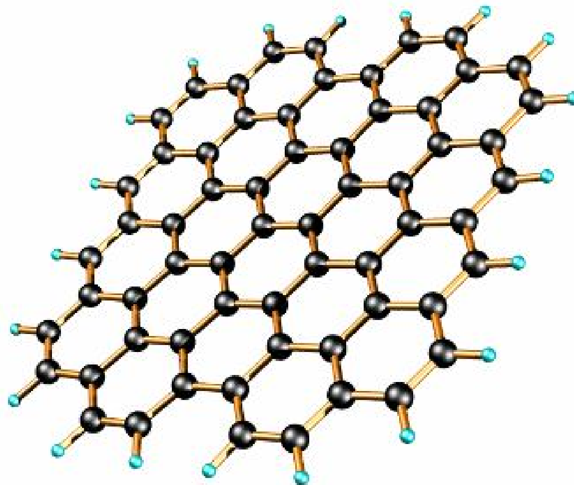

Figure 2: Graphene layer structure [3].

II-1- Crystal structure

The graphene Bravais lattice is hexagonal. The carbon atoms occupy the top of regular hexagons. This network is formed by both A and B carbon atoms per unit cell. This could be considered as a combination of two hexagonal sub arrays A and B forming a crystal

honeycomb structure (Figure 3-a). The unit cell vectors are given by Equation (1.1). The distance separating two successive carbon atoms "a" is in the range of 1.42A ° (a≈1.42A °). Graphene lattice parameter equals. The vectors connecting an A atom with its three nearest neighbor atoms B are given by equation (1.2).

$$\vec{a}_1 = \frac{a}{2}(\sqrt{3},3), \vec{a}_2 = \frac{a}{2}(-\sqrt{3},3) \tag{1.1}$$

$$\vec{b}_1 = \frac{a}{2}(\sqrt{3},1), \vec{b}_2 = \frac{a}{2}(-\sqrt{3},1), \vec{b}_3 = a(0,-1) \tag{1.2}$$

Unit cell vectors of the reciprocal network and can be determined by the relations:

$$\vec{a}_1^{\,*}\vec{a}_1 = 2\Pi \quad , \quad \vec{a}_2^{\,*}\vec{a}_2 = 2\Pi \tag{1.3}$$

$$\vec{a}_1^{\,*}\vec{a}_2 = \vec{a}_2^{\,*}\vec{a}_1 = 0 \tag{1.4}$$

Thus, the reciprocal lattice vectors are given by the following expressions:

$$\vec{c}_1 = \frac{2\Pi}{3a}(\sqrt{3},1) \quad , \quad \vec{c}_2 = \frac{2\Pi}{3a}(-\sqrt{3},1) \tag{1.5}$$

Vectors $\vec{c}_1$ and $\vec{c}_2$ define the first hexagonal Brillouin zone of reciprocal space. The two high symmetry points K and K' have none equivalent wave vectors in the first Brillouin zone (Figure 3-b).

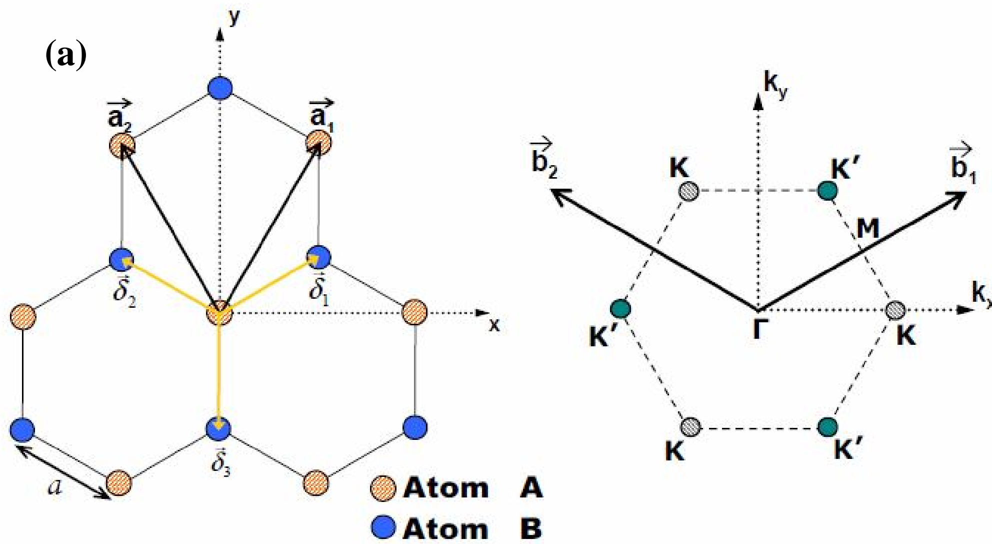

Figure 3: a- The Bravais lattice, **b-** The first Brillouin zone of ideal graphene [6] .

II-2- Electronic Structure

Carbon atoms forming graphene layer are sp^2-hybridized. This ensures the cohesion of the graphene sheet in honeycomb structure. The orbitals are characterised with an angle of 120 ° in the plane facing the first three nearest neighbors. They combined with those of neighboring sites to create the σ (binding) and σ * (anti binding) bond respectively (see, figure 1). The fourth valence electron filled half of p_z orbital forming an angle of 90 ° with the graphene plane. The recovery of these p_z orbitals form a Π and Π * bond which is weak comparing to σ bond (see, figure 2). These binding ‘’ Π and Π *’’ ensure the cohesion between the different sheets of graphene forming graphite and reflect the unique electronic properties of graphene. Although the Mermin-Wagner theorem shows the instability of two-dimensional structures [7], stability of graphene is provided by medium corrugations of 1/2 nanometers high by 5 nanometers in length.

One of the simple methods determining the band structure of graphene remains the tight-binding model. This approximation is based on the strong localization of the electron orbitals around atomic sites. The collection of electronic wave functions is adequate to correct to the representation of isolated atoms. However, this is still not enough to validate the atomic description. For graphene an accurate description could be determined using the field of energy. The Hamiltonian "H" of a total periodic crystal in the neighborhood of each node in the network is similar to that of a single atom "H_{at}". Thus, the bound levels of the atomic Hamiltonian are well located and the crystal of the Schrödinger equation is:

$$H_{at} \quad \Psi_k(r) = E_0(k) \quad \Psi_k(r) \tag{1.6}$$

Taking in concern the orbital overlap corrections in the Hamiltonian expression, we obtain a new equation (1.7). These corrections affect the entire nuclear potential by checking the periodicity of the total potential of the crystal. Thus, the wave function "$\Psi_k(r)$" must be small but non-zero [8] to check the Schrödinger equation of the atomic crystal given by:

$$H \quad \Psi_k(r) = E(k) \quad \Psi_k(r) \tag{1.7}$$

To determine the electron dispersion relation in graphene, we need to take into account the contribution of the site atoms A as well as the site atoms B respectively. This neglecting recoveries between different orbitals and considering that atoms A and B atoms constituting graphene are similar (carbon atoms). Here, we limit our study to the first nearest neighbor. Thus, we neglect the contributions of the other terms defined from farest neighbor interaction. The jump parameter of carbon atom in site A (B) and its closest neighbors B (A) is equal to t

(R) = t = 2.8eV. However, the second and third nearest neighbors is t '=0.1ev and t"= 0.07ev respectively [9]. This define both of the bands of energy of the crystal expression given bellow:

$$E_{\pm}(\vec{k}) = E_0 \pm |t| \sqrt{1 + 4\cos^2(k_x \frac{a}{2}) + 4\cos(k_x \frac{a}{2})\cos(\frac{\sqrt{3}}{2} k_y a)} \qquad (1.8)$$

Wallace was the first to find this equation in 1947 as part of the study of the band structure of the graphite [10]. Figure 4 describe the band structure of graphene in the first Brilloiun area along the [K K' Γ M] directions. The particularity of graphene as given by equation (1.8) common in these bands Π and Π * that touch at K and K', respectively, where a linear behavior of the dispersion equation was observed. This unique behavior makes graphene a semiconductor and semi-metal at the same time. Hence the name of zero-gap semiconductor was attributed to graphene [11-15].

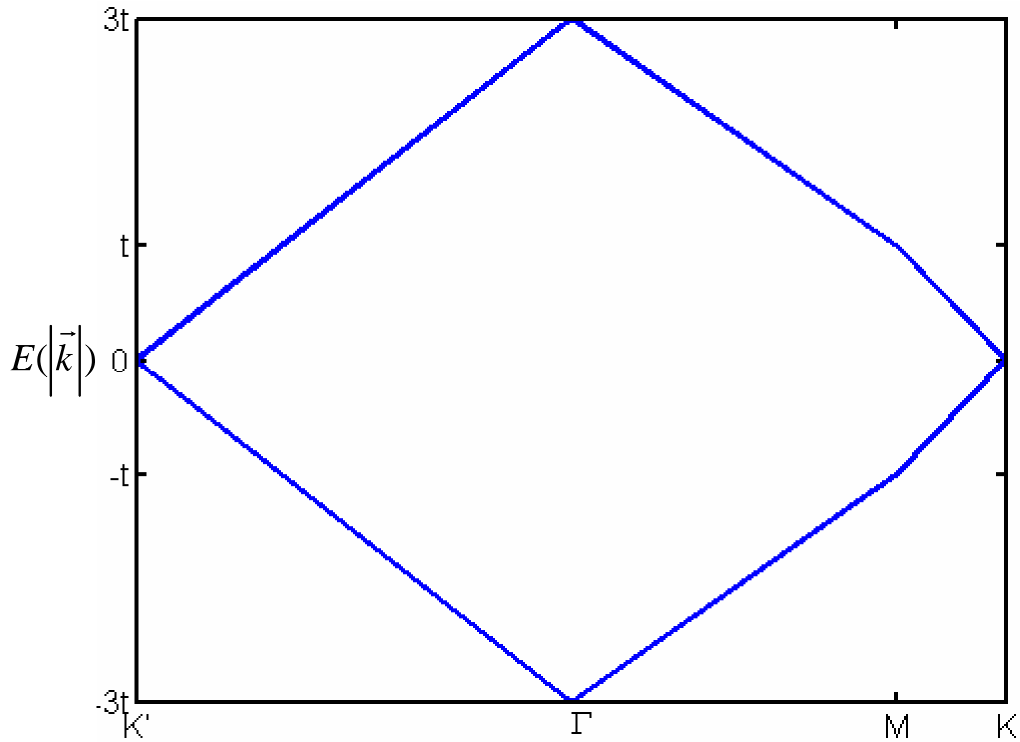

Figure 4: Graphene band structure.

❖ Exceptional behaviour at the vicinity of K and K'

For undoped graphene the Fermi level is located in the energy E = 0. The contact points between the Dirac cones are located on six points denoted K and K 'of the first Brillouin zone. All K points are physically equivalent since we can go from one point to another by a reciprocal lattice vector, which is also true for K ' [16]. Nevertheless, the only difference between these points K and K ' is the global term of phase which is involved in the

Hamiltonian without changing the system properties. The bands of energy around these issues have a particular shape, where the points K and K' are appointed valleys due to the behavior of electrons around these points and that takes the name in English valleytronic. We define these two points K and K '

$$K = \frac{2\Pi}{a}\left(\frac{2}{3}, 0\right) \quad , \quad K' = \frac{2\Pi}{a}\left(-\frac{2}{3}, 0\right) \tag{1.9}$$

The study of the system behavior near these points allows the determination of energy in the valleys. Due to the similarities of K and K', we limit ourselves to the point K. Thus, the energy at this point is given by

$$E_{\pm}(\vec{k}) = E_0 \pm |t| \sqrt{1 + 4\cos^2(k_x \frac{a}{2}) + 4\cos(k_x \frac{a}{2})\cos(\frac{\sqrt{3}}{2} k_y a)} \text{ , avec } E_0 = 0,\ k_x = \frac{4\Pi}{3a},\ k_y = 0 . \tag{1.10}$$

$$E_{\pm}(\vec{k}) = \pm |t| \sqrt{(1 + 4\cos\left(\frac{2\Pi}{3}\right) + 4\cos^2\left(\frac{2\Pi}{3}\right))} = 0 \tag{1.11}$$

The - (+) are assigned to the Π valence band (the conduction band Π *) assigned to the holes (electrons) band.

The p_z orbital of graphene are half filled. These results in an energy band which can be completely empty or full. Thus, the Fermi surface becomes reducible by these two points in the first Brillouin zone. Here, the dispersion relation of electrons near the Fermi level can be given by a Taylor expansion of the first order and the energy is expressed in terms of the group velocity in the following form

$$v_F = \frac{1}{\hbar}\frac{\partial E}{\partial p} = \pm \frac{1}{\hbar}\frac{\sqrt{3}}{2} a\ t \tag{1.12}$$

Graphene is characterized by a different energy proportional $|p|$ to that of free electron which is proportional to p^2 reflecting the peculiarity of graphene. This energy depends only on the norm of the vector ($\vec{k}$ ($|\vec{k}|$)). Thus, the Hamiltonian can be written

$$H = \begin{pmatrix} 0 & k_x - ik_y \\ k_x + ik_y & 0 \end{pmatrix} \tag{1.13}$$

Here, a phase factor shift could be considered using pseudo-spin σ defined by $\sigma = (\sigma_x, \sigma_y)$, where σ_x and σ_y are the Pauli matrices. We found correspondingly the Hamiltonian K of a massless Dirac fermions (which is also true for K')

$$H = hv_F \ (\sigma_x k_x + \sigma_y k_y) \ , \tag{1.14}$$

Where $\sigma_x = \begin{pmatrix} 0 & 1 \\ 1 & 0 \end{pmatrix}$, $\sigma_y = \begin{pmatrix} 0 & -i \\ i & 0 \end{pmatrix}$

The Hamiltonian expression is similar to that of relativistic massless fermions. Thus, the dispersion equation in the vicinity of K is

$$E_{\pm}(\vec{k}) = \pm\hbar\, v_F \left|\vec{k}\right| \tag{1.15}$$

Equation (1.15) shows spectra of linear energy around the points K and K'. This is very a unique behavior for graphene, where the relativistic kinetic energy is similar to a Dirac equation for mass less fermions. In fact, the expression of the relativistic kinetic energy is given by $E = \sqrt{p^2c^2 + m_0^2c^4}$, where E is the energy of a relativistic particle, particle mass m, p the momentum and c is the speed of light. For a massless particle the energy can be written E = ± pc, this equation is similar to (1.15). Thus, graphene quasi particle behaves as massless relativistic particle. The movement of electrons in graphene is described by the relativistic Dirac equation

$$(i\hbar\frac{\partial}{\partial t} + i\hbar c\alpha\nabla - \beta mc^2)\ \Psi(r,t) = 0 \tag{1.16}$$

Where, the Fermi velocity of graphene is equal $v_F \approx c/300 \approx 10^6 m/s$. This describes the spectrum of the quasi particles of graphene at the vicinity of the Fermi level in the Dirac cone. Hence, the electrons in graphene are characterized by different behavior from those in metals and semiconductors, where the energy spectrum is given by a parabolic dispersion relation (Figure 5).

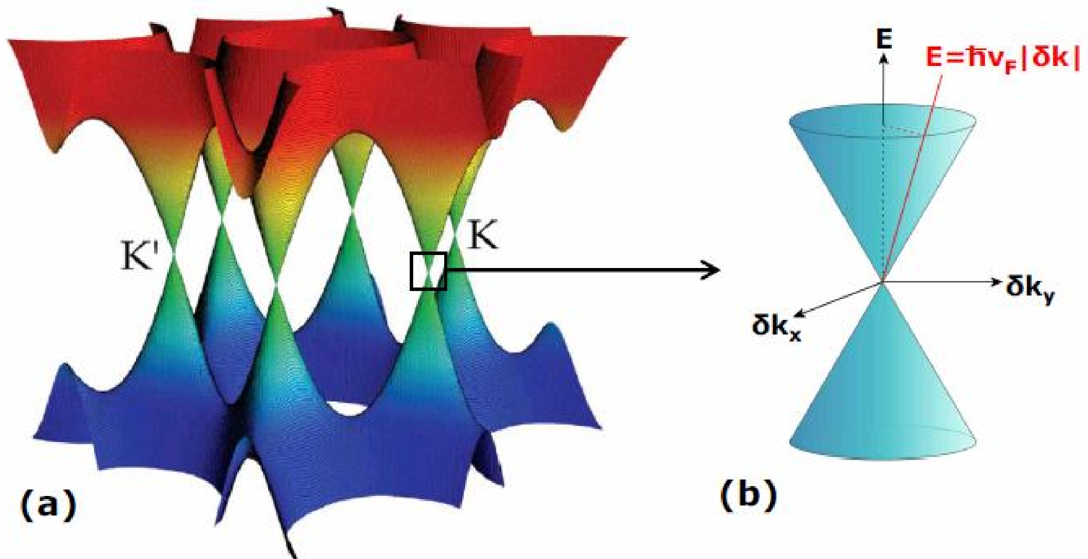

Figure 5: Band structure of ideal graphene obtained by Tight-binding approximation: dispersion band of Π and Π * [6].

❖ **Half-integer quantum Hall effect**

Quantum Hall effect appears for two-dimensional electron gas under strong magnetic fields and low temperatures. Experimentally, it is the quantification of the Hall conductivity "σ_H" in integer multiple of the quantum of conductance. The bi-dimensional gas expression is given by equation (1.17), where e is the elementary charge and the degeneration of the system g (g = 2 to degeneration due to spin electrons). This effect arises from the Landau levels whose electron state density appears under the effect of a magnetic field applied perpendicularly to the gas of two-dimensional electrons. Generally, the energy spectrum of these levels is given by the equation (1.18), where c = e B = m pulse cyclotron. Here, B is the magnetic field, m corresponds to the electron mass m and n is an integer.

$$\sigma_H = \pm n \frac{ge^2}{h} \quad (1.17)$$

$$E_n = \pm \hbar \omega_c (n + \frac{1}{2}) \quad (1.18)$$

For graphene the energy distribution of the Landau levels is different from that discussed previously (equation 1.19). We notice a variation in $\sqrt{n}$ and not in n for the energy of the Landau levels. This can induce a non-regular spacing of energy levels. Thanks to this peculiarity of the variation of the energy in $\sqrt{n}$, there appears a linear dispersion in cone of Dirac. Moreover, we notice the appearance of a Landau level of zero energy (n = 0) signature of the electron chirality's in graphene. These symmetry effects observed for the wave function induces the presence of a Berry phase. The latter, added to the accumulated phase on the cyclotron orbit of the electrons under the effect of a magnetic field. Thus, a half-shift in the distribution of the Landau levels takes place, inducing quantum Hall effect conductivity (equation 1.20). The graphene is characterized with a double degeneracy of the valleys respectively in K and K 'of the Fermi surface, such that g = 4, which is added to that of the electron spin. This shift in conductivity energy was experimentally illustrated by the teams of Manchester and Columbia, which called it the Hall integer hall effect [17-19]. This presents one of the important results of graphene. The experimental study of this phenomenon reveals various electronic properties of graphene. Indeed, exfoliated graphene measurements under high magnetic field validate the existence of such an abnormal quantum Hall effect [20, 21].

$$E_n = \pm v_F \sqrt{2eB\hbar n} \qquad (1.19)$$

$$\sigma_H = \pm (n + \frac{1}{2}) \frac{ge^2}{h} \qquad (1.20)$$

II-3- Mechanical properties of graphene

Mono- and multilayer graphene have specific mechanical properties. However, to better understand these properties it is necessary to investigate the bulk material i. e. graphite. This latest represents infinity of graphene layers stoked along C axis. Mechanical properties of graphite were detailed by Kelly in 1981. It is characterized by strong C-C bond of dissociation energy equal to 348 kJ Mol^{-1}. Graphite structure leads to unique mechanical properties, where the elastic constant in the direction perpendicular to the plane differs from the elastic constants along the basal plane. This was verified using the preliminary experimental studies conducted in 1960 and 1970. Similar mechanical properties were also found in other carbon allotropes such as graphene. Graphene seems to be one of the strongest materials ever tested. Measurements illustrate its tensile strength which is more than 100 times greater than a steel film of the same thickness. On other hands, graphene elasticity modulus (stiffness) is about 1TPa (150 000 000 psi) [22].

II-4- Vibrational properties

Graphene band structure represents its dispersion curves along the high symmetry directions [Γ M K Γ] (Figure 6). These dispersions curves are theoretically and experimentally determined based on the inelastic scattering at different points in the first Brillouin zone and using infrared reflectivity. The vibration modes numbers is given by $N_t = 3Nr$. N corresponds to the number of cell in the crystal while r is assigned to the number of atoms per unit cell and 3r vibration branches. The primitive cell of the graphene is formed by two atoms A and B. Thus, the total number of branch is six where three are acoustic and the others are optical branches. These branches are separated into transversal and longitudinal depending on the orientation of the vibration that could be parallel (longitudinal) or perpendicular (transversal) to the direction of the atoms A and B. These vibration modes could be further divided according to the movement of the two sub-lattices.

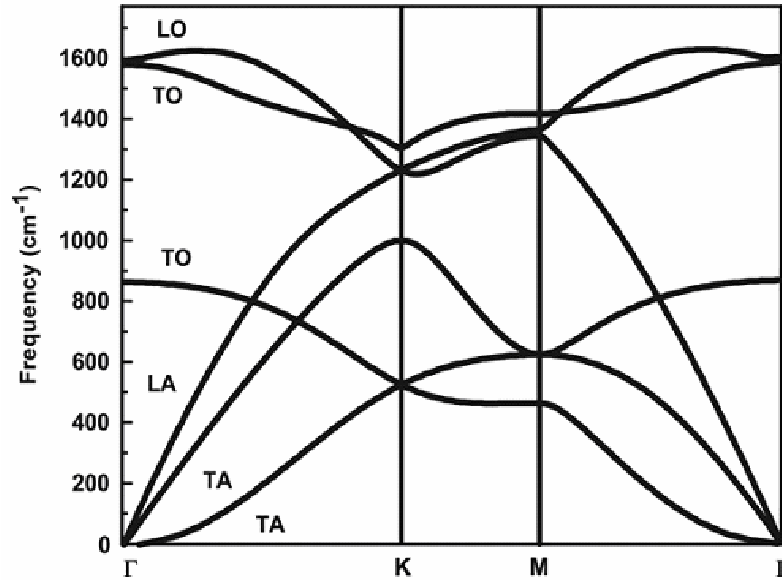

Figure 6: Graphene dispersion relation curves showing the "LO, TO, TO, LA, TA and TA"[23].

The dispersion relation of phonon depends on the number of layers of graphene. The number of phonons branch is multiplied by increasing the number of layers. Indeed, theoretical studies have shown a doubling of branches for bilayer comparing to single layer graphene.

II-5- Photoeffect

Graphene's high carrier mobility [24] and extensive optical absorption properties [23,25] covering the wavelength regime from terahertz to ultraviolet are an advantage for nano-electronics[26], nonlinear optics, plasmonics [27,28] and resonators applications [29]. Nevertheless, current optoelectronic graphene devices are orientated to considerate photocurrent mechanism [30]. Photocurrent enhanced due to hot carriers produced with an optical excitation to energy states far above the Fermi level. The excited hot carriers are significant due to their relaxation via acoustic phonons displaying a bottleneck effect, and through electron–electron scattering generating carrier multiplication which results in a strong decoupling between the electron and lattice temperature. Furthermore, photovoltaic response is also promising for upcoming applications.7 Photovoltaic effects may appear due to thermoelectric effect. These photo-responses change under different factors such as the presence of a substrate, the sample geometry, the electrode materials and biasing. This reveals the main role of the present substrate "SiC and SiO_2", particularly for the ultra fast domain, i.e. terahertz and ultraviolet. Indeed, a delay appears between the collective behaviour and the photoelectric effect in the sited optical domains. Recently, suspended exfoliated graphene has ameliorated the

photoresponse ten-fold. However, no photo-responses have been reported so far not in ultra fast domain. Indeed, the main graphene photo-responses study has been estimated in the vicinity of the M point of energy 4.7 eV ($\lambda \approx 260$ nm). To date this limitation has been counter-productive towards producing graphene photo-applications in the visible range. Nonetheless, light–matter interaction was widely investigated. Particularly, exfoliated, CVD graphene and practical applications require scalable approaches. Thus the majority of the interest was leaning to chemical vapor deposition (CVD) graphene for photo-detectors. Indeed, no previous examination addressed the use of epitaxial graphene. This is due to the mysterious photo-physics of epitaxial graphene. Mostly, the grain boundaries, random growth, impurities and the presence of the SiC substrate influence the mechanism of photo-responses and, photocurrent generation. This limits epitaxial graphene application for opto-photo-electronic applications. On other hands, magnetic properties of epitaxial graphene are important. In combination with photo-effects, outstanding properties may appear. To date, there has been a lack of experimental work in this area. In fact, impurity-related lifetime degradation is investigated based on the correlation between photoresistance and the magnetic field. Thus, the associated electron recombination process may identify the local structural defects. We have investigated, for the first time, photo response of epitaxial graphene. This will be reported in detail in chapter 5.

III- Epitaxial graphene

Since 1947, the preliminary theoretical studies of PR Wallace highlighted various properties of graphene. But, the discovery of the graphene growth method attracted more researchers to this material. The first prototypes were made by Geim team at Manchester University where they were able to isolate exfoliated graphene layer using micromechanical cleavage [31, 32]. Later in the same year, Walt Heer group in Atlanta succeed in developing epitaxial graphene, i. e thermally graphitization of silicon carbide SiC. In 2007, researchers began to use another method for the growth of CVD graphene. Thus, the three basic graphene approaches were defined. Following, we will limit our study to epitaxial graphene. We will detail is properties as well as that of SiC substrate.

III-1- Silicon carbide (SiC) substrate

Silicon carbide is a semiconductor composed of as equal number of silicon and carbon atoms. This semiconductor is rarely found in nature, it is only found in some meteorites or

rocks. Mainly, silicon carbide "SiC" found today is synthesized. In recent decades, this material has attracted the attention of the scientific community since it becames comparable to silicon. Its application extends to contain the field of microelectronics and optoelectronics. This material is characterized by different electronic properties such as: its broad band gap, high electronic mobility and chemical properties such as its inert, hardness, high stability[33] (table 1).

Polytype	Band gap eV	Lattice constants		
		a	c	c/na
2H	3.300	3.076	5.048	0.8205
4H	3.263			
6H	3.023	3.0806	15.1173	0.8179
3C	2.390	3.0827	7.5510	0.8165

Table 1: Variation of the band-gap and lattice parameters for the four most common polytypes of SiC. The ratio (c/na) shows the variation of (c/a) per layer in an n-layer polytype [33]

III-1-1- SiC structural properties

The atomic arrangement of the silicon carbide form sp^3 hybrid orbitals which is similar to that of GaAs. Its crystal structure is based on the covalent bond of Si - C (88% covalent and 12% ionic). Carbon and silicon are characterized with similar electronic structure ($Si = 3s^2\ 3P^2$, $C = 2s^2 2p^2$). There crystalline structure looks similar to dimant in the volume. The unit cell of the silicon carbide 'SiC' consists of a tetrahedron of carbon atoms in the center of which is placed Si (C respectively). This induces a first neighboring atoms of different chemical natures.

It exist over than 250 polytypes of SiC crystal structure. These polytypes differ by their stacking sequences along the C axis [0001] (Figure 7-a). The planes of C_1 distant, separating the base plane of the tetrahedron and the central atom of this structure in bilayer, are well bond and form an SiC biplane. The distance C_1 corresponds to the $\frac{1}{3}$ of the C_2 distance separating the central atom and the vertex of the regular tetrahedron (Figure7-a). These polytypes consist of elementary silicon and carbon bilayers stacked differently. The three most repeated SiC symmetries are: 3C (cubic) or (β-SiC), H (hexagonal) and R

(rhombohedral) or (α-SiC) [34]. The 3C-SiC is characterized by a stacking done by keeping the same orientation from one biplane to another. Whereas the stacking sequences of the hexagonal symmetry (H) are done by a rotation of 180 ° about the C axis [0001]. The atoms forming hexagonal symmetry occupy positions A, B or C in the hexagonal cell (Figure 7-b). The hexagonal polytype are usually denoted nH, atributed to Ramsdell notation. Here, n indicates the number of biplane in the unit cell along the [0001] axis followed by the initial Bravais lattice to which the hexagonal poly type belongs. Generally, epitaxial graphene is characterized with a bipolar behavior. Thus is assigned to the SiC biplane the termination where each termination C or Si specify the the polarity. This latter is denoted SiC (0001) for face terminated Silicon and SiC (000-1) for face terminated carbon. This bipolar aspect largely affects the properties of epitaxial graphene. Following, we will detail polarity effect by limiting our study to the hexagonal polytype. These characteristics remain the same for the different polytypes.

(a) **(b)**

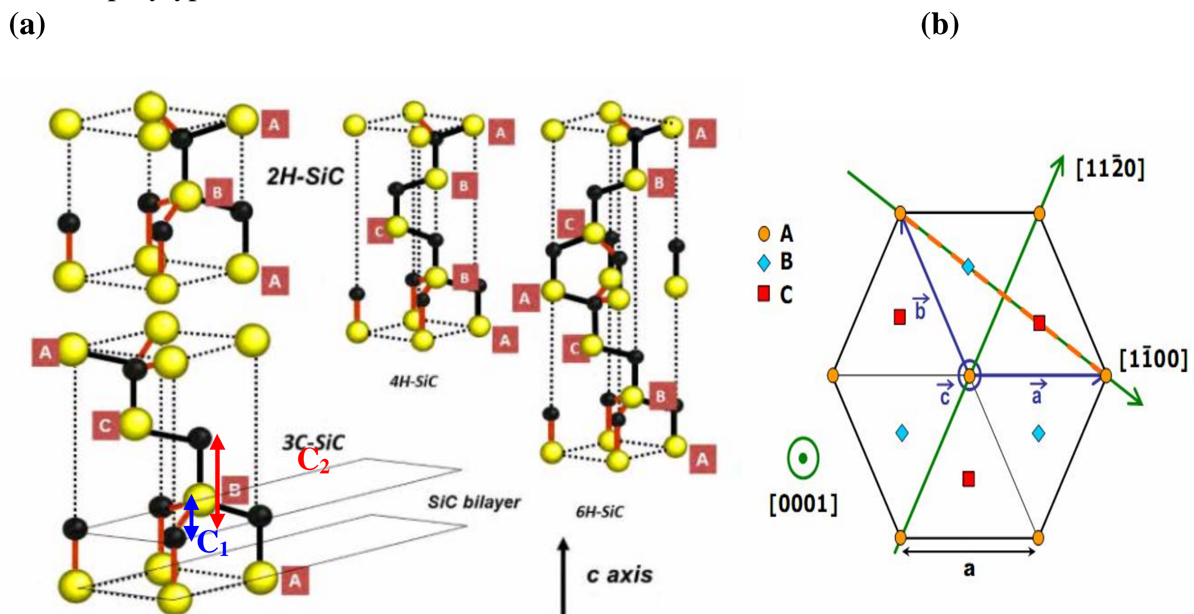

Figure 7: a- 3C-SiC, 4H-SiC, 6H-SiC poly type [35], **b-** hexagonal mesh representing the different symmetries of the SiC volume. Vectors are unit vectors of the mesh[Ref 16]. The locations A, B and C are the places where pile SiC tetrahedra center. The orange dotted line is the plan [in 1120].

III-1-2 Applications

SiC applications extend to reach numerous research areas such as: electronics, optoelectronics etc .... SiC was widely used in electronics following the discovery of

electroluminescence in a metal junction - SiC semiconductor by Round [36]. On other hands, it starts to be the basis of opto-electronic components of high frequency power, high temperature, or other materials do not work. Furthermore, the SiC substrate investigation extends to contain the production of epitaxial graphene.

III-2- Graphitization from SiC

Silicon carbide "SiC" shows high thermal relativity to high temperatures ($\geqslant$1000 ° C) [35, 37-38]. The graphitization on SiC starts from a well-determined temperature according to the polarity of the SiC. This induces different reconstruction evolution as a function of the temperature of Si-terminated SiC or terminated C [37, 39]. In fact, the graphitization would take place following the sublimation of the silicon atoms of the Si-C bilayers, although Si is more electronegative than carbon. Nevertheless, this effect comes from the sublimation temperature of Si which is lower ($\approx$1000°C), compared to that of carbon. Following the sublimation of three Si planes, the remaining "C" carbon atoms rearrange to form a graphitic C plane on the surface. Indeed, the choice of sublimed Si plane number from the SiC substrate bilayers is related to the atomic density of carbon atoms "C" present in a graphene plane. This atomic density is practically equivalent to three SiC biplanes.

However, different atomic reconstructions are observed at the beginning of graphitization in a well-defined temperature range [34-40]. From an experimental point of view, the graphitization takes place under ultra-vacuum "UHV" in a pressure range of below 10-9 mbar by heating the sample with electron bombardment or in an annealing furnace under a secondary vacuum (10- 5 mbar). Under UHV, the first graphene planes are observed at T = 1350 ° C for face terminated Si and T = 1100 ° C for face terminated C [41, 42]. Last years, epitaxial graphitization was developed using a flux of Si. This ensures the improvement of the quality and the graphene layer dimension.

III-2-1 Graphene on SiC face terminated Si

- **Structural properties**

Contrary to exfoliated graphene, other graphitization phase appears before the first graphene layer growth as a function of the annealing temperature. This phase is considered one of the fundamental steps during epitaxial graphitization process. It is observed at 1150 ° C for the finished face Si. This emerges clearly using Low Energy Electrons Diffraction “LEED” technique, as reported in Ref 49. Figure 8 shows a rich layer of C-atoms of a

diffraction pattern in 6√3x6√3R30 denoted 6R3-SiC. This phase is defined with respect to the unit cell (1x1) of the surface of the SiC (0001) [34, 38, 41]. It is characterized by a density of carbon atoms consistent with that of a graphene plane [39]. The cell of this graphitization phase is also called buffer layer, and the SiC (0001) are almost measurable for a common 6R3-SiC cell, which corresponds to 13x13 for graphene cell. This similarity is related to the lattice parameters of a graphene and the SiC (0001) surface. Despite the difference between SiC and graphene, wherein the lateral distance between the Si atom and the C atom on the (0001) plane is 0.166 nm, whereas the distance between two neighboring atoms in the graphene plane is about 0.142nm.

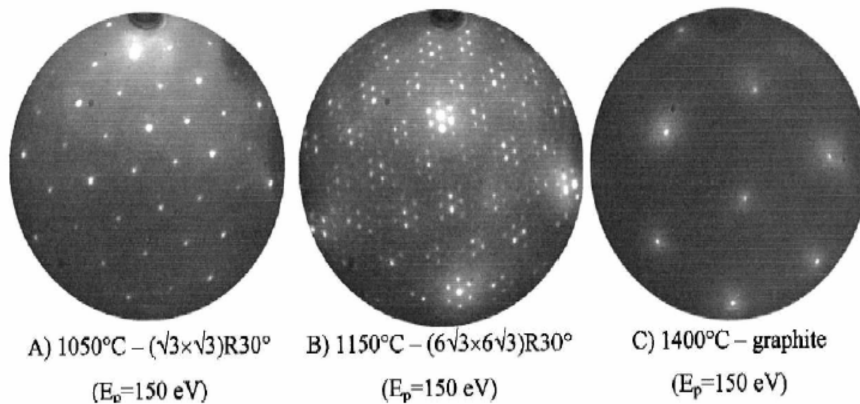

Figure 8: Image from Ref [37]. LEED images obtained on a sample 6HSiC (0001) for an energy of 150eV. We distinguish the following reconstruction area different annealing temperature: A) obtained √3x√3R30 ° to 1050 ° C, B) obtained 6√3x6√3R30 ° to 1150 ° C, C) 1X1 graphite obtained at 1400 ° C .

❖ 6R3-SiC phase properties

The cell parameters of this phase differs from one method to another which is a hampering for epitaxial graphene. STM measurments show surface reconstruction of 6 x 6-SiC [43, 44]. However, "LEED" shows a crystal symmetry of 6R3-SiC. This difference is assigned to the poor quality of the obtained STM images. Indeed, this variation could be attributed to the slightly electronic structure disturbed of the graphene layer from the substrate placed on a non-reconstructed surface of the SiC (0001) [34, 37]. This illustrates the presence of the 6 x 6-reconstruction SiC. Indeed, 6R3-SiC phase is not due to surface reconstruction. But it comes from purely electronic effect type charge transfer between graphene and the substrate. LEED is a complex phenomenon associated with multiple scattering effect between this first

graphene plan and the SiC surface [37]. This explains the symmetry in 6 x 6-SiC observed in STM compatible with LEED experiments [44]. However, from another point of view the difference in the size of the formed phase size using these both techniques could be ascribed to the self-organization of atoms "C" during annealing [41]. This nano structuring leads to surface reconstruction between the latter plane and the SiC first graphene plane simultaneously, where there are few carbon atoms "C" bound to silicon atoms "Si" of the substrate in or linked to other atoms carbon "C" neighbors.

❖ Epitaxial growth of carbon layers

For a temperature above 1350 ° C [39], the graphene layer is formed (Figure 8). The crystal lattice of the formed C planes are rotated with 30 ° in respect to the SiC (0001) under AB type stacking similar to graphite. Generally, epitaxial growth is defined as an oriented of two crystals with respect to each other which have a number of similar symmetry in their crystal lattices. Controlled variation of UHV annealing temperature allows graphene layer to grow one-to-one with respect to the substrate [42, 45]. This method allows the controlled synthesis of epitaxial graphene layers, where graphene planes follow the steps of the substrate. Indeed, the dimension is enlarged by this technique with respect to exfoliated graphene where the localized graphene sizes reach 100 nm [42, 46].

❖ Electronic structure

Rollings et al. revealed a band structure consistent with that predicted by the preliminary theoretical studies for graphene layers [47]. Indeed, carbon plan doped electrons is observed. Here, Dirac point is observed at 0. 27 eV below the Fermi level to a few layers of graphene. However, Bostwick et al. and Zhou et al. the band structure of graphene monolayer confirms the electronic structure "cone Dirac" [48] (Figure 9- a, b). A good agreement between the experimental results and the band structure of graphene is determined theoretically verified. Despite the presence of the substrate underneath graphene electronic structure "Dirac cone" is still preserved.

This shows that the doping of the graphene is independent of the substrate [47]. While the electronic structure of low energy graphene varies from theoretical results for an ideal graphene. This difference can be attributed to a normalization (without gap opening) of the "Dirac cone" structure originating from the electron-electron, electron-plasmons interaction. This change extends to contain the concentration of electrons in layers forming a biplane of

graphene. Indeed, ARPES measurements performed by Ohta et al show a signature doping electrons ($E_F = E_D + 0.4eV$) with a doping difference between the plan, plans more doped than the other [49] (Figure 9-c). In fact, the electronic structure of a biplane AB stacking different from the monoplane (Figure 7). This non-equivalence of the two planes of graphene affects the electronic structure. In particular, a gap between the bands is displayed. This reveals the decay of the excess electron density map all away from the graphene - substrate interface.

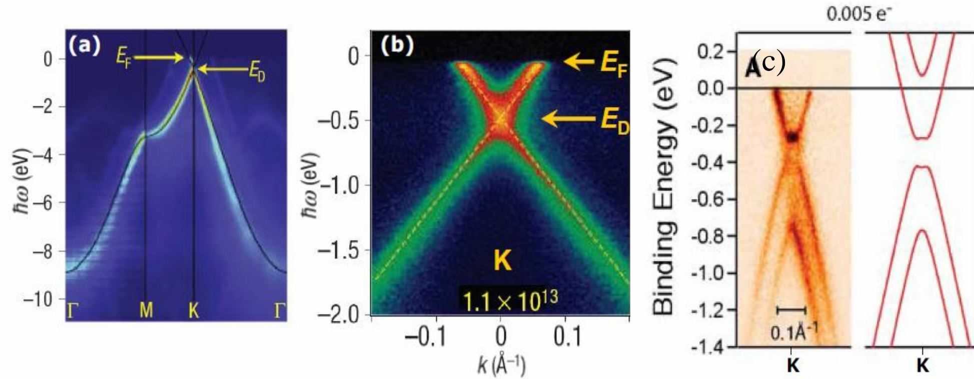

Figure 9: ARPES of graphene on 6H-SiC (0001) show the electronic structure of a graphene monolayer. Images from [45]: a- experimental band structure Γ-Γ MK. The band of graphene is very visible. EF is the Fermi energy and ED is the energy of the Dirac point. The black curve is the band structure of isolated graphene calculated by the method of strong bonds. b- Zoom at K point that reveals the structure "Dirac cone." Doping electron is 1.1 x 10^{13} cm^{-2}.c- Comparison between the band structure of the 6R3-SiC phase with that of graphene.

❖ Transport properties

The first magneto-transport measurements were carried out in 2004 by the team of Walt de Heer in Atlanta for a system consisting of a few C plans (3 to 5 shots graphene) on the surface of SiC (0001) [50]. Their work revealed a pattern of behavior "two-dimensional electron gas", of 1100cm^2 / V.s electron mobility. s corresponding to a charge carrier density of 10^{12} cm^2. Unlike exfoliated graphene, the absence of SiO_2 below the C planes prevents the use of a back gate to modulate the carrier density of the system. To solve this problem, one method was covering a part of the graphene planes with a thickness of 100 nm alumina (Al_2O_3). This layer provides a useful gate insulating means to type devices field effect transistor (source, drain and gate) [50]. We also note that the magneto-transport measurements have not demonstrated a quantum Hall effect for this system. On the other hand, through studies of Shubnikov de Haas oscillations, the existence of a Landau level the charge

neutrality point was checked. This shows the chirality of quasiparticles of a graphene monolayer.

III-2-2- Graphene on SiC face terminated C: SiC $(000\bar{1})$

❖ Structural properties

Unlike face terminated Si, we find less studies characterizing the early stages of graphitization SiC face finished carbon C, denoted SiC (000-1). Its graphitization temperature is lower compared to the face terminated silicon, it is about 1100 °C. No signs of reconstruction in 6R3-SiC is visible on the diffraction cliches for surface observed by LEED UHV [34, 37, 38] (Figure 10). Indeed, two types of surface reconstructions 2x2 and 3x3-SiC-SiC coexist before and after the early stages of graphitization. The prevalence of each of these reconstructions strongly dependent on the growth method [51]. The graphene growth is done with a rotational disorder between grains. This was proved by the diffraction patterns [37] (Figure 10). Here, the disorientation of the layers, as well as the size of the zones of the same crystalline quality depend very much on the preparation.

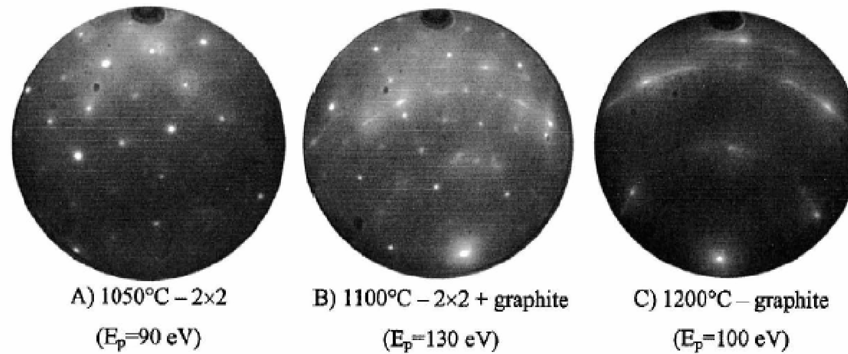

Figure 10: Image of Ref [37]. LEED images of graphene on 6HSiC (000-1) to an energy Ep There are reconstructions of the area following different annealing temperature: a- 2 X 2 obtained at 1050 ° C, b- 2 X 2 and 1 X 1 of graphite obtained at 1100 ° C, c- 1X1 graphite obtained at 1200 ° C.

❖ Electronic properties

The ARPES experiments on graphene finished carbon face "SiC" is difficult due to rotational disorder of plans C. Thus, little information are provided about the electronic structure of n layer of graphene grown on SiC (000-1). By the way, the ARPES study could determine Π and Π * bands of graphene on SiC (000-1) graphitized 3x3-SiC [52]. While the

energy distribution of the Landau levels and the existence of a linear band structure of type "Dirac cone" for plans C neutral on the surface [53] was demonstrated by infrared transmission in a magnetic field. This shows a decoupled electronic structure for the monolayer graphene.

❖ Transport properties of the system

The appearance of a two-dimensional electron gas type of behavior is one of the peculiarities of graphene. This behavior is associated with Shubnikov Haas oscillations. The characteristics of the "two-dimensional electron gas" are best compared to that of the Si face and those of exfoliated graphene, wherein the electron mobility of the system $\mu = 27000 cm^2$ =V/s and the carrier density of $n = 1.\ 10^{12}\ cm^{-2}$. In fact, the difference depending on the polarity can be attributed to the production method, where the use of an annealing furnace can offer better structural properties.

On other hands, the transport properties differ as function of the graphene - substrate interaction. A charge transfer occurs between the substrate and the carbon planes, where the closest planes of the interface are the doped and largely contribute to the transport. The Fermi energy is estimated at 0. 21 eV above the Dirac point to the nearest plan [54] substrate. However, the electronic structure of the substrate for low impact, should be similar to that of a multi graphene plane AB stack or to that of graphite. Unlike face If we note the disappearance of quantum Hall effect. However, the system transport properties are dominated by the C virtually decoupled from the substrate plane. We conclude that graphene on SiC face terminated C is characterized by better transport properties than that of the face terminated Si this makes it more cost effective for applications in electronic nano.

IV- Applications

Since the Nobel Prize in Physics honoured to Geim and Novoselov for graphene a large publication number appear. This reveals the broad scientific committee interest of this material graphene [55]. Graphene is characterized by a non-zero electrical conductivity. This latest remains above the quantum conductivity $\sigma \sim e^2 / h$ [56] even for a zero density K and K '. For intrinsic graphene, the Fermi level is situated at the intersection of the cones Dirac the equivalent points K and K '. Under the effect of an electric field, the Fermi level can be moved. Thus, the graphene can be n-type conductive (with electrons) or p (with holes) all depending on the polarization of the field [57]. Contrary to other two-dimensional semiconductors, graphene quantum Hall effect may exists even at room temperature [58].

Furthermore, graphene is transparent, it is characterized by a 95% transparency to visible light for a film of 2 ML (mono layer). Thus, it absorbs only 2.3% of white light [59]. Such a transparency make of graphene a powerful candidate for ITO "indium tin oxide" for applications in transparent electrode of a surface resistance of less than 1 kΩ/sq [60-61]. Its unique mechanical properties open door to graphene applications as: flexible conductor [62] and membrane for gas detection [63]. Furhtermore, Graphene's high carrier mobility, associated with its Dirac electron spectrum1 and extensive optical absorption properties [22, 24] in ultra fast domain allows the conception of original applications in nano-electronics, [25] nonlinear optics, plasmonics [27, 28] and resonators [29].

V- conclusion

We presented the properties of graphene in its different states, these benefits and limitations, and some new potential applications. The objective of this work is to show the variation of these properties for the epitaxial graphene by modifying the shape of the surface of the layer of epitaxial as well as the presence of other factors.

References :

[1] Erwin Schrödinger, Mémoires sur la mécanique ondulatoire, Gabay (Sceaux): 1988.

[2] E. Francis, ''Valence Electrons.''

[3] C. Berger, Z. Song, X. Li, A.Y. Ogbazghi, R. Feng, Z. Dai, A.N Marchenkov, E.H. Conrad, P.N. First, W.A. de Heer, J. Phys. Chem B, 108, 19912, 2004.

[4] R.E. Peierls, Helv. Phys. Acta, 7, 81-83, 1934.

[5] L.D. Landau, Phys. Z. Sowjetunion, 11, 26-35, 1937.

[6] François Varchon, Propriétés électroniques et structurales du graphene sur carbure de silicium, universite Joseph Fourier (2008).

[7] N. D. Mermin, Phys. Rev. 176(1), 250, 1968.

[8] N.W. Ashcroft et N.D. Mermin, Physique des solides. EDP Sciences, 2002.

[9] S. Reich, J. Maultzsch, C. Thomsen et P. Ordejon, Phys. Rev. B 66, 035412, 2002.

[10] P.R. Wallace, Phys. Rev., 71, 622, 1947.

[11] G. Gu, S. Nie, RM. Feenstra, R.P. Devatry, W.J Choyke, W.K. Chan et M.G. Kane, "Applied Physics Letters, vol. 90, no.25, p. 253507-3, 2007.

[12] I. Meric, N. Baklitskaya, P. kim et K. Shepard, IEDM 2008. IEEE International, p. 1-4, 2008.

[13] I. Meric, M.Y. Han, A.F. Young, B. Ozyilmaz, P. Kim et K.L. Shepard, Nat Nano, vol. 3, no.11, p. 654-659, 2008.

[14] J.S. Moon, D. Curtis, M.Hu, D. Wong, C. McGuire, P.M. Campbell, G. Jerigan, J.L. Tedesco, B. VanMil, R. Myers-Ward, C. Eddy, et D.K. gaskill, Electron Device Letters, IEEE, vol. 100, no.6, p. 650-652, 2009.

[15] X. Wang, Y. Ouyang, X. Li, H. Wang, J. Guo et H. Dai, Physiscal Review Letters, vol. 100, no.20, p. 206803-4, 2008.

[16] C. Bena et G. Montambaux, arXiv: 0712.0765v1, cond-mat.mes-hall, 2007.

[17] Novoselov, K. S.; Geim, A. K.; Morozov, S. V.; Jiang, D.; Katsnelson, M. I.; Grigorieva, I. V.; Dubonos, S. V. Firsov, A. A., Nature 438, 7065, 197-200, 2005.

[18] Zhang Y.; Tan Y.-W.; Stormer H. L. Kim P., Nature 438, 201-204, 2005.

[19] A.K. Geim, K.S. Novoselov, Nature Mat. 6, 183, 2007.

[20] J. N. Fuchs, M. O. Goerbig, pour la Science 367, 36, 2008.

[21] H.W.Kroto, J.R. Heath, S.C. O'Brien, R.F. Curl, et R.E. Samelley, Nature, vol. 318, no. 6042, p. 162-163, 1985.

[22] Joseph Scott Bunch, mechanical and electrical properties of graphene sheets, Cornell University, 2008.

[23] A. K. Geim and K. S. Novoselov, Nat. Mater., 6, 183, 2007.

[24] F. V. Kusmartsev and A. M. Tsvelik, JETP Lett., 42, 257, 1985.

[25] W. Li, B. Chen, C. Meng, W. Fang, Y. Xiao, X. Y. Li, Z. F. Hu, Y. X. Xu, L. Tong, H. Q. Wang, W. T. Liu, J. M. Bao and Y. R. Shen, Nano Lett., 14, 955, 2014.

[26] Y. P. Wu, B. Wang, Y. F. Ma, Y. Huang, N. Li, F. Zhang and Y. S. Chen, Nano Res., 3, 661, 2010.

[27] W. S. Kim, Y. I. Kim, H. J. Kim, J. Y. Hwang, S. Y. Moon, N. H. Park, K. B. Shim, H. W. Kim, H. Ham and H. Huh, J. Mater. Chem., 21, 15655, 2011.

[28] H. W. Tien, Y. L. Huang, S. Y. Yang, J. Y. Wang and C. C. M. Ma, Carbon, 49, 1550, 2011.

[29] Q. Liu, Z. F. Liu, X. Y. Zhang, N. Zhang, L. Y. Yang, S. G. Yin and Y. S. Chen, Appl. Phys. Lett., 92, 223303, 2008.

[30] L. Sun, C. G. Tian, M. T. Li, X. Y. Meng, L. Wang, R. H. Wang, J. Yin and H. G. Fu, J. Mater. Chem. A, 1, 6462, 2013.

[31] Berger, C.; Song, Z.; Li, T.; Li, X.; Ogbazghi, A. Y.; Feng, R.; Dai, Z.; Marchenkov, A. N.; Conrad, E. H.; First, P. N. de Heer, W. A., The Journal of Physical Chemistry B 108(52), 19912-19916, 2004.

[32] Novoselov, K. S.; Geim, A. K.; Morozov, S. V.; Jiang, D.; Katsnelson, M. I.; Grigorieva, I. V.; Dubonos, S. V. Firsov, A. A., , Nature 438 (7065), 197-200, 2005.

[33] C. J. Schneer, Acta Crystallog., **8** (1995) 279-285

[34] A.J. Van Bommel, J.E. Crombeen, A. Van Tooren, Surf. Sci., 48, 463, 1975.

[35] Properties of silicon carbide, Edited by GARY L HARRIS Materials Science Research Center of Excellence Howard university, Washington DC, USA.

[36] Round H.J., Electrical World 19, 309, 1907.

[37] I. Forbeaux, J.-M. Themlin, A. Charrier, F. Thibaudau, J.-M. Debever, Appl. Surf. Sci., 162-163, 406, 2000.

[38] F. Owman, P. Martensson, Surf. Sci., 369, 126, 1996.

[39] I. Forbeaux, J.-M. Themlin, J.M. Debever, Phys. Rev. B, 58, 16396, 1998.

[40] K. Heinz, J. Bernhardt, J. Schardt, U. Starke, J. Phys. : Condens. Matter, 16, S1705, 2004.

[41] W. Chen, H. Xu, L. Liu, X. Gao, D. Qi, G. Peng, S.C. Tan, Y. Feng, K.P. Loh, A.T.S. Wee, Surf. Sci., 596, 176, 2005.

[42] A. Charrier, A. Coati, T. Argunova, F. Thibaudau, Y. Garreau, R. Pinchaux, I. Forbeaux, J.-M. Debever, M. Sauvage-Simkin, J.-M. Themlin, J. Appl. Phys., 92, 2479, 2002.

[43] L.Li, I.S.T. Tsong, Surf. Sci., 351, 141, 1996.

[44] C.S. Chang, I.S.T. Tsong, Y.C. Wang, R.F Davis, Surf. Sci., 256, 354, 1991.

[45] T. Ohta, A. Bostwick, J.L. McChesney, T. Seyller, K. Horn, E. Rotenberg, Phys. Rev. Lett, 98, 206802, 2007.

[46] J. Hass, R. Feng, T. Li, X. Li, Z. Zong, W.A. de Heer, P.N. First, E.H. Conrad, C.A. Jerey, C. Berger, Appl. Phys. Lett, 89, 143106, 2006.

[47] E. Rollings, G.-H. Gweon, S.Y. Zhou, B.S. Mun, J.L. McChesney, B.S. Hussain, A.V. Fedorov, P.N First, W.A. de Heer, A. Lanzara, J. Phys. Chem. Solids, 67, 2172, 2006.

[48] S. Y. Zhou, G.-H. Gweon, A. V. Federov, P. N. First, W. A. de Heer, D.-H. Lee, F. Guinea, A. H. Castro Neto, A. Lanzara, Nat. Mater., 6, 771, 2007.

[49] T. Ohta, A. Bostwick, T. Seyller, K. Horn, E. Rotenberg, Science, 313, 951, 2006.

[50] C. Berger, Z. Song, X. Li, A.Y. Ogbazghi, R. Feng, Z. Dai, A.N Marchenkov, E.H. Conrad, P.N. First, W.A. de Heer, J. Phys. Chem B, 108, 19912, 2004.

[51] J. Bernhardt, M. Nerding, U. Starke, K. Heinz, Mat. Sci. Eng. B, 61, 207, 1999.

[52] K. V. Emstev, F. Speck, T. Seyller, L. Ley, Phys. Rev. B, 77, 155303, 2008.

[53] M.L. Sadowski, G. Martinez, M. Potemski, C. Berger, W.A. de Heer, Phys.Rev. Lett, 97, 266405, 2006.

[54] C. Berger, Z. Song, X. Li, X. Wu, N. Brown, C. Naud, D, Mayou, T. Li, J. Hass, A.N Marchenkov, E.H. Conrad, P.N. First, W.A. de Heer, Science, 312, 1191, 2006.

[55] Richard Van Noorden, ‘Chemistry: the trials of new carbon', Nature 469, 14-16, 2011.

[56] Novoselov, K. S.; Geim, A. K.; Morozov, S. V.; Jiang, D.; Katsnelson, M. I.; Grigorieva, I. V.; Dubonos, S. V. Firsov, A. A., Nature 438 (7065), 197-200, 2005.

[57] Novoselov, K. S.; Geim, A. K.; Morozov, S. V.; Jiang, D.; Zhang, Y.; Dubonos, S. V.; Grigorieva, I. V. Firsov, A. A., Science 306(5696), 666-669, (2004).

[58] Novoselov, K. S.; Jiang, Z.; Zhang, Y.; Morozov, S. V.; Stormer, H. L.; Zeitler, U.; Maan, J. C.; Boebinger, G. S.; Kim, P. Geim, A. K., Science 315, 5817, 1379, 2007.

[59] Nair, R. R.; Blake, P.; Grigorenko, A. N.; Novoselov, K. S.; Booth, T. J.; Stauber, T.; Peres, N. M. R. Geim, A. K., Science 320(5881), 1308, 2008.

[60] Blake, P.; Brimicombe, P. D.; Nair, R. R.; Booth, T. J.; Jiang, D.; Schedin, F.; Ponomarenko, L. A.; Morozov, S. V.; Gleeson, H. F.; Hill, E. W.; Geim, A. K. Novoselov, K. S., Nano Letters 8(6), 1704-1708, 2008.

[61] Wang, X.; Zhi, L. Mullen, K., Nano Letters 8(1), 323-327, 2008.

[62] Lee, C.; Wei, X.; Kysar, J. W. Hone, J. Science 321(5887), 385-388, 2008.
[63] Chen, J.-H.; Ishigami, M.; Jang, C.; Hines, D.; Fuhrer, M. Williams, E., Advanced Materials 19(21), 3623-3627, 2007.

Chapter II

Characterization technique

I- Introduction

As part of our study we focused on the localization of epitaxial graphene, the determination of its nature suspended or strongly bounded to the substrate SiC and the study of its electrical properties. The optical localization of epitaxial graphene is based on particular morphological changes on the surface such as: roughness, homogeneity, defects, contrast, substrate steps and new shapes of the graphene layer. In this chapter, we will present the characterization techniques used during our work. These characterization techniques are mainly: optical microscopy, Raman spectroscopy, atomic force microscopy (AFM), ultrasonic force microscopy (UFM) and photoelectric set up. Through some theoretical reminders, we will highlight their potentialities and their limits with respect to the size of the graphene layer, i.e. of atomic order (that of carbon atom (≈ A °)). These characterization techniques determine: the number of graphene layers, the defects, the dimensions of the elaborated graphene flakes, the shapes of the graphene layer, the electric properties and their photoelectric properties.

II- Graphene surface analysis

The change of the surface morphology of epitaxial graphene and its interaction at the interface with the substrate characterizes the properties of graphene. This effect is very important especially for such type of graphene. Epitaxial graphene is thermal produced from SiC substrate, which affects its optical, electrical and mechanical properties. Indeed, surface studies remain very important for epitaxial graphene. Where, its visual location remains among the fundamental problems faced since its growth in 2004. Thus, it is important to analyze the graphene surface in order to study it. Several complementary characterization techniques are used to characterize materials on a microscopic and nanometric scale.

1- Optical microscopy

Optical microscopy is one of the fundamental characterization techniques used to obtain the surface image of the graphene layer. Most microscopes are equipped with graduated axis to measure the size of the observed object. Here, we recall the principle of this microscopy. Figure 1 shows the general schema of optical microscope. Each microscope can contain two lamps. The first is used for transmission microscopy, while the second is used for reflection microscopy. The choice of the used microscopes depends on the nature of the studied sample. The transmission mode is suitable for the analysis of transparent samples at the used

wavelengths. This mode is generally used in biology. However, the reflection mode is designed to study metallic or semi-conductor materials opaque to visible light. As part of our work we used Bright Field (Bright Field). Where, the surface defects or localized roughness appear as dark areas. This explains the visualization of defects as areas of different dark shapes on a light background.

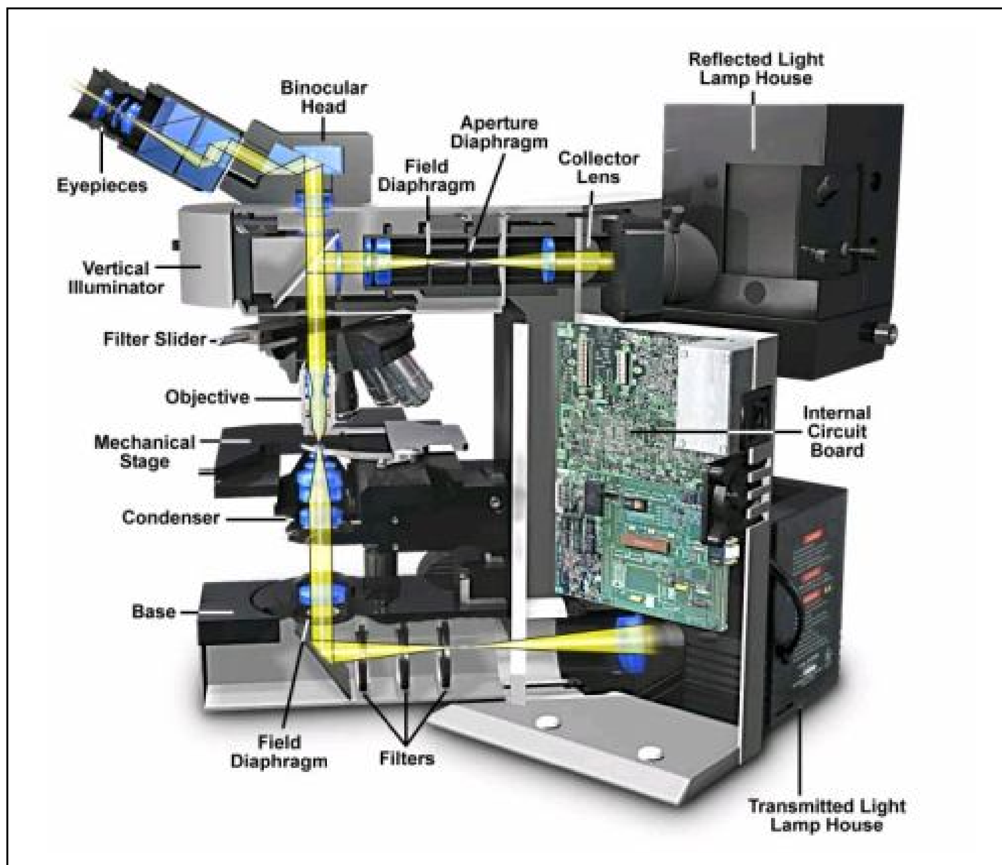

Figure 1: Optical microscopy [1].

2- Atomic Force Microscopy (AFM)

The limit of some spectroscopy to the analysis of substrates morphology of different natures "metal, insulator and semiconductor" [2] required the use of other techniques ensuring better surface analysis [3]. These techniques include atomic force microscopy (AFM).

2- 1 Principle of the AFM

In 1986, G. Binnig, C.F. Quate and C. Gerber invented the AFM atomic force microscope [4]. Its nanoscale axial resolution lies between atomic and optical microscopy resolution of micrometric scale. Its field of application extends to contain biological objects of

large size (micrometric). This microscopy is based on two modes: contact mode and tapping contact mode.

AFM microscopy is based on the measurement of the interaction force between the atom of the tip and the atoms of the surface [5-8]. For this microscopy, the tip is integral to the cantilever as the sample moves underneath (Figure 2). At the meeting of the atoms of the tip with that of the surface, the atoms attract themselves in space by the interaction of Van der Waals [9, 10]. Thus, the force of attraction is minimal.

The tip force - substrate is given by Hooke's law. But, experimentally, it is translated by the deflection of the lever arm. Hooke's law is given by the following formula:

$$F = - kx,$$

where k is the stiffness constant of the spring and x is the deflection of the lever.

The deflection of the cantilever can be measured by optical interferometer or by the deflection of the laser beam reflected by a mirror (Figure 2). The reflected beam falls on two opposing photodiodes. A slight deflection of the beam will give an easily measurable differential signal. This allows the amplitude of the deflection to be recorded as a function of the position X and Y. Thus, an image of the interaction forces between the tip and the surface atoms is obtained.

The AFM microscope used during our study is: Nanoscope IIIa, Bruker AXS in the physics laboratory at Lancaster University UK (UK). We used a standard mode of contact, characterized by a resolution k = 0.2 N / m. The sample is placed clearly on a support before analyzing it. This ensures a clear localization of the study area. A detailed description of this characterization technique will be given in the following chapters.

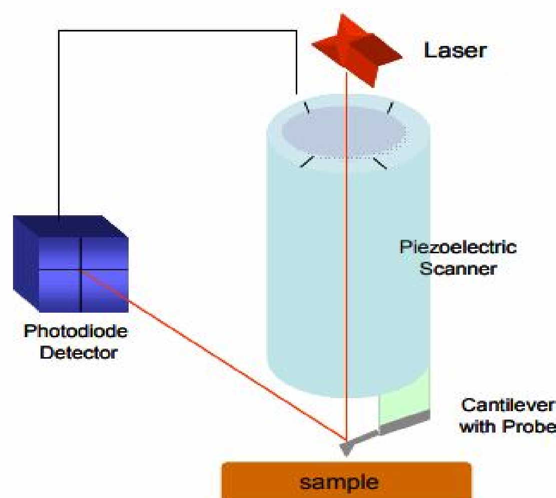

Figure 2: AFM atomic force microscopy [11].

3- Ultrasonic force microscopy (UFM)

Ultrasonic force microscopy UFM is based on atomic force microscopy. The tip of the cantilever vibrates in contact with the sample surface at very high frequency of the order of a few megahertz (4 MHz). The force between the tip and the sample depends non-linearly on the position of the tip. AFM atomic force microscopy is widely used to understand the surface morphology of graphene as well as other nanoscale materials properties. It gives an image of the topography of the surface at constant force. The highest reach frequency for these approaches is limited by the resonant frequency of the peak which is of the order of 10 to 100 KHz. Its frequencies do not reach the regions of interest Intermolecular vibrations as well as the relaxation frequencies which are of the order of MHz or GHz. This makes this microscopy unable to analyze the local mechanical properties of rigid structures on the surface of materials. Thus, a different approach for the detection of these high frequency vibrations is required. This approach is based on nonlinear detection. This was realized for a console of very high rigidity, leaving the compromise between the maximum force resolution and the sensitivity to dynamic viscoelastic properties called the ultrasonic force microscopy UFM. The name originates from the vibration frequency ν_v in the Ultrasound domain [12 - 16]. Indeed, it has been proven that the UFM is competent of mapping the mechanical responses for materials of very high rigidity by incorporating various heterogeneous materials ranging from rigid polymers to ceramics [4, 5]. This new characterization technique provides new information on the local elastic properties, the forms found on the surface. The UFM makes it possible to image the elastic properties of the materials by a spatial resolution less than micron limited by the wavelength of the ultrasound. This study was used within the framework of our thesis to prove the existence of a mechanical response of the shapes obtained following the modification of the graphene layer which will be given in detail in the following chapters.

3-1- Principle of the UFM

Imaging the top surface and nano-mechanical mapping are determined using UFM. UFM measurements are obtained during our work via a modification of a commercial AFM system (Nanoscope IIIa, Bruker AXS). This is using an additional piezoelectric ceramic disc (Piezomaterials PI) which oscillates vertically [6].

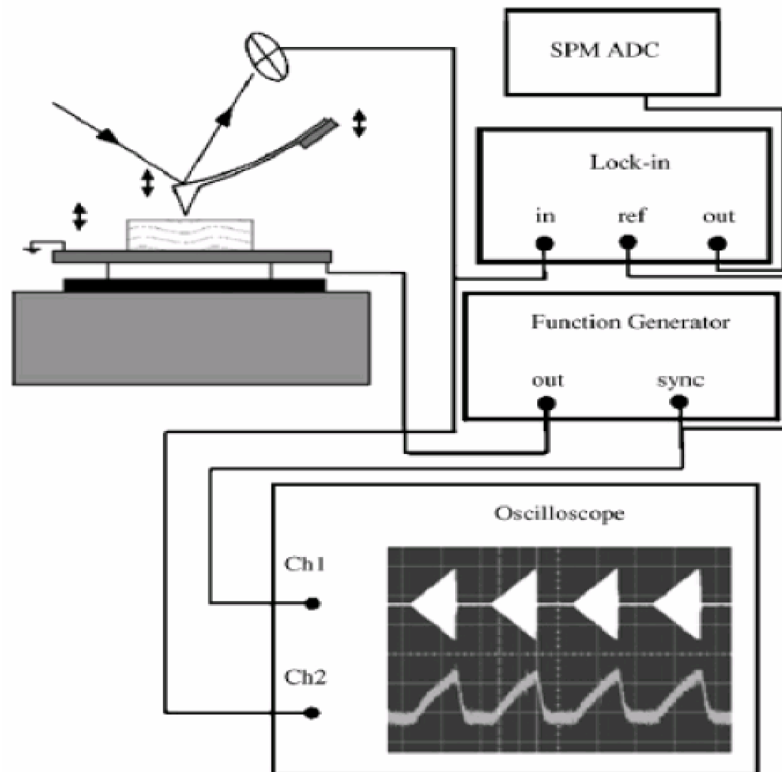

Figure 3: Principle of ultrasonic force microscopy [7, 8].

4- Raman Spectroscopy

During the interaction of monochromatic light with a medium (solid, liquid, gas), this radiation can be transmitted, absorbed, reflected, or diffused. For diffusion, two types of diffusions can be distinguished: the first type is the elastic diffusion. Here, the scattered photons retain the same frequency as that of incident photons. The second type of diffusion is inelastic scattering, where a small part of incident light (1 photon on photons) of frequency is scattered with frequencies lower than that of incident photons. This exchange of energy between the diffused light and the incident light is known by the Raman effect.

4-1- Principal

Raman effect is demonstrated in 1928 by the Indian physicist Chandrasekhara Venkata Raman, winner of the Nobel Prize in 1930 [17-21]. This spectroscopy is a non-destructive characterization technique. It is based on the excitation of a material by a monochromatic source or the levels of energies are brought to the virtual levels to then retransmit diffused radiations comprising two types of signals. The elastic scattering or Rayleigh scattering presents the major part of the diffusion phenomenon. The light is thus diffused at a frequency equal to that of the light. For the smallest fraction of the incident beam the diffusion is called

inelastic. In this case, for radiations shifted to the low frequencies "i. e. Red shift". Here, absorption of energy appears which is assigned to Stokes radiations. For the other case, the radiations are shifted to the high frequencies "Blue shift". The photons yield energy and originate Anti-Stokes radiation [17, 18].

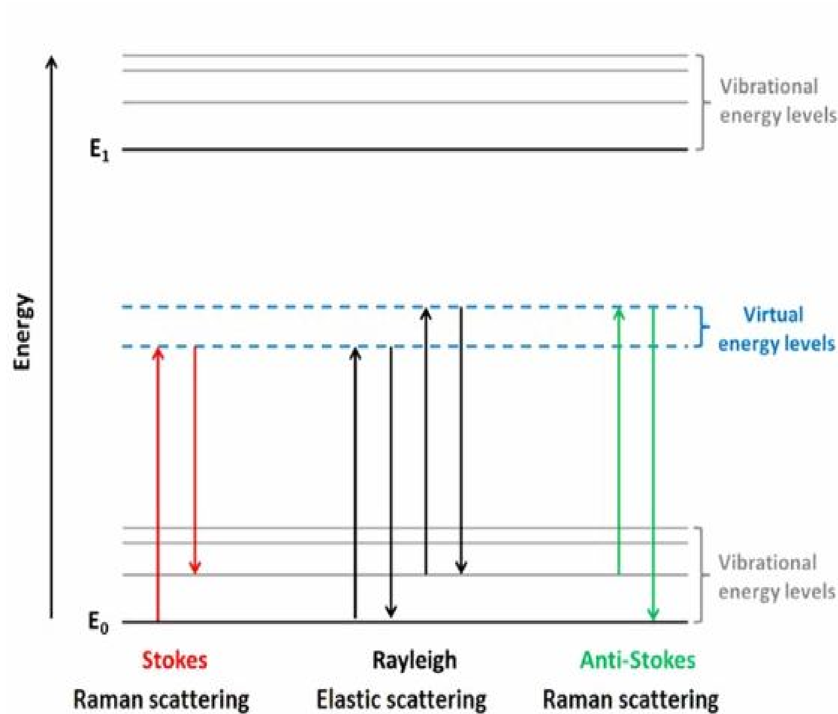

Figure 4: Raman and Rayleigh scattering [22].

The displacement of the Raman line varies between 100 and 1000 cm^{-1} while that of the Rayleigh line width is about 1000 cm^{-1}. This shows that the Rayleigh line is very large compared to the Raman displacement. Thus, the elimination of the Rayleigh line is required during the observation of the Raman effect (Figure 4). In addition, the comparison of the intensity ratio of the Stokes and Anti-Stokes lines shows that:

$$\frac{I_{Anti-Stokes}}{I_{Stokes}} = e^{-\beta h \nu} \leq 1$$

This illustrates the power of visualization of the Stokes part of the Raman spectrum.

- **Classical description of the Raman phenomenon**

The classical description of the wave diffusion is related to the change in the polarization. Following the excitation of a crystal by a monochromatic wave, a displacement of the electron cloud takes place with respect to the nucleus causing the creation of a dipole moment. For weak electric fields the expression of the polarization is given by

$$P = \varepsilon_0 \tilde{\chi} \vec{E}$$

The susceptibility represents the deformation capacity of the electron cloud, as well as the vibration of the atomic network. The relative displacement U of the first-order atoms is given by

$$\tilde{\chi} = \tilde{\chi}_0 + \left(\frac{\partial \chi}{\partial \vec{U}}\right)_0 \vec{U} \quad , \quad \text{where} \qquad \vec{U} = U_0 \cos(\vec{q}.\vec{r} - \Omega t)$$

The electric field is written in the following form $\vec{E} = \vec{E}\cos(\vec{k}_i.\vec{r} - \omega_i t)$. Thus, the polarization is given by

$$\vec{P} = \varepsilon_0 \tilde{\chi}_0 \vec{E}_0 \cos(k.r - \omega_i t) + \frac{\varepsilon_0 \vec{E}_0}{2}\left(\frac{\partial \tilde{\chi}}{\partial \vec{U}}\right)_0 \vec{U}_0 \{\cos((k_i + q)r - (\omega_i + r)t) + \cos((k_i - q)r - (\omega_i - r)t)\}$$

Where, the first term is associated with frequency Rayleigh scattering ω_i. The second and third term correspond to the emission of the radiation of frequency equal to $(\omega i - \Omega)$ called diffusion Stokes and of frequency $(\omega i + \Omega)$ called Anti-Stokes diffusion (Figure5). Thus, the classical approach highlights the conservation laws that govern first-order Raman scattering in a crystal.

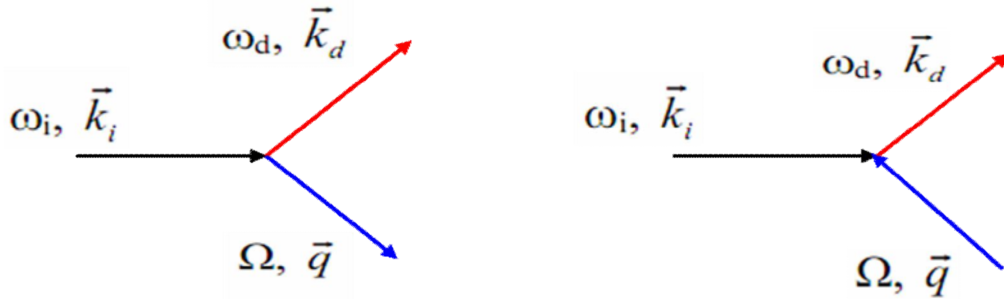

Figure 5: Schematic representation of the incident radiation emitted during Stokes and Anti-Stokes scattering.

❖ **The quantum mechanical description of the Raman**

The classical approach does not take into account the major role of electrons. In fact, the photon - phonon interaction is unlikely due to the large difference between the frequency of incident photons and phonons (Figure 6). In fact, the frequency of incident photons is much higher than that of phonons [19, 20]. This is where the intermediate role of electrons intervenes to ensure this interaction. In this approach, the Raman process can be described in three steps:

- The Interaction of an incident photon with an electron and the creation of an electron-hole pair.
- The diffusion of an electron by the phonon involved.
- The Recombination of an electron by emitting a photon.

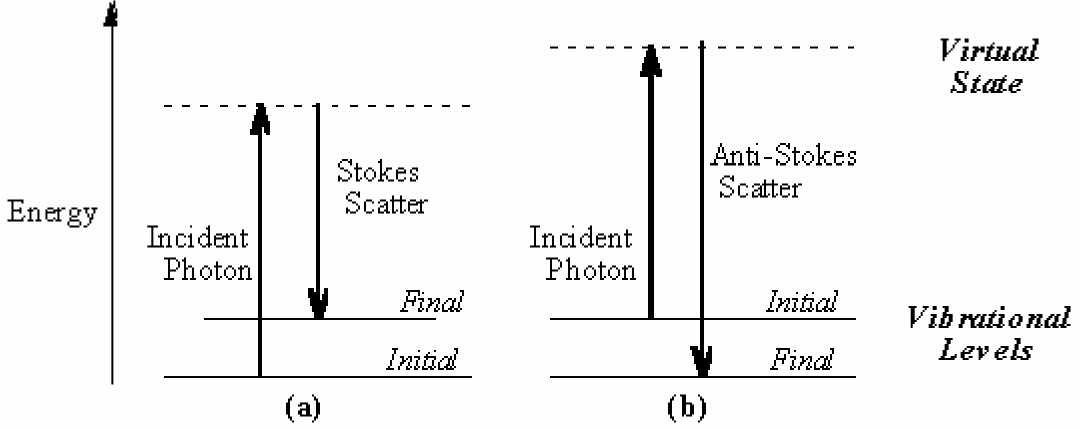

Figure 6: Raman scattering energy diagram: Raman Stokes diffusion, Raman Anti-Stokes [23].

a- First order Raman effect

During diffusion process, the energy is conserved and at each step the conservation of the wave vector must be ensured. In the initial state, a solid is in the ground state where only the valence states are occupied. The process of the Stokes diffusion can be represented by six processes. One of these processes is described in three steps, in a first step, an incident photon of energy $E_i = h\omega_i$ and wave vector $\vec{k}_i$ created by absorption to energy $\vec{E}_a(\vec{k}_i)$ an electron hole pair. This transition is virtual. However, it can be real if the incident energy $\vec{E}_i$ corresponds to $\vec{E}_a(\vec{k}_i)$. An intra - band diffusion of an electron by a phonon takes place and the electron - hole pair is brought to $|b\rangle$ an energy state $\vec{E}_b(\vec{k}_d)$. Finally, the crystal returned to the ground state, where a recombination of the electron-hole pair occurred following the emission of a photon of energy E_d [12, 14]. The photons frequencies are much higher than that of the phonons resulting $\|\vec{q}\| \langle \; 2\|\vec{k}_i\|$ very close to centre area. Thus, only zone centre phonons participate in a first order Raman process (Figure 7).

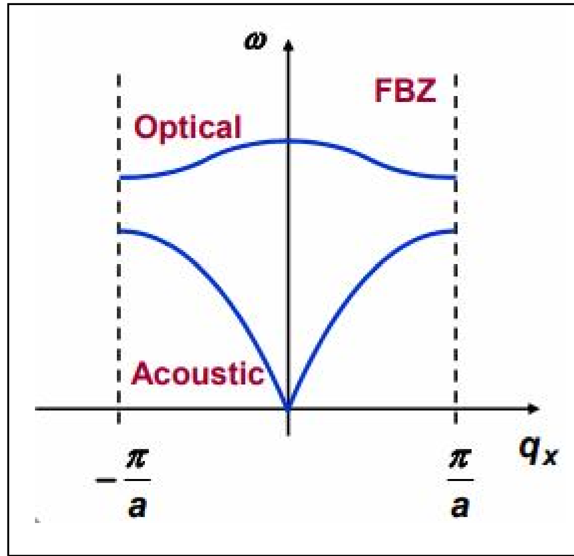

Figure 7: The Brillouin zone centre phonons only participate in the Raman effect [24].

For this approach, the amplitude of probability during a Raman scattering is written:

$$A = \frac{\langle n, E_a, N+1 | H_{photon/e-} | n, 0, N \rangle \times \langle n-1, E_b, N+1 | H_{e-/phonon} | n-1, E_a, N \rangle \times \langle n, 0, N+1 | H_{e-/photon} | n-1, E_b, N+1 \rangle}{(\hbar\omega_i - E_a)(\hbar\omega_d - E_b)}$$

Here, $|n, E, N\rangle$ represents the state vector, where n is the number of photons, N is the number of phonons and E is the energy of the corresponding electron state.

$H_{photon/e-}$ = Hamiltonian interaction electron photon.

$H_{e-/phonon}$ = Hamiltonian interaction electron phonon.

$H_{e-/photon}$ = Hamiltonian electron photon interaction.

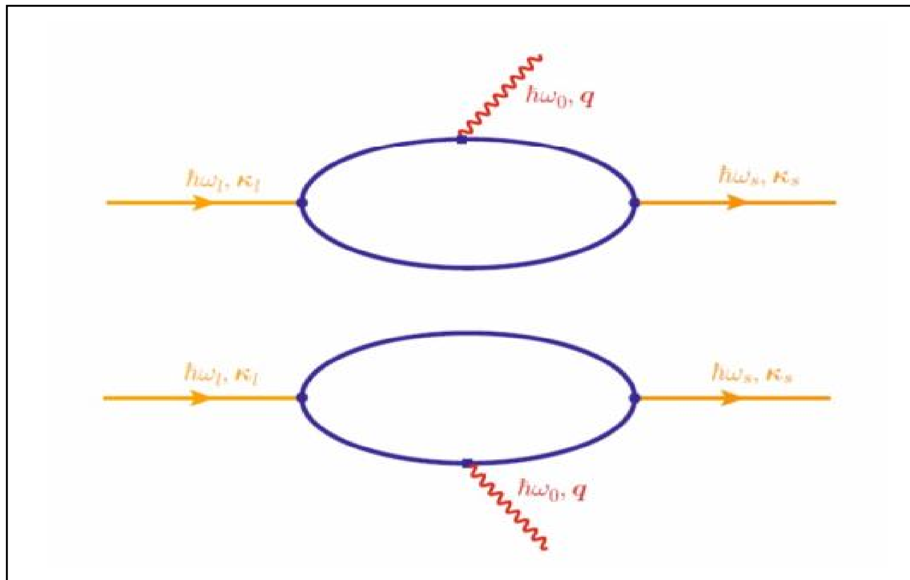

Figure 9: Feynman diagram of Stokes and Anti-Stokes scattering [24].

b- Second order Raman effect

During a second-order Raman process two phonons are involved. These phonons are characterized by a sum of zero wave vectors. Thus, all the phonons of the Brillouin zone will be considered. Three types of processes can be distinguished in this case:

a- Simultaneous creation or annihilation of two phonons.

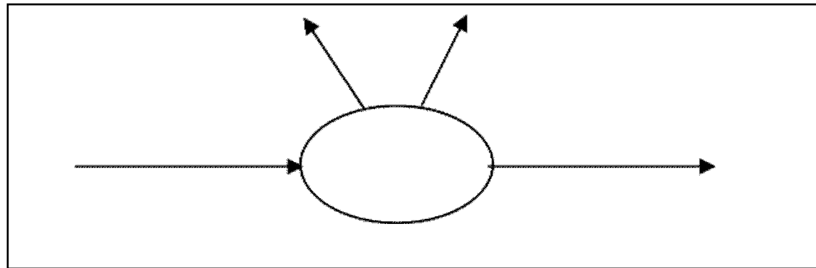

b- Separate creation or annihilation of two phonons.

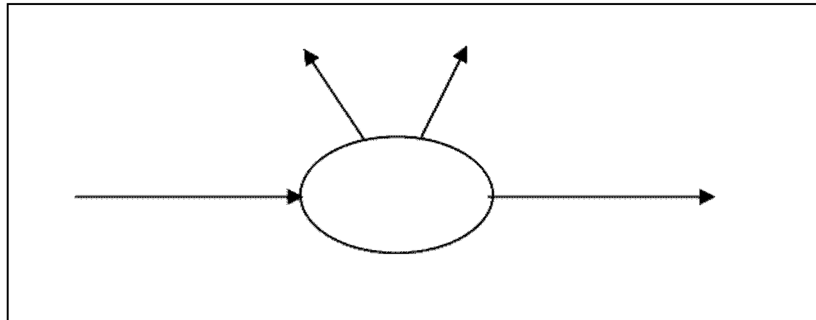

c- The creation or annihilation of two phonons will take place by the succession of two processes of first order.

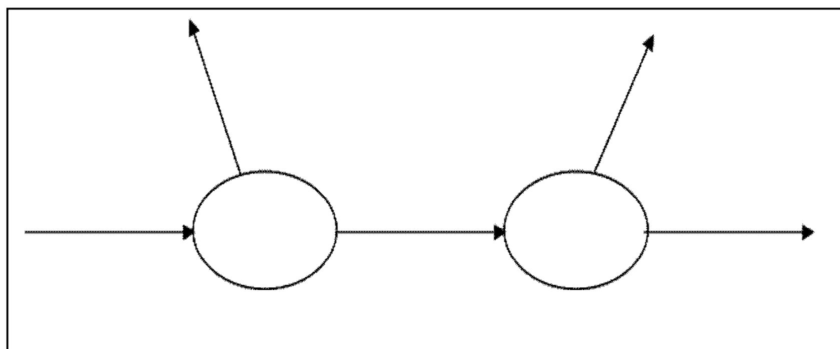

c- Raman polarization effect

Raman scattering is partially polarized even for cases characterized by any orientation such as gases, molecules, etc. For an isotropic medium, the polarization results from the variation of the components of the dipole induced in space with respect to the coordinates of the system studied. A Raman scattering tensor is given by

$$I \propto \left|\vec{e}_i . R . \vec{e}_d\right|^2 ,$$

where $\vec{e}_e$ and $\vec{e}_S$ are the vectors of polarization of the incident wave and that diffused.

R is the Raman tensor, $R = \left(\frac{\partial \alpha}{\partial u}\right)_0$ where u: is the phonon vector, α: is the polarizability.

Thus, the Raman intensity depends on the polarizability tensor of the crystal. For example, for a cubic crystal Zincblende the R is given by $\{R_x, R_y, R_z\}$.

$$R_x = \begin{pmatrix} 000 \\ 00d \\ 0d0 \end{pmatrix}, R_y = \begin{pmatrix} 00d \\ 000 \\ d00 \end{pmatrix}, R_z = \begin{pmatrix} 0d0 \\ 00d \\ 000 \end{pmatrix}$$

In this case, the Raman intensity is given by

$$I \propto \left|\vec{e}_i . R . \vec{e}_d\right|^2$$

$$I \propto \left|\vec{e}_i . \left[\vec{e}_x R(x) + \vec{e}_y R(y) + \vec{e}_z R(z)\right] . \vec{e}_d\right|^2$$

With $\vec{e}_x$, $\vec{e}_y$, $\vec{e}_z$ are respectively the components of the polarization of the phonon.

The study of polarization determines the intensity in different configurations such as intensity in perpendicular polarization $I_\perp$ and parallel polarization $I_\parallel$. Thus, we can calculate the depolarization ratio ρ which is given by:

$$\rho = \frac{I_\perp}{I_\parallel}$$

Based on the obtained ρ value, the nature of the Raman bands can be determined [12].

d- Experimental set up

We have a high resolution LabRAM denoted "LabRAM HR- HORIBA". It is a simple monochromator (Figure 10). This simple mode is used for the highest sensitivities.

Figure 10: LabRAM HR spectrometer (Jobin yvon).

This system contains:

- A detection system: A CCD is available, characterized by a spectral response covering the broadband between (250 - 800nm).
- A simple stage with a confocal microscope. The latter is used to visualize the surface of the sample and probed the existing vibration modes.
- Sample cooling system between 193 ° C.
- A computerized system for the management and management of data.
- The source of the incident signal is a laser covering the visible range.

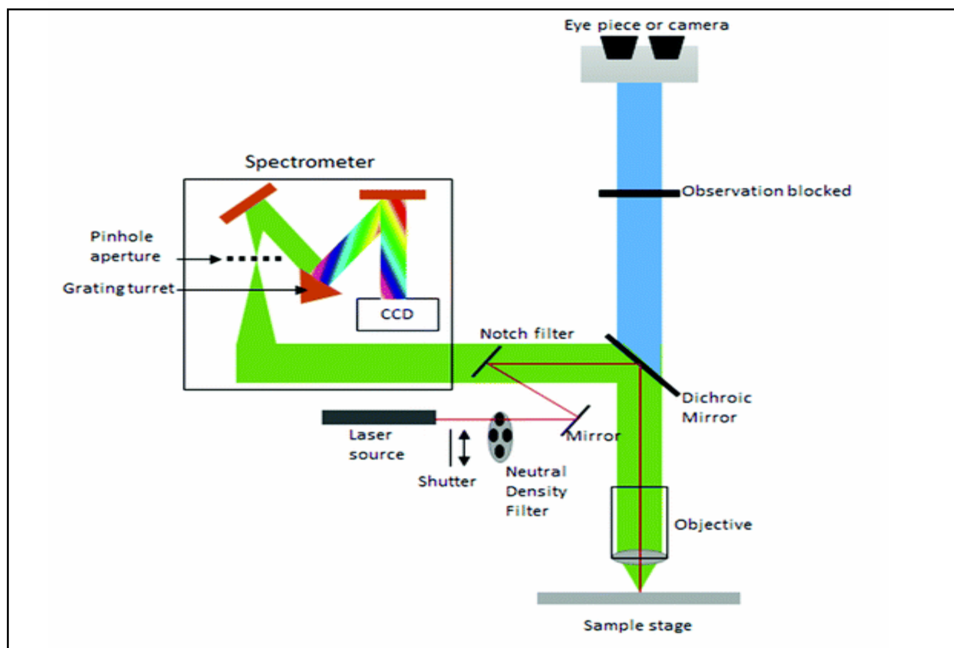

Figure 11: Raman measurements process [25].

5- Photoelectric effect

In 1887, Heinrich Hertz discovered a particular response of electrodes illuminated with ultraviolet light. Here an electric sparks appears [26]. Later in 1900, while studying black-body radiation, Max Planck shows that the energy carried by electromagnetic waves could only be released in "packets" of energy. Five years later, Albert Einstein published a paper advancing the hypothesis that light energy is carried in separate quantized packets in order to clarify photoelectric effect experiment. This model improved the quantum mechanics field. This study was later illustrated by Robert Millikan's experiment at 1914. Finally, Einstein was awarded the Nobel Prize in 1921 for "his discovery of the law of the photoelectric effect". Later in 1923, Millikan was awarded by the Nobel Prize for "his work on the elementary charge of electricity and on the photoelectric effect".

5-1- Principal

The photoelectric effect is based on the emission of electrons when light comes on top of the material (Figure 12). The classical electromagnetic theory explains such phenomena to the exchange of energy from the light to electron. Here, an alteration in the intensity of light would transforms the kinetic energy of the electrons emitted from the metal. Accordingly, sufficient light appears between the initial light and the subsequent emission of an electron. Nevertheless, the experimental results did not agree with those given by the classical theory. Here, electrons are moved only by the impingement of photons when those photons reach or exceed a threshold frequency (energy). Below this latest, no electrons are emitted from the metal for any case of the light intensity or the length of time of exposure to the light (hardly ever, an electron will be released by absorbing two or more quanta.

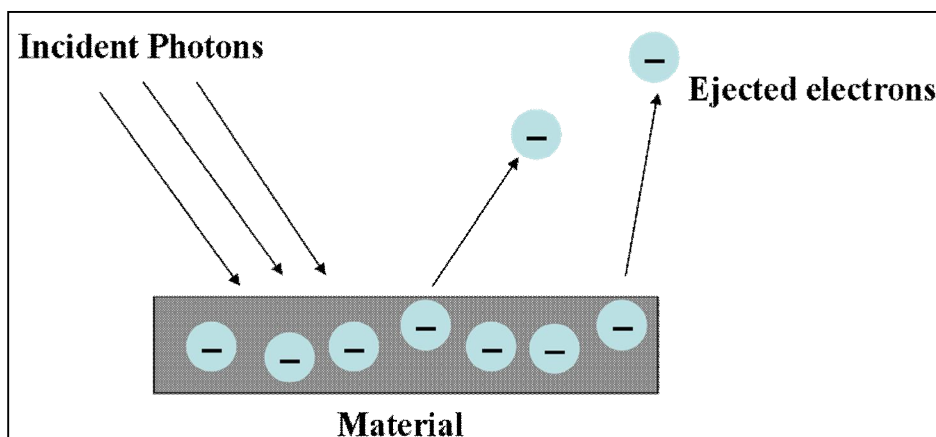

Figure 12: Photoelectric effect.

5-2- Experimental set up

During our research, the voltage and resistance characteristics of the graphene layers were determined based on this approach. We used a Keithley 2400 source meter. We applied separate illumination systems, i.e. red, green and violet lasers. The sample contacts were held in place using silver epoxy. We used a four contact configuration. The measurements were taken by customized programs written with the LabVIEW® software.

III- Conclusion

In this chapter, we have just recalled the different surface characterization techniques used in this thesis. We detailed the characteristics of atomic force microscopy (AFM) and the limit of its sensitivity to the surface such as the graphene - substrate interface. We have just given an overview on ultrasonic force microscopy "UFM" and its utility to analyze the response nano-mechanical responses of the graphene layer. We have presented the principle of Raman scattering and its experimental set up. Finally, we have detailed the characteristics of the photoelectric effect.

References:

[1] Michael W. Davidson and Mortimer Abramowitz, OPTICAL MICROSCOPY

[2] G. Bining and H.Rohrer. Reviews of Modern physics, 59: 615-630, 1987.

[3] G. Binnig, H. Rohrer, CH. Gerber, and E. Weibel. *Tunneling* Applied Physics letter, 40: 178- 200, 1982.

[4] M.Bienias, S. Gao, K.Hasche, R. Seemann, and K. Thiele. Applied physics, 66: 837-842, 1998.

[5] G. Binnig, C.F. Quate and C.H. Gerber, Phys. Rev. Lett. 56(9), 930–934, 1986.

[6] J.N. Israelachvili, D. Tabor, Proc. Roy. Soc. London A, 331, p.19, 1972.

[7] A.G. Khurshudov, K. Kato, H. Koide, Wear, 203-204, p.22, 1997.

[8] Seiji Akita, Hidehiro Nishijima, Yoshikazu Nakayama, Fuyuki Tokumasu and Kunio Takeyasu, J. Phys. D: Appl. Phys., 32, p.1044, 1999.

[9] H.C. Hamaker. Physica IV, 10: 1058-1072, 1937.

[10] J.N. Israelachvili, Academic Press London, 1992.

[11] Robert A. Wilson and Heather A. Bullen,* Department of Chemistry, Northern Kentucky University, Highland Heights, KY 41099.

[12] The Raman Effect A Unified Treatment of the Theory of Raman Scattering by Molecules, by John Wiley & Sons Ltd, Baffins Lane, Chichester, West Sussex PO19 1UD, England, 2002.

[13] J.L. Koenig, Volume 12, Number 2, 2001.

[14] Raman spectroscopy for soft matter applications, A JOHN WILEY & SONS, INC publication, 2009.

[15] G. Bining and H.Rohrer, Reviews of Modern physics, 59: 615-630, 1987.

[16] G. Binnig, H. Rohrer, CH. Gerber, and E. Weibel.. Applied Physics letter, 40: 178- 200, 1982.

[17] Micro-Raman spectroscopy to study local mechanical stress in silicon integrated circuits, Semicond. Sci. Technol. 11 139–154. Printed in the UK, 1996.

[18] Introduction to Laser Spectroscopy Halina Abramczyk, Elsevier, 2005.

[19] R.Loudon, Adv.Phys. 13, 423, 1964.

[20] Théorie des groupes et symétrie : de l'atome au solide. Daniel Malteree P 39.

[21] The Raman Effect A Unified Treatment of the Theory of Raman Scattering by Molecules, by John Wiley & Sons Ltd, Baffins Lane, Chichester, West Sussex PO19 1UD, England, (2002).

[22] Raman spectroscopy and regenerative medicine: a review Katherine J. I. Ember, Marieke A. Hoeve, Sarah L. McAughtrie, Mads S. Bergholt, Benjamin J. Dwyer, Molly M. Stevens, Karen Faulds, Stuart J. Forbes & Colin J. Campbell.

[23] http://www.renishaw.com

[24] ECE 407 – Spring 2009 – Farhan Rana – Cornell University

[25] Raman spectroscopy: an evolving technique for live cell studies, Rachael Smith, Karen L. Wright and Lorna Ashton, journal RSC, C6AN00152A, 2016, 141, 3590-3600

[26] F. W. Zemansky, M. W. young, H. D. University Physics (6th ed.). Addison-Wesley, 843–844. ISBN 0-201-07195-9, 1983.

Chapter 3:

Graphene Localisation from variation of mechanical to electrical properties

I- Introduction

Raman spectroscopy is a powerful tool for rapid and non-destructive characterization of different materials. This spectroscopy was widely used for atomic scale material such as graphene. Indeed, Raman allows the analysis of the various properties of graphene such as: defects, the number of layers, mechanical and electrical properties. On other hands, the high quality of the Raman mappings of the sample surface illustrates the possible change in the surface morphology of the graphene layer [1].

II- Raman spectra

1- Silicon Carbide

- **SiC polytypes**

Different SiC polytypes are used for epitaxial graphene growth. Nevertheless, the most repeated polytypes are: 6H-SiC, 4H-SiC hexagonal and 3C-SiC cubic with their two polarities face terminated "silicon" Si "or" C "carbon. SiC hexagonal polytypes are generally denoted nH, where n corresponds to the number of SiC bilayer in the unit cell. Raman determines their possible structural changes affected by the high growth temperature. The increase of the SiC bilayers from 1 to n along the hexagonal stacking axis induces a division of the Brillouin zone by n in the direction of the reciprocal lattice. Consequently, a folding of the dispersion curves along the direction of the reciprocal lattice appears. The dispersion curves of the polytypes nH or 3nR are obtained from the 3C-SiC polytype. This occurs by dividing the Brillouin zone of 3C-SiC by n [2]. The division by the number of bilayer n results at the level of the Brillouin zones a folding of the dispersion curves of the polytype 3C-SiC. This folding will be in the direction of the reciprocal lattice corresponding to the direction c of the crystal. Thus, new modes appear at the edge of the Brillouin zone, point Γ (q = 0), appear.

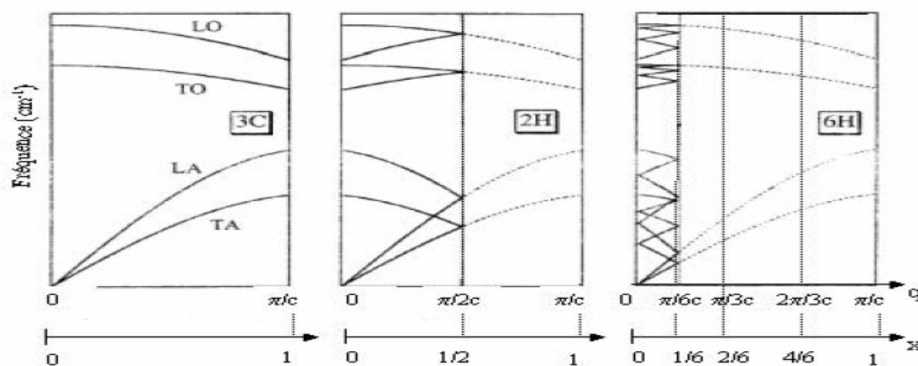

Figure 1: The folding of transverse and longitudinal modes at the edge of Brillouin zone of 3C-SiC originating 2H and 6H-SiC polytypes [2].

- **Raman Spectrum of SiC**

We used a laser wavelength λ = 488 nm = 2.54eV for the spectra acquisition. This exciting wavelength is the only wavelength used in our work. The Raman spectra of the different SiC substrates are investigated between [100 - 1000 cm^{-1}], where different Raman modes of the first and second orders of SiC exist. Figure 2 illustrates typical Raman spectra of different polytypes of the SiC substrate. Figure 2-a is associated to the Raman spectrum obtained for 3C-SiC (100) / Si (100). We located the first-order Raman modes T_2 (TO) and T_2 (LO) at 796.55 cm^{-1} and 972.41 cm^{-1}, respectively [3]. Furthermore, two new modes at 302 and 521 cm^{-1} are observed which are associated respectively with the vibration modes of Silicon 2 TA (X) and TO (Γ). Figure 2-b represents the Raman spectrum of 4H-SiC, several modes have been distinguished. The main Raman modes are respectively the E_1 (low), E_2, E_1 (TO), and A_1 (LO) located at 270, 770, 791, 967 cm^{-1}. Furthermore, two new low intensity modes appear at 154 and 245 cm^{-1}. These modes correspond to E_2 (high) and E1 (high) modes, respectively of 6H-SiC. The typical Raman spectrum of the 6H-SiC substrate is given in Figure 2-c. Four modes of broad intensity are observed at 765, 787, 795 and 964 cm^{-1}, they are assigned to E_2, E_2, E_1 (TO), A_1 (LO). In addition, other low-intensity peaks are also observed at 154, 245, 507 and 516 cm^{-1} respectively corresponding to E_2 (high), E_1 (high), A_1 (low) and A_1 (high) [4-5].

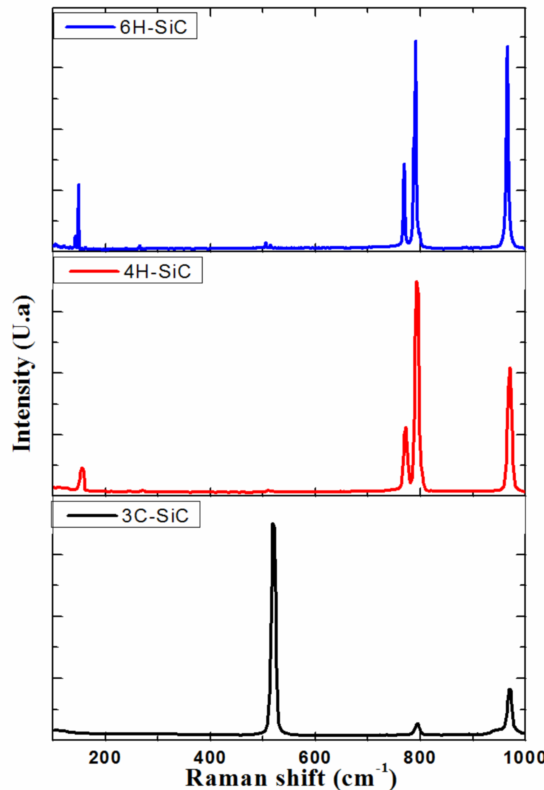

Figure 2: Raman spectra of the different SiC substrate polytypes.

2- Graphene Raman spectra

Various properties can be deduced from a Raman spectrum obtained from graphene such as: Defects, The number of layers, strain effect and doping. Raman spectra registered at different points in the sample surface in the frequency range between [1000-3000 cm^{-1}] (Figure 3).

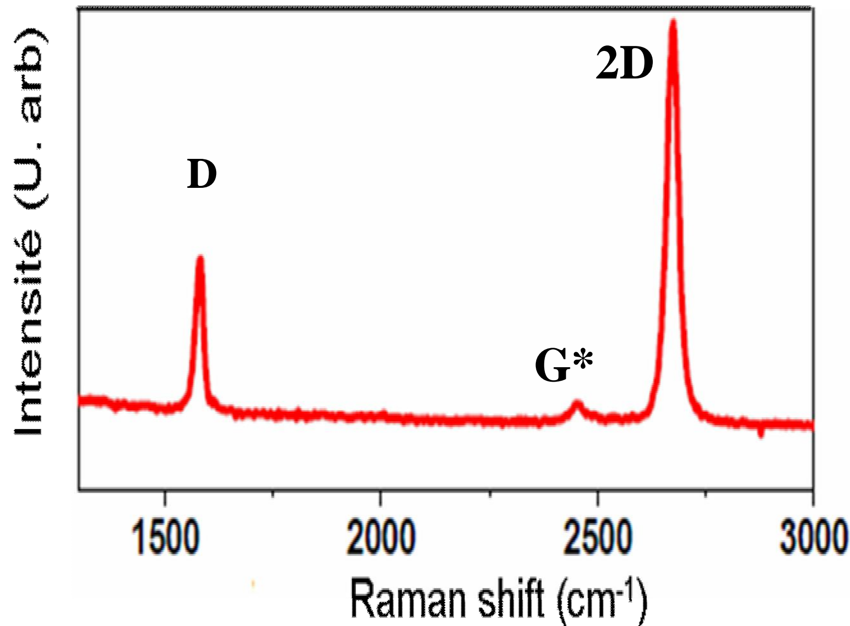

Figure 3: Raman spectra of ideal graphene [6].

We located all the Raman modes of the graphene, such as the D, G and 2D bands [7–9]. The G-band is a doubly degenerate (TO and LO) phonon mode (E_{2g} symmetry) at the Brillouin zone centre (Figure 4). The D-band is assigned to phonons on the K point and defects [10, 11] (Figure 4). The 2D band is associated with 2TO. We investigated the Raman mapping of the D band. The D-band spectra showed mostly low intensity (Figure 4). This could be associated mainly with oxygen impurities present in epitaxial graphene layers. High intensity in the D-band is normally induced by structural defects found in epitaxial graphene on face terminated carbon. The G * mode observed at 2687 cm^{-1} corresponds to a combination of a TO phonon and a LA phonon. It is presence is a signature of a monolayer of graphene. Indeed, the increase in the number of layers results in the widening of this mode and the decrease in its intensity.

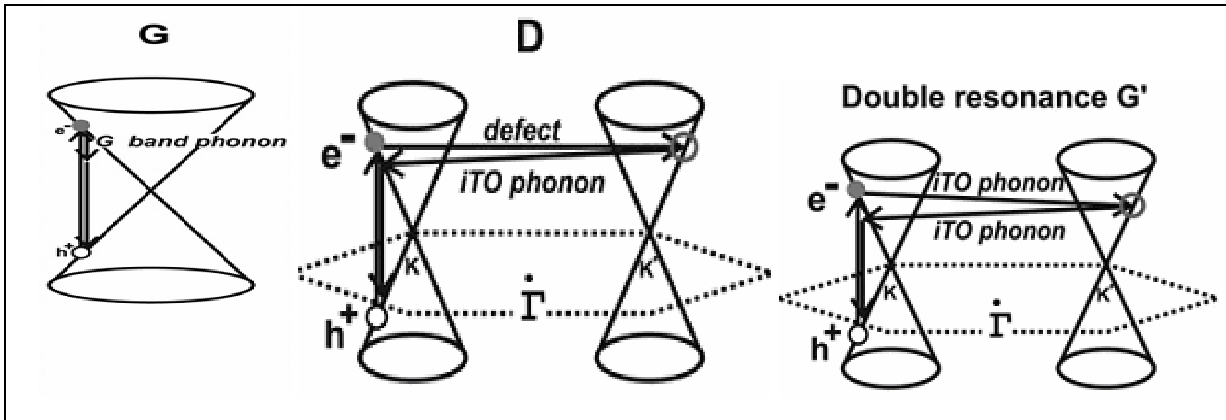

Figure 3: Graphene Raman modes.

III- Mechanical properties investigation

1- Epitaxial graphene macro-island

We investigated epitaxial graphene grown on 4H-SiC ($000\bar{1}$) substrate using optical microscope at room temperatures. The large homogeneous area has been was associated with macro-island (Figure 4- a). Macro-island localisation helps determining epitaxial graphene properties. The size of the grown macro-island is larger than the size generally observed. This island was produced intrinsically during the epitaxial growth. It shows an excellent tool to study both tensile and biaxial strains. Indeed, mechanical properties of epitaxial graphene remain unable to specify the strain variation due to the hard location of the graphene layers [19, 20].

We start with the optical contrast study. This latest is high compared to ordinary graphene. We observed a visible darker flake of brown colour in the centre (SZ_1) surrounded by a lighter area from outside (SZ_2) (Figure 4-a). This optical image illustrates the size of the graphene macro-island that was identified using interference colour observed in the optical microscope. We also investigated the formation of macro-island using local mapping of intensity and spectral position of graphene Raman active modes associated to the D, G and 2D bands (Figure 4- b, c and e)). Raman spectra exhibit a particular behaviour at the centre of this macro-island. They indicate a signature of four layer graphene in the macro-island. The G band has a high intensity, especially at the centre and so the 2D band becomes broader. This was confirmed by the full width at half maximum (FWHM) measurements of the 2D band correlated with the intensity ratio of G and 2D band (I_G/I_{2D}).

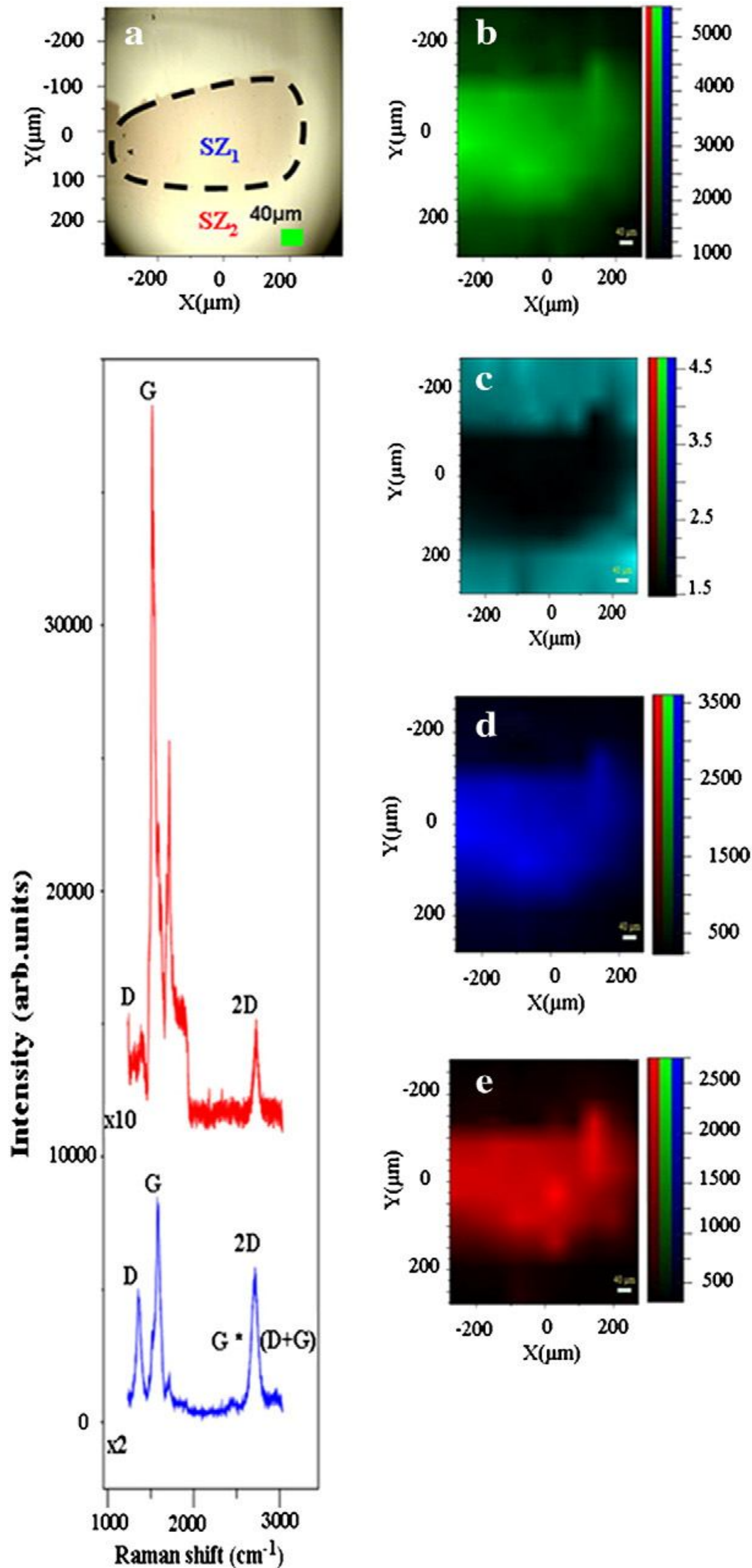

Figure 4: Raman spectra, SZ_1 and SZ_2 of graphene layers taken inside (Z_1) andoutside (Z_2) areas of the main flake. Inset: (a) Optical microscopy image of graphene layers grown on 4H-SiC, (b)mapping Raman intensity (MRI) of G band, (c) MRI of 2D band, (d)mapping Raman intensity (MRI) of the ratio of G/2D band, i.e. I_G/I_{2D} ratio, and (e) MRI of D band of the graphene flakes.

2- Strain distribution analysis

To study the strain distribution in the macro-island the Raman measurements, we carried out in regular locations with small step of 50µm along horizontal and vertical directions across the macro-island flake. Raman spectra have been checked in each point of the sample surface using an auto focusing adjustment of the laser beam acquisition. We identified a set of first and second order Raman modes between 1000 and 3000 cm^{-1}. The typical spectra of each area were presented in Figure1. We will focus our discussion on the central flake which has the largest area forming the macro-island. The defect Raman mode (D band) is located at 1360 cm^{-1} (Figure 4). The second G band sited at 1587 cm^{-1} is assigned to the E_{2g} in-plane vibration modes (Figure 4) [3, 22]. We have also located G*, 2D and (D + G) bands and studied their changes depending on the position on the macro-island (Figure 4). The G* band appears at 2447 cm^{-1} indicating an intervalley process involving one TO and one longitudinal acoustic (LA) phonons [13, 14]. The 2D band at 2720 cm^{-1} associated with a double resonant excitation of two phonons having opposite wave vectors at *K* point in the Brillouin zone [7]. The (D + G) band observed at 2946 cm^{-1} is signature of defects in the graphene layers. The layer number **n** of epitaxial graphene grown on 4H-SiC have been identified based on the correlation between the full width at half maximum (FWHM) of the 2D band and the ratio (I_G/I_{2D}). The FWHM of the 2D band across the investigated macro-island shows an order of 90 cm^{-1} (Figure 5-a). Previous studies have reported in Ref. [8, 9, 10] that, the I_G/I_{2D} ratio less than 0.5 corresponds to a single layer, in the range [0.5 - 1] to bi-layer and greater than 1.8 (n> 5) to multilayer of graphene. We found an (I_G/I_{2D}) of 1.5 inside the macro-island (Figure 4-d). Thus, we have determined the layer number **n** of graphene of the localised macro-island to four layers [8, 9].

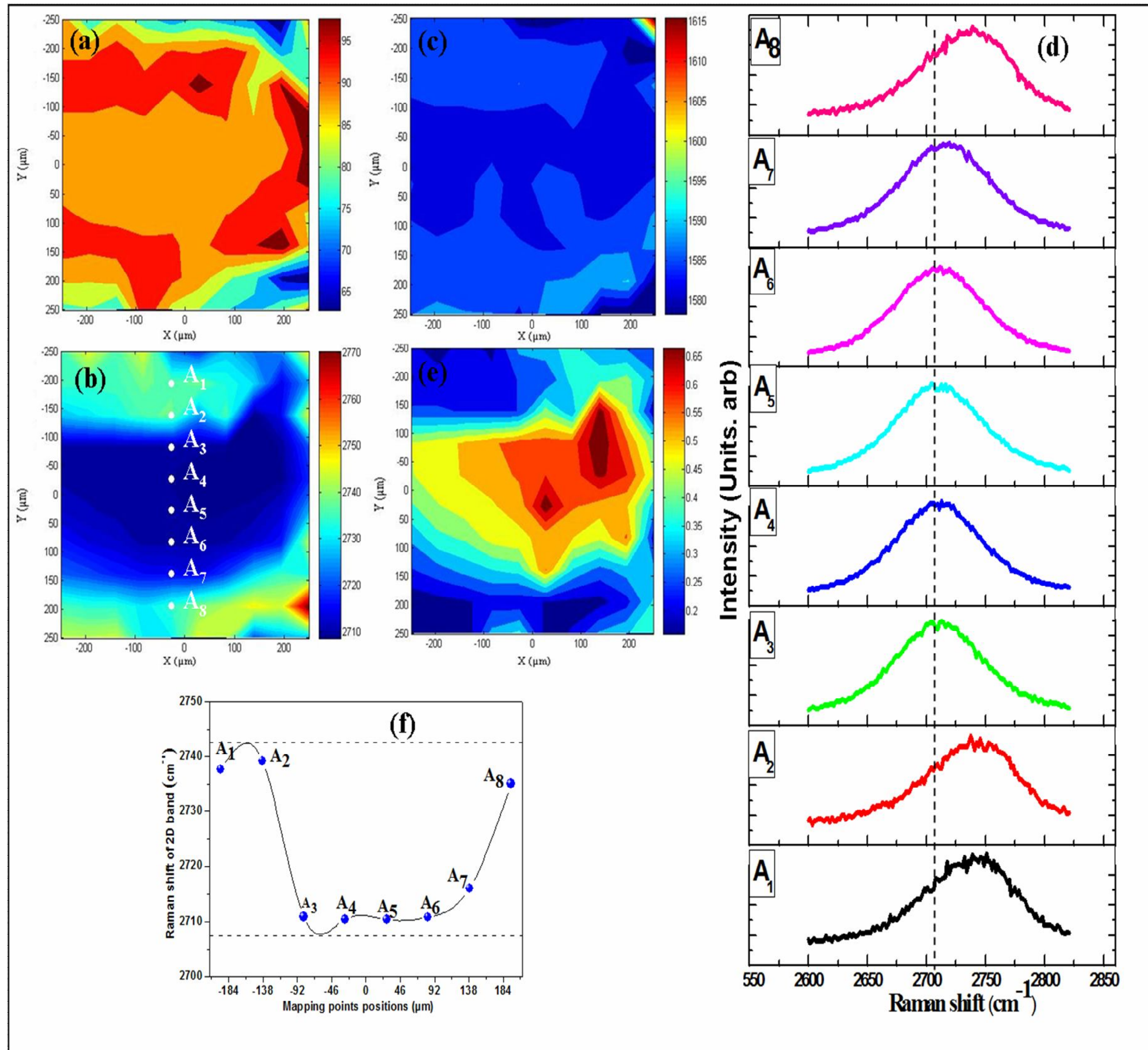

Figure 5: The mapping of the Raman spectra to the surface of the sample measured at room temperatures: a- the mapping of the FWHM of the 2D band, b- the mapping of frequency associated with the peak of the 2D band, c- the mapping of peak frequency of the G band, d- the evolution of 2D band shape obtained for a line scan taken along vertical, y direction at the coordinate, x = −27 µm, e- the mapping of peak intensity ratio, i.e. I_D/I_G ratio, and f- the variation of a frequency associated with the 2D band peak for a line scan taken along y direction at the value x = −27 µm.

3- Strain effect

Raman mapping analysis is a good tool for elastic strain characterization of the four layers macro-island. We focus our discussion the graphene G, and 2D bands measured at room temperature on the macro-island. The adjustment of the 2D band using a Lorentzian curve gives a FWHM values in the range of [87- 94 cm^{-1}] (Figure 5-a). These FWHM values correlated with the intensity ratio of the G and 2D bands represent four layers graphene, as discussed above. The FWHM values are homogeneous in the centre of this macro-island. They became larger in the vicinity of the foundations of the island. Different foundation sides of this

island the strain is inhomogeneous (Figure 5-a). Figure 5-b shows 2D peak frequency mapping that varies in the range [2732 - 2716 cm^{-1}] (Figure 5-b and c). We note a blue shift for both 2D and G bands, respectively of the value approximately, 16 and 10 cm^{-1}. The blue shift increases from the centre of the main flake to the edge of the island [6]. We studied in detail the 2D band variation using a line scan a long y axes is taken in the spatial interval from -194 µm to 194 µm (Figure 5-d). We considered a fixed x- position, **i.e.** x= -27 µm in the island. The Raman spectra of 2D band obtained for all investigated points demonstrate the changes observed in the described mapping. The map exhibits a symmetric behaviour from both sides of a big uniform area located at the centre of this island, even in spite of the small variation of the central position of the frequency for each Raman band observed inside this area (insert, Spectrum 2- taken in the following location spots: A_3, A_4, A_5, A_6). On other hands, we notice a significant frequency blue shift far from the central area of the island on both sides (Raman Spectrum in A_1, A_2, A_7, A_8). Here, the substrate effect plays an extra role of negative pressure. Therefore, we expect some decompression to happen. The frequency of the 2D Raman band across this island changes from 2710 cm^{-1} to 2739 cm^{-1} (Figure 5-f). This blue shift differed to common graphene grown on SiC face termination C, where the high decoupling between graphene layer and substrate reduce of strain effect [15]. This blue shift could not be attributed to charge transfer from the substrate. This is due to the charge decreases by increasing graphene layer number. In fact, the high electron concentration of single layer of graphene has a of 7 cm^{-1} Raman shift of the G band [7, 16-20]. Accordingly, a decrease of the Raman shift is expected with increasing layer number, where a diminution of the electron concentration appears in the graphene sheets. This confirms our results eliminating the charge transfer effect as origin of the high blue shift that is 7 cm^{-1}, specially, with the localised layer number i. e four layers graphene. Similarly, the large 2D band shifts verifies also this condition revealing the weak amount of charge transfer in this island.

We compared our results to those of four layers exfoliated graphene. Similar blue shifts were located for both G and 2D bands. The G band peak appears at 1582 cm^{-1} while the 2D band peak appears at 2682 cm^{-1} [7]. Each mode has a blue shift of 5 cm^{-1} and 38 cm^{-1}, respectively. This illustrates that the behaviour observed here is mainly due to the strain effect arising at the formation of this large epitaxial island. Our results are consistent with previous work, where strain effects in epitaxial graphene are associated to the located blue shifts of 2D and G bands. Contrary to exfoliated graphene the frequency shifts of the Raman modes and strain effects are significantly weaker [7]. The obtained values for Raman band shifts are close to ones reported in previous work [7]. They reported similar effects for epitaxial graphene

grown on 6H-SiC face terminated Si, that is on samples very different from our ones [15]. Here, our sample is grown on 4H-SiC substrate face terminated C. The origin of this similarity has been investigated using the Raman intensity ratio for D and G peaks, I_D/I_G. Indeed, we observed a similar behaviour of isolated Raman spectrum in the main flake of which the macro-island (Figure 5-e). This reveals the good quality of graphene layers on the island elaborated here. Thus, the origin of the blue shift obtained for both Raman modes could only be attributed to mechanical properties of four layers of graphene and strain effect arising at the formation of the macro-island.

3-1- Temperature effect on a formation of strain in epitaxial graphene

We ascribed the Raman mode changes to the strain effects in the macro-island. Indeed, it shows also strong temperature dependence and a high sensitivity on the layer number. G and 2D graphene modes highly depend to temperature [21]. We start by investigating the temperature dependence of the 2D band frequency at 77K. The temperature decrease from 300K to 77K induces a blue shift of the peak frequency and the FWHM increase of the 2D band (Figure 6-a and b). As for exfoliated graphene strain effects increase with the temperature [22, 23]. This is signature of a thermal expansion or contraction with the temperature. We presents in Figure 6-c the line scan of 2D Raman band taken in the main flake along y axes in the interval [-194, 194] µm at x = -27 µm. Here one may clear see that both Raman frequency blue shift and FWHM of the G band increases as the temperature decreases. In fact we found a linear temperature dependence of the frequency position of G and 2D Raman bands where the negative temperature–frequency shifts coefficient χ_G = - 0.022 cm^{-1} K^{-1} and χ_{2D} = -0.030 cm^{-1} K^{-1}. The χ_G is smaller than one located in monolayer and bilayer of exfoliated graphene. In fact, the $\chi_{G\ (bilayer\ exfoliated)}$ is about -0.0154 cm^{-1} K^{-1}. We expect a decrease of G band shift coefficients with increasing the layer numbers. However, χ_{2D} is larger with respect to a small number of graphene layer, where χ_{2D} of bilayer of exfoliated graphene $\chi_{2D\ (bilayer\ exfoliated)}$ corresponds to -0.066 cm^{-1} K^{-1} [21- 24]. Here, the phonon frequency shift with varying temperature is associated here to the strain and could be attributed primarily to the thermal expansion of the four-layer the macro-island. Different factors may contribute like: graphene-substrate interaction, electron-phonon coupling and an-harmonic phonon-phonon interactions [21]. For the G band, some effects could be neglected like the anharmonic contribution due to its small value in the temperature range [77-300 K] [21]. Thus; we conclude that the negative thermal expansion coefficient cannot be the only origin of the negative sign for the frequency shift as reported in

Ref. [21]. This negative sign is assigned to both Gruneisen parameter and thermal expansion coefficient [21]. Furthermore, the χ_{2D} value of epitaxial graphene is larger in comparison to that of bilayer of exfoliated. Therefore, the blue shift of the 2D bands observed with decreasing temperature could be attributed likewise to the thermal expansion effect of both substrate and the four graphene layers. Correspondingly, the FWHM temperature coefficient for both G and 2D bands shows the same temperature dependence. The value τ_G is negative (τ_G = -0.004 cm^{-1} K^{-1}) while τ_{2D} of 2D band is positive (τ_{2D} = 0.011 cm^{-1} K^{-1}).

3-2- Estimation of the strain effect on graphene modes

We demonstrated the strain effect on Raman modes using a theoretical model calculation. Previous studies have shown that the strain of graphene materials, ε for both Raman modes 2D and G, have been given with the following expressions [19, 25, 26]:

$$\varepsilon_{2D} = \left(\frac{\Delta\omega}{\omega_{02D}} \right) / \gamma_{2D} \quad (1)$$

$$\varepsilon_{G} = \left(\frac{\Delta\omega}{\omega_{0G}} \right) / \gamma_{G} \quad (2)$$

where ω_{02D} (ω_{0G}) is the frequency for the peak of the 2D (G) bands of exfoliated graphene, the value $\Delta\omega$ is the difference between the Raman frequency of the epitaxial graphene under the strain effect and of the graphene free of strain, γ_{2D} (γ_G) is the Gruneisen parameter of 2D (G) band of graphite (with γ_{2D} = 2.7 and γ_G = 1.8) [19].

Figure 7 and 8 represent the 2D and G bands mapping of strain effects in a percentage with respect to a suspended graphene. The corresponding mapping of the 2D band demonstrates different ranges of strain variation between [0.2- 0.6 %]. The mapping shows two areas. One presents a big homogeneous flake of the macro-island (Figure 7). This is surrounded by the island foundation-boundaries. However, the areas outside the island have an inhomogeneous with the strain. Interesting, we localised an increase of the strain value at the edge of the main flake that is an obvious influence of the substrate. The strain homogeneity in the central main flake confirms the high quality of elaborated graphene in the macro-island. Thus, the strain variation outside of the main central area of the flake is assigned to graphene-substrate interaction. This originates from to the difference between the lattice constants of the graphene layer and the SiC substrate where the graphene of the island and the substrate are bound [12].

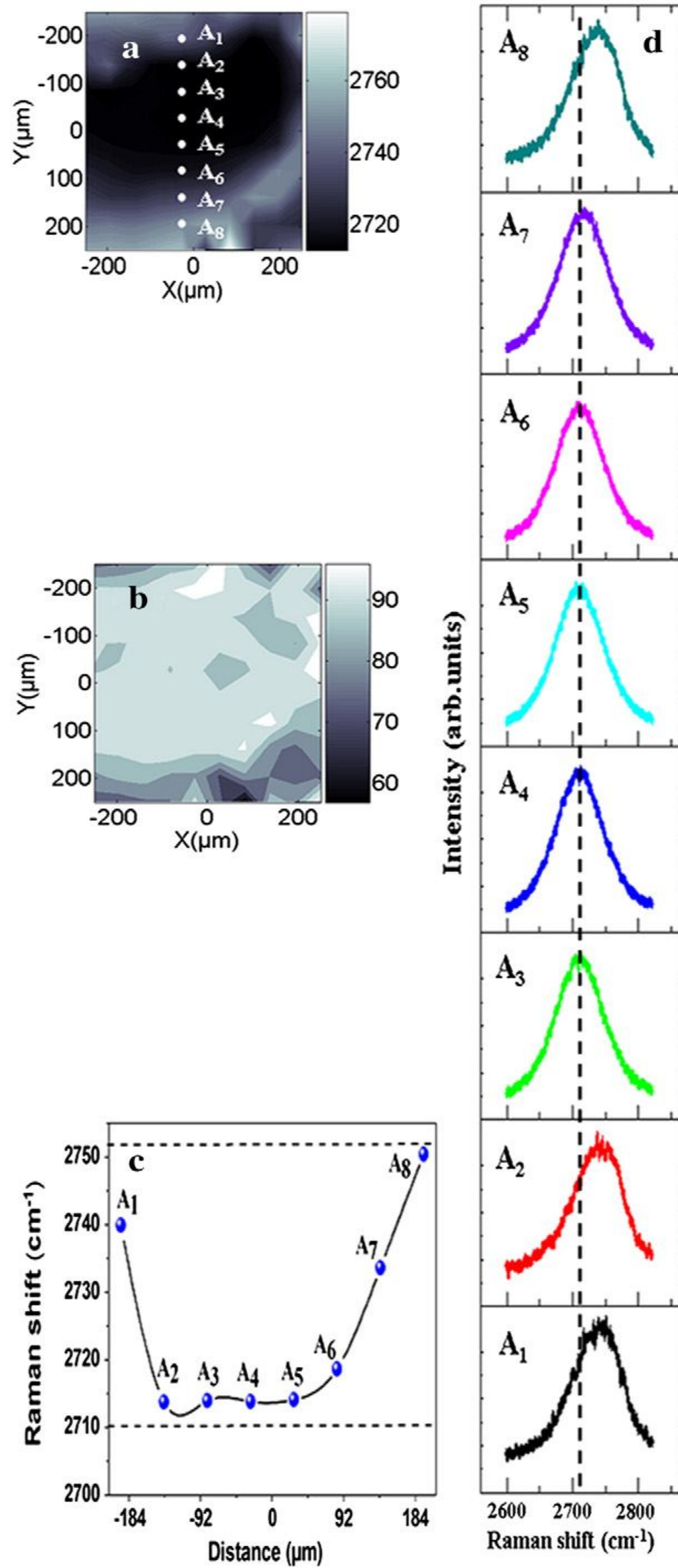

Figure 6: Raman mapping- the spectroscopic map of the central position and the bandwidth of the 2D band measured at various points on the surface of the central epitaxial graphene flake at 77 K: a-the Raman frequency mapping for the 2D peak taken with high resolution in regular positions on a lattice is indicating a smooth variations, b- the same procedure is

applied to obtain the FWHM mapping, c- evolution of the Raman shift for the 2D band taken on the scan along y-direction at the fixed value x = −27 µm, and d- evolution of the shape and the position of the 2D band measured on the scan along y-direction at the fixed value x = −27 µm.

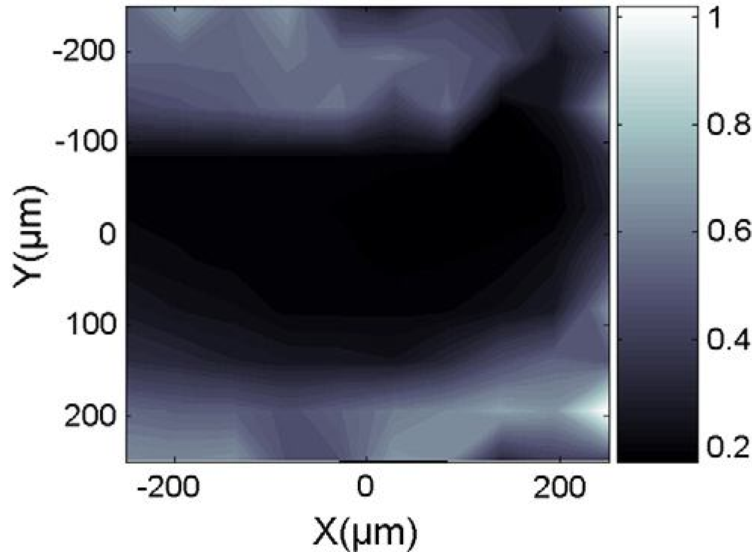

Figure 7: The Raman 2D band mapping of the strain (in percents) of graphene grown on 4H-SiC (0001). The lowest strain is in the centre of the flake while tensions arise near the edges.

The high quality of graphene layers elaborated here allows the investigation of strain effects on G band. Indeed, G band show high intensity in the central area of the main flake, where no second order Raman mode of SiC substrate coexisted with. To see these effects on the G band, we have studied its variation using the same mapping position of 2D band as discussed above. We observe a G band splitting that depends highly on the mapping position. We keep the same line scan used for the 2D band: we present the set of Raman spectra taken along y axes from the position y = -194 µm to the position y= 194 µm for an arbitrary chosen coordinate x=-27 µm of the main flake studied here (Figure 8-a). The Raman spectra exhibit a weak split at the centre as observed in A_3, A_4, A_5 and A_6. This effect became more pronounced at the edge of the flake as appears in A_1, A_2, A_7, A_8. We have used the theoretical model developed previously to investigate G band strain variation (equation 2). The Raman mapping with this band shows a big blue area of this island at the centre identical to the one obtained with the use of the 2D band for the main graphene flake (Figure 8-b). The strain range and the Raman intensity variation obtained for the G band differ to the strain data obtained with 2D band. This dissimilarity is assigned to the limit of our model, which is still good enough to describe our results qualitatively. Note that the 2D band spectrum is more sensitive for a strain variation.

However, the G band investigation still represents a good scale for the strain effect determination. The Raman mapping on the graphene surface demonstrate a broad width at the island boundary. We have fitted the G band using two Lorentzian curves: G^+ and G^-. The bands, G^+ and G^-, correspond respectively to perpendicular E_{2g}^{+} and parallel E_{2g}^{-} modes splited due to the applied strain [15]. We present in Fig. 5-c the intensity mapping of G- (blue colour) and G+ (magenta colour) bands. The obtained results demonstrate similar behaviour to that obtained in theoretical study. The central island zone is dominated with G+ band which is identical to G band without any splitting. The presence of the two bands G^+ and G^- illustrate the presence of biaxial strain in the central area of the flake and uniaxial strain. This could be related to the mechanical properties that change at the edge. The Raman spectra in the main island area keep the same behaviour signature of the presence of biaxial strain in the central island zone of the main flake. The G- band at the edge of the central island zone became more pronounced and verifies the calculated value (see, A_1, A_2, and A_8). This revealed the creation of the uniaxial compressive strain, where the sp_2 bonds became shorter to the direction of the applied strain. This is in contrary to perpendicular bonds that are not too much affected. This illustrates the good agreement between the two studied Raman mappings. On other hands, it helps to specify the value of the strain for epitaxial growth and confirms the above results.

Consequently, our results showed a strain relaxation in the centre of the large graphene flake forming the macro-island. However, at the edge a strong contribution of the substrate effect on the mechanical properties of the graphene exist.

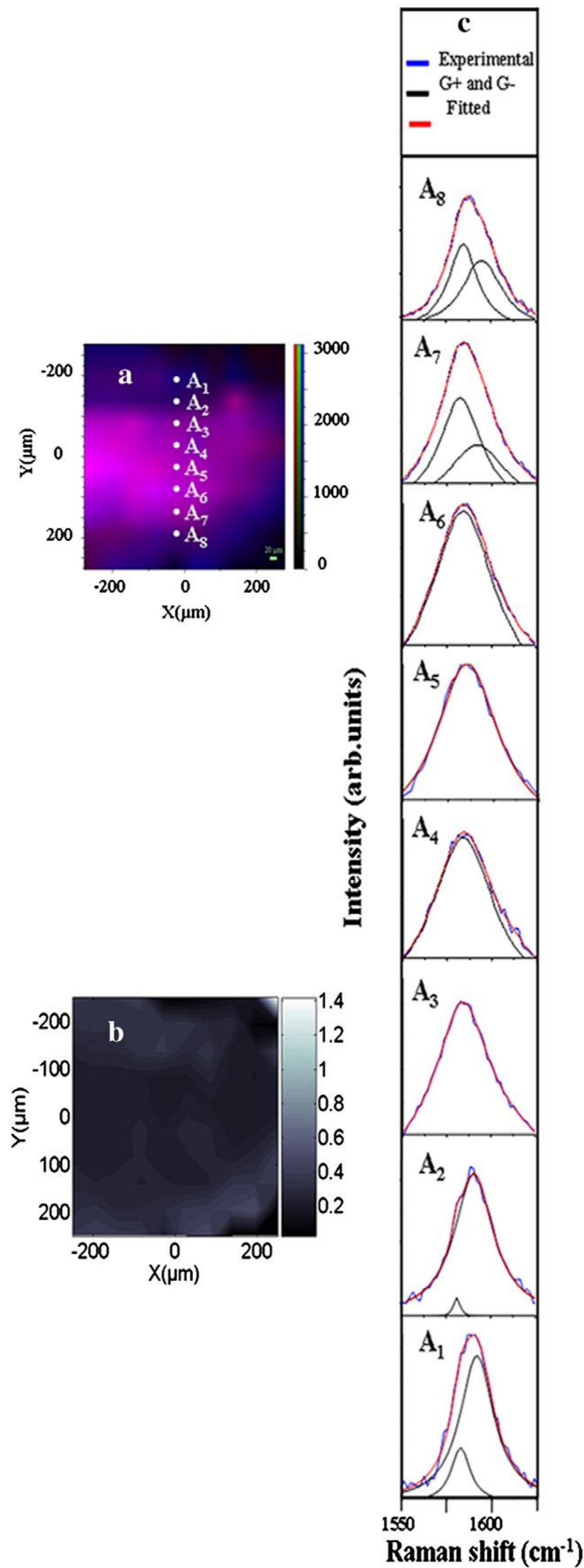

Figure 8: a-The mapping of Raman spectrumof the G band (precisely speaking, the intensity of the G band has been put in a correspondence to the points on the surface of the graphene flake) - for darker spot the band shift is larger, b- G band strain mapping, in percent, on graphene grown on 4H-SiC (0001) substrate - for darker spot the strain is smaller, and c- the mapping intensity and Raman spectra of G+ and G− bands measured at the following points

(A1, A2, A3, A4, A5, A6, A7 and A8, along the y-direction at some fixed coordinate x, see, panel a).

IV- Electrical properties

1- Surface morphology: epitaxial graphene nano-domes and macro- bubbles:

❖ AFM measurements

We investigated the sample surface of our epitaxial graphene grown on 4H-SiC ($000\bar{1}$) substrate using optical microscopy. Three surface morphologies denoted GA_1, GA_2 and GA_3 have been distinguished (Figure 9- a, b and c). The associated optical images show different morphologically (Figure 9).

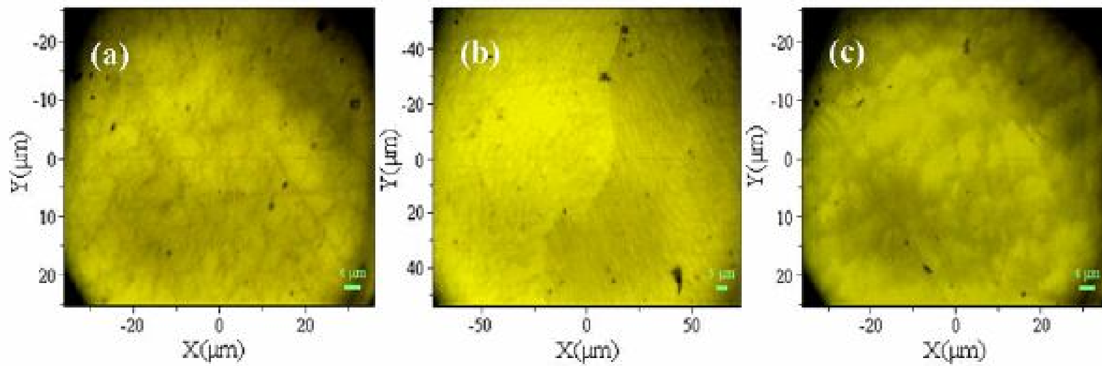

Figure 9: Image obtained using an optical microscope in the different graphene areas 'GA': a- GA_1 (100 x), b- GA_2 (50x) and c- GA_3 (100x).

Figure 10 shows the AFM topography for the considered graphene areas in contact mode. Here, GA_3 show different behavior comparing to GA_1 and GA_2. Indeed, the atomic curved terraces of GA_1 present 500 nm wide and a homogeneous height of 10 nm between the adjacent terraces. Nevertheless, no equidistant steps could be distinguished (Figure 10-a). GA_2 presents terraces of different orientation to GA_1. Here, smaller regular terraces of 250 nm wide and 10 nm height between adjacent terraces arranged with equidistant step were located (Figure 10b). The uniform step height found here illustrates an identical stacking sequence of Si-C bilayer [27, 28]. The equidistant step structures are associated to the repulsive step interaction through the minimisation process of the total surface energy. On the other hand, the asymmetrical step kinetics mechanism results the various stepped morphology as located in GA_2. However, the terrace height in GA_1 and GA_2 is larger than the usually expect for graphene layer, i.e. about 5nm. Commonly, the height of the graphene terraces is *ca.* half to few unit cells of 4H-SiC substrate, i.e. 0.5 to 2nm [29]. The found terraces attain a maximum

height for face terminated C [30, 31]. Nonetheless, we noted the appearance of nanometre size structures even at low resolution for both studied areas. AFM measurement in GA_3 shows different behaviour. The result obtained here differs to the discussed measurements [31 - 32] (Figure 10-c). Here, the sample surface shows large uniformly distributed terraces, of about 500 - 600 nm wide (Figure 10-c). We located a 5 nm height between adjacent terraces as well as equidistant steps. Unusual circles appear in the stepped morphology extending over a few terraces. These circles could not be attributed to the simple roughness of the surface commonly observed for epitaxial graphene grown on 4H-SiC substrate [29, 33, 34]. It could not be defects due to their large size and location. On other hands, they can not originate from the AFM cantilever or scanning artefacts due to their presence across multiple scans at different length scales. The AFM lateral topographical resolution is not able to adequately describe the origin of the surface morphology associated with the new graphene structure observed.

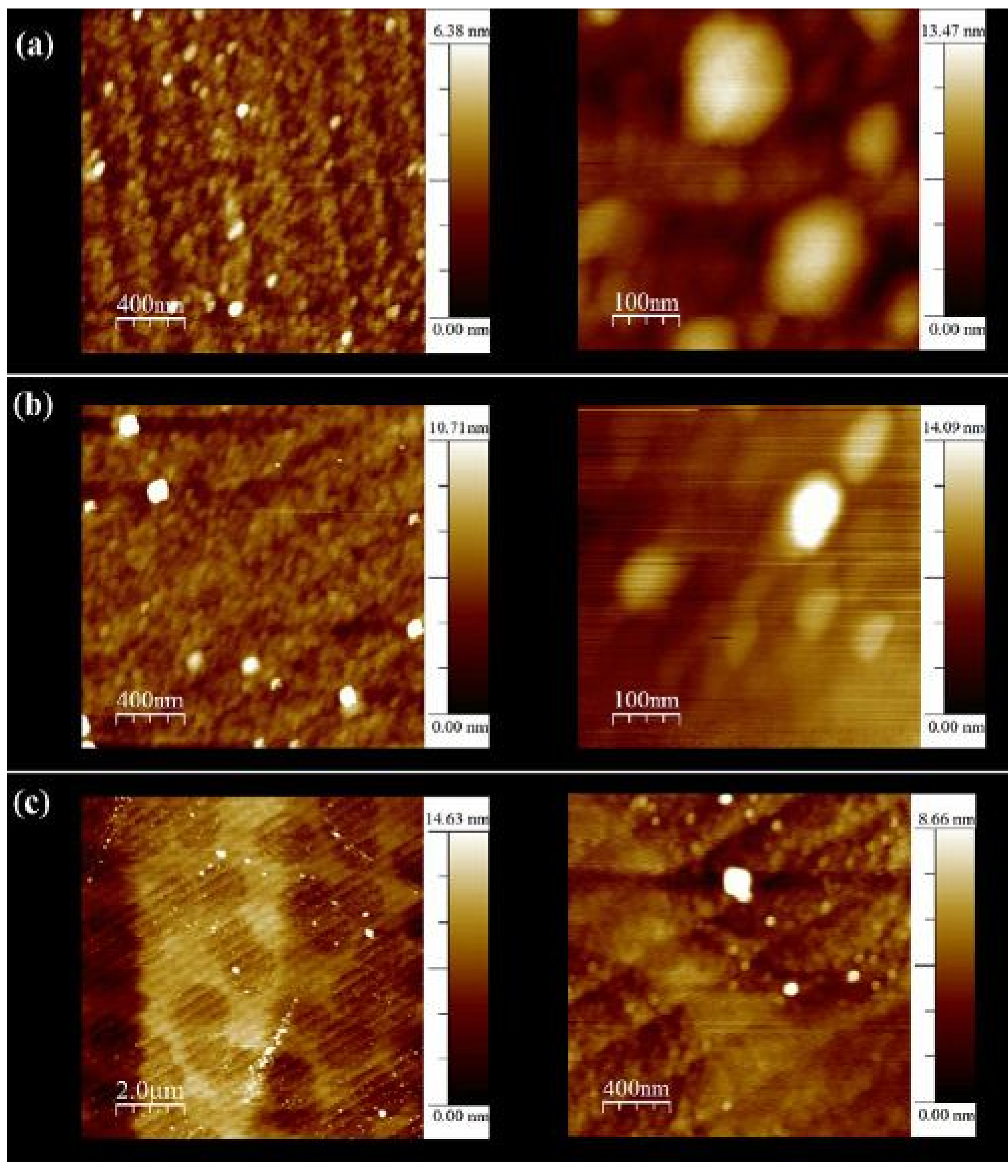

Figure 10: Atomic force microscopy (AFM) images obtained in the investigated graphene areas 'GA' with different scales. a- GA_1, b- GA_2 and c- GA_3.

- **UFM measurements:**

We investigated the nano - mechanical of the sample surface using UFM. UFM measurements characterise local nano - mechanical stiffness. Brighter areas in UFM images correspond to mechanically stiffer areas whereas darker areas have weaker mechanical stiffness. Nevertheless, the absence of UFM signal highlights a zero mechanical contact to the substrate. The dark regions located here correspond to the discussed epitaxial graphene structures (EGS) that could be identified like domes and/or bubbles, respectively, in $GA_{(i=1,2)}$ and GA_3. The darker contrast demonstrates the lower rigidity of these EGS. Here, the various contrast, widths and heights are associated to the domes and bubbles (Figure 11). However, domes and bubbles illustrate a backbone oriented almost parallel to the surface, while their roof takes different forms, i.e. circular and elliptical. We found different size of these graphene structures. EGS of nanometre size (≈150-200nm) are assigned to "domes", whereas those of several micrometers size (≈2µm) correspond to "bubbles". We measure within 5 - 12 nm height in both $GA_{1,2}$ and GA_3. However, UFM of a few domes demonstrates good mechanical stiffness in the centre signature of a supported nature i.e not completely freestanding (Figure 11-a). This type of domes presents a similar high in the centre of the dome as outside it. Indeed, they could be considered as domes with supported centre with a decoupled 'skirt' around the perimeter (Figure 12- a). This indicates higher form in the centre (12 nm) and stiff, corresponding to Si droplets / pillars contamination below the graphene layer. On other hands, the found bubble areas have lower stiffness than the surrounding material. We found large circular regions with [0.5 - 1nm] lower than the surrounding stiffer material (Figure 10-c and 11-c). Thus, we have localised new EGS.

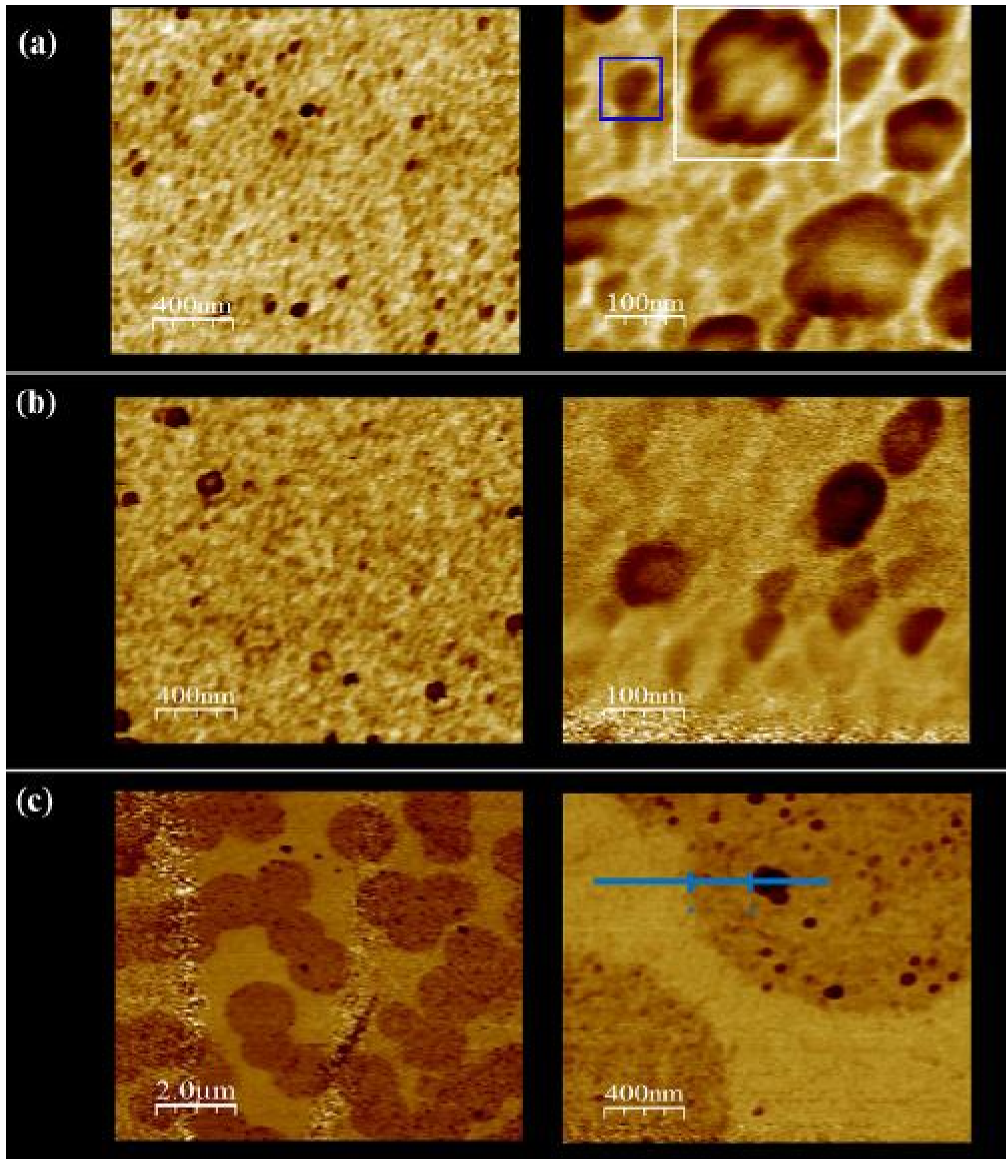

Figure 11: Ultrasonic force microscopy (UFM) images obtained in the studied graphene areas 'GA' with different scales. a- GA_1. b- GA_2 and c- GA_3.

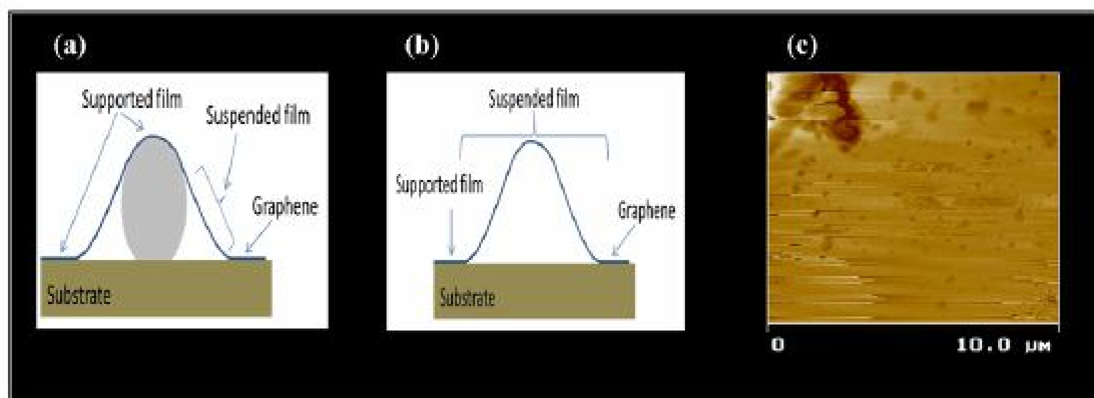

Figure 12: a- Image of epitaxial graphene structures (EGS) having a supported centre with a decoupled 'skirt' around the perimeter, as discussed in the text. b- Image of epitaxial

graphene structures (EGS) completely delaminated or 'freestanding'. c- UFM images taken in GA_2, proving the presence of the step bunching of the 4HSiC (000-1) substrate.

V- EGS properties

1- Raman mapping Localisation of EGS

The optical properties of the EGS identified with UFM were ininvestigated with local intensity mapping of D and 2D bands and the intensity ratio I_G/I_{2D} respectively in GA_1, GA_2 and GA_3 areas (Figure 13 (a, b, c and e)). Due to the similarity between GA_1 and GA_2, we limited our study to GA_1 area. Raman measurements were carried out in periodic locations using 0.5 µm horizontal and vertical step sizes across the flake. Furthermore, we used an auto focusing adjustment for better analysis. We presented the associated Raman spectra (Figure 13). Two different behaviours have been distinguished in the studied areas. Firstly, Raman mapping intensity of the 2D band in GA_1 shows small flakes of lower intensity surrounded by brighter areas of different shapes which from the UFM study we identify as nano-domes. However, due to their nanometre size which exceeds the limit of our beam scale Raman mapping is incapable of precisely determining individual dome boundaries (Figure 13). Secondly, it should be noted that the 2D Raman mapping in the GA_3 area shows remarkable circular structures of high intensity and different radius separated with darker homogenous terraces (Figure 13). These structures look similar to bubbles identified independently using UFM measurements. The mapping intensity ratio of I_G/I_{2D} obtained in GA_1 and GA_3 areas showed similar behavior to the 2D band, where graphene domes and bubbles have been distinguished. These structures also exhibit a low intensity ratio of I_G/I_{2D} revealing low graphene layer number. Thus, the analysis of optical and Raman mapping data confirms the UFM identified epitaxial graphene structures. Raman mapping give a visual identification of the graphene terraces allowing identification of the graphene layer interaction with the substrate and bubbles structure on these terraces. We limited our study to epitaxial graphene bubbles.

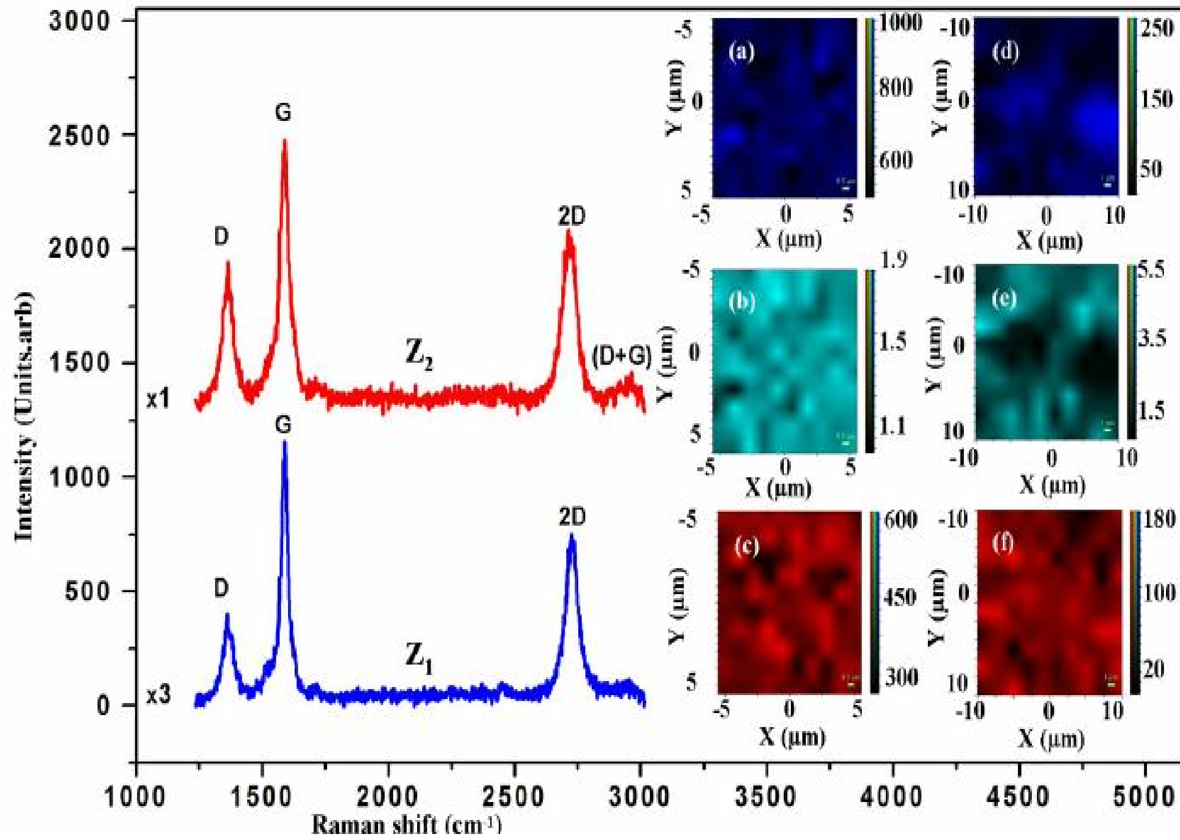

Figure 13: Raman spectra, Z_1 and Z_2, of graphene layers taken in GA_2 and GA_3. Inset: - a, d Mapping Raman Intensity (MRI) of the 2D band, - b, e MRI of the ratio of the G to 2D bands, i.e. IG=I2D. - c, e MRI of the D band obtained in GA2 and GA3 respectively.

We illustrated the sample surface using the local intensity mapping and spectral position of the graphene Raman active modes associated to the D, 2D bands and the I_G/I_{2D}, I_{2D}/I_G ratios (Figure 14 (a, b, c and d)). The Raman spectra inside the bubble display similar behavior to suspended graphene, i.e. isolated from the substrate. The located bubbles showed different micrometric sizes. We chose a typical bubble, of 5 x 4 μm^2 whose size is in good correlation with our high resolution beam focusing scale limit. The Raman spectra show high intensity at the centre for both G and 2D band. The layer number **n** of the epitaxial graphene bubble has been determined using the full width at half maximum (FWHM) of the 2D band correlated with the intensity ratio of the G and 2D bands (I_G/I_{2D}). We have determined the FWHM of the 2D band across the bubble which is of order of 38 - 63 cm^{-1} signature of single layer graphene [35] (Figure 14-e). This verified the obtained intensity ratio (I_G/I_{2D}) results. Indeed, a ratio less than 0.5 corresponds to single layer graphene, for the range 0.5-1 bi-layer and higher than 1.8 it indicated graphene multilayer ($n > 5$); as reported in Ref [36, 37, 38]. Here, we found an intensity ratio of the G and 2D bands (I_G/I_{2D}) is about 0.7 in the area

surrounding the centre of the bubble centre. This ratio increases to 1.5 in the centre and on the edges of the bubble (Figure 14-a). Thus, the correlation between the two methods shows a signature of single layer of graphene. We noted a low intensity ratio (I_G/I_{2D}) in the area surrounding the centre of the bubble. It reaches high intensity in the centre and the bubble edges. Indeed, the low intensity ratio (I_G/I_{2D}) could be assigned to the high doping effect [39]. This is a possible explanation for the variation observed in the behavior of the intensity ratio (I_G/I_{2D}) relative to the 2D band FWHM located in some sample areas. This excludes possible changes of mechanical properties. However, other factors could be attributed to the high value of (I_G/I_{2D}) noted in different areas on the bubble surface. Indeed, at the bubble edges such behavior could be associated with the weak contribution of the substrate. Consequently, we have determined the graphene layer, numbers "n", to single layer of graphene [36, 37]. On other hands, the origin of the dispersion or broadening of the 2D band and the intensity ratio, I_G/I_{2D}, is ascribed to the doping effect. Here, the strain is very small across the bubble and therefore, it could be neglected.

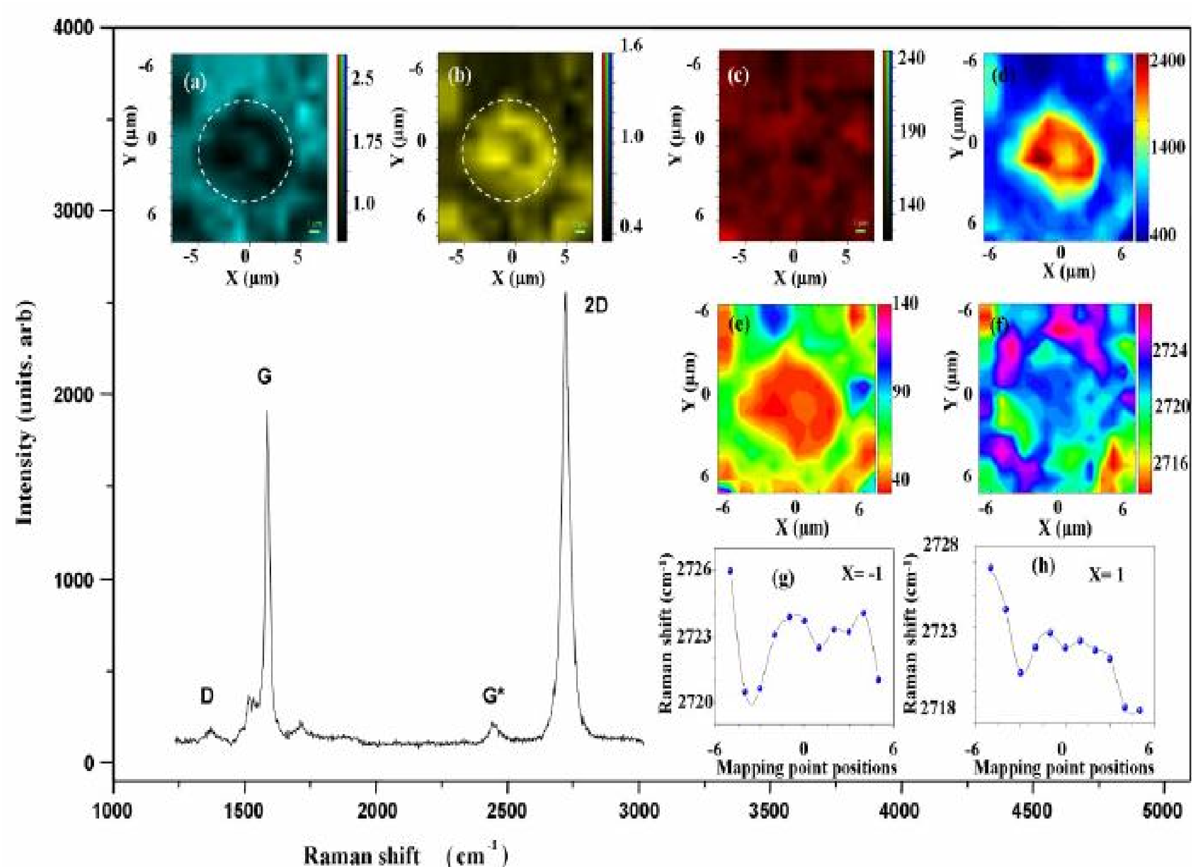

Figure 14: Raman spectrum on the bubble and Raman mapping intensity of: a- the ratios I_{2D}=I_G and b- I_G=I_{2D}; c- the D band; d- the 2D band; e- FWHM of the 2D band; f- Raman shift of the 2D band; - g, (h) Raman shift variation in X =1 and X =-1, respectively, along the Y axes .Y [5, -5] across the bubble.

2- Capacitor effect on epitaxial graphene bubble

The carrier charge density and mobility could be determined using Hall effect measurements. Nevertheless, this method supplies only the transport characteristics of materials. We have studied the charge redistribution between graphene layer, naturally n-type doped, and the substrate, using the Raman mode variation. This intrinsic doping influence nears the surface area of the substrate. Thus, a new charge density distribution is located on the surface and in the volume near the surface. Here, graphene bubble and the charged area of the substrate form a charged system. This behaves as plate capacitor associated with an effective total capacitance, C [40, 41]. Indeed, Graphene properties depend highly on the substrate type. The intrinsic charge impurities of the substrate act as a gate voltage and provide a local doping [39]. Here, a charge transfer from the graphene to the substrate arises. Consequently, epitaxial graphene layer is naturally n-doped. This results in strong Coulomb forces and a transverse electrical field in the substrate-graphene system similarly to plate capacitor. Consequently, the new charge redistributions between graphene and the substrate modify the optical properties, dielectric constants as well as the Raman spectra [39]. We localised an amended behavior of both the Raman spectra of the graphene and the substrate. Raman spectra analysis of epitaxial graphene bubbles describes the strong Coulomb coupling of the graphene layer with the substrate and the associated charge redistribution. Due to the advance of our grown epitaxial graphene bubble, we found a possible determination of the field variation inside the bubble due to a doping effect where new charge redistribution emerges. We demonstrate a possible field creation due to doping effect not only due to strain effect. In fact, Ref [42] reported a field determination of Pt bubbles arising under a giant strain effect. This giant strain produced under low temperature due to the difference in the thermal expansion of Pt and graphene. This varies to our case where our epitaxial graphene bubbles raised during the growth process at high temperatures where all practically strain effects are relaxed. This reveals the advancement of our epitaxial graphene bubbles.

3- Charge distribution in epitaxial graphene bubbles

We determined the charge distribution between the substrate and the graphene layer using Geim group method. They illustrated the dependence between the charge density of the graphene and the intensity ratio of the 2D and G bands (I_{2D}/I_G), reported in Fig.1 Ref. [39]. Using the association and our mapping of the intensity ratio of 2D and G bands (I_{2D}/I_G) across the sample surface, we have defined the charge density distribution in the graphene layer. We

have observed a homogenous charge density distribution going from the centre to the edges of the bubble. The ratio I_{2D}/I_G reaches a high value in the roof and in the foundation of the bubble. Furthermore, the intensity ratio (I_{2D}/I_G) varies from 0.5 to 1.5 and its change from a point to point taken on different homogeneous areas representing different local carrier density (Figure 15-a) [39]. We have determined the corresponding charge density in each of these areas (Figure 15-b). Our measurements show evidently a strong electron doping of the epitaxial graphene layer [39]. The determined electron concentration in the graphene bubble reveals a large variation indicating inhomogeneous substrate behaviour. Thus, it occurs a phonons - plasmons coupling in the graphene-substrate interface related charged capacitor. Thus, we have found the electron density distribution in the graphene layer. Due to the charge neutrality, a thin layer of SiC substrate is highly charged with opposite charge to the bubble graphene layer. Here, the graphene layer charged negatively due to the electron doping, while a positive charge in the SiC substrate emerge. Consequently, the total charge of the system is zero and the neutrality condition is established. Therefore, the graphene bubble and the substrate form a highly active "capacitor" system. This capacitor acts as a resonance cavity for plasmons excitations as well as acting as a mirror limiting and screening the penetration of the electromagnetic radiation from outside to the uncharged volume of the SiC substrate. We will not determine the accurate number of the Si-C bilayer involved in the capacitance system. The charged capacitor forms a mirror or a filter for such radiation. We used a 488 nm line of an Ar-ion laser as exciting probe. However, Raman spectroscopy is not a surface probe. Thus, we were able to characterise the charge distribution in an area of the substrate a few µms thick. We have used the high resolution confocal arrangement of the Raman spectrometer. This leads to probing of a typical depth of 1 to 2 µm after that the penetration of the majority of incident radiation will be stopped. We expect that a small fraction of this radiation will penetrate deeper than 1-2 µm, however, their contribution to the Raman signal will be very small in a comparison with the Raman scattering arising from the graphene - substrate charged system of which the bubble is made of.

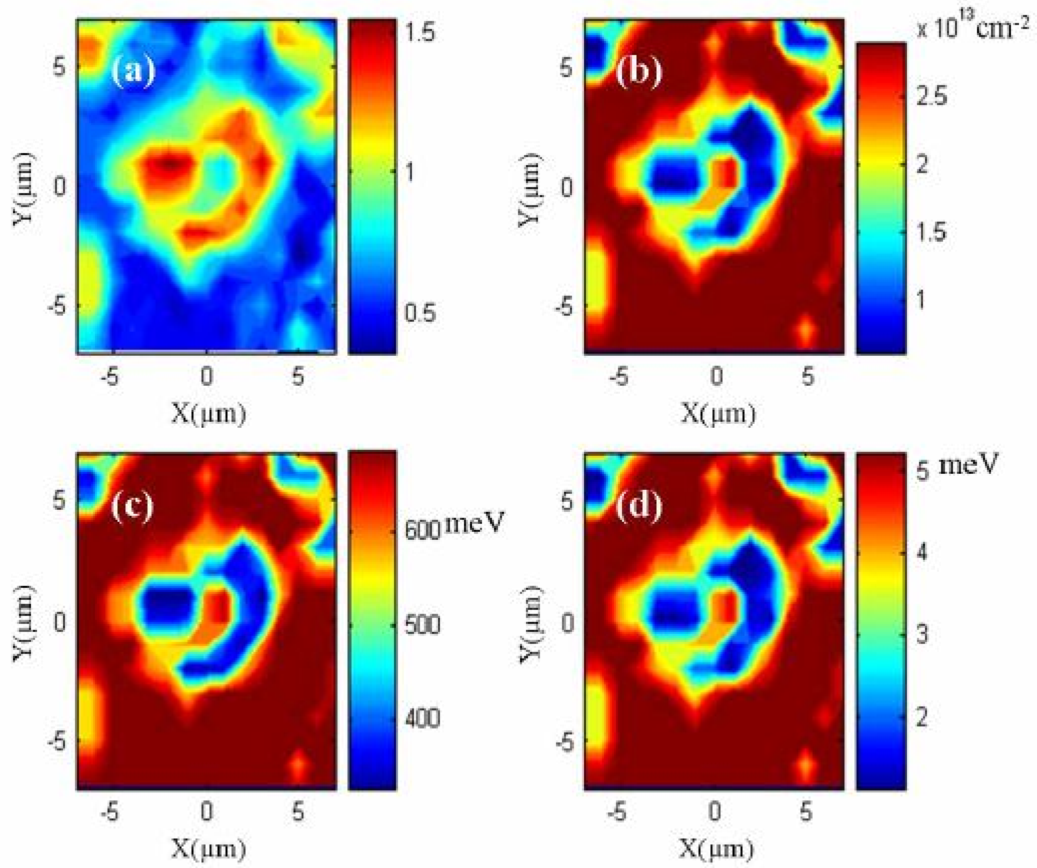

Figure 15: a- Raman mapping of the intensity ratio $I_{2D}=I_G$, b- Electron density distribution mapping. c- Mapping of the Fermi energy variation across the bubble. D- Electric field distribution mapping.

4- Quantum capacitance

We found n-doping effect from electrons coming to the graphene bubble to the 4H-SiC substrate. This results a new electron distribution appears near the graphene-substrate interface inducing intrinsic capacitance. Figure 15-a characterizes the charge distribution across the bubble and the surrounded areas. The substrate defects and the existing charged impurities create additional electrostatic potential contributing to get the observed charge redistribution. Their electrostatic potential acts as a local gate voltage, which changes the charge (electron or hole) density in graphene locally confining electrons or holes approximately. Here, the impurities distribution and the charge redistribution between the graphene and substrate induce charged puddles consisting of holes or electrons. Such puddles have been observed in graphene on SiO_2 substrate [43, 44]. The charge impurities of the substrate are measured as a dominant factor for the puddle's formation. The similar puddles of elongated shape may also be naturally created in epitaxial graphene on SiC due to a terrace step in SiC layer [45, 46]. The atomic terrace on the substrate behaves as gate voltage applied to

graphene forming a trapping potential for electrons or holes. This could be attributed to capacitor effect. Indeed, total capacitance in epitaxial graphene system is given by the following equation [47]:

$$\frac{1}{C} = \frac{1}{C_Q} + \frac{1}{C_{eq}} \qquad (1)$$

Where, C_Q is the quantum capacitance of the graphene layer and C_{eq} is the classical electrostatic plate capacitance formed between the graphene layer and the substrate. The total capacitance for epitaxial graphene corresponds to the summation of three capacitances acting in series composed of the graphene layer, the buffer layers and the doped layer of the 4H-SiC substrate respectively. Thus, the total capacitance could be written as:

$$\frac{1}{C} = \frac{1}{C_Q} + \frac{1}{C_{eq_{BL}}} + \frac{1}{C_{eq_{\mathrm{DL}(4H-SiC)}}} \qquad (2)$$

Where, $C_{eq_{BL}}$ and $C_{eq_{\mathrm{DL}(4H-SiC)}}$ are the electrostatic capacitance of the buffer layer and the doped charged layer of 4H-SiC respectively.

We are studying graphene on carbon terminated face. Therefore, no buffer layer could exist. The electrostatic capacitance is related with the doped layer of 4H-SiC. This could be considered as conventional parallel plate capacitance composed of two plate electrodes. The first electrode is made of graphene layer whereas the second electrode is made of a doped layer of 4H-SiC [48]. The contribution of the SiC bulk layers involved in the capacitance systems is of the order of the quantum capacitance or less. Nevertheless, its value does not depend on the charging effects. Consequently, we will limit our study to the quantum capacitance having the strongest dependence on the charging. Quantum capacitance C_Q is an important property of graphene. It related the capacitor of the graphene layer to accommodate the charge carriers. This type of capacitance differs to the conventional parallel plate capacitance. Indeed, to identify the quantum capacitance we must investigate the dependence of electron density on chemical potential, μ. The density of states (DoS) in two-dimensional graphene on the Fermi energy is related to the value of the Fermi energy E_F given by [49]:

$$D(E_F) = \frac{2|E_F|}{\pi\hbar^2 V_F^2} \qquad (3)$$

There Planck constant is $\hbar$ = 6.58× 10^{-16} eV.s and Fermi velocity in graphene equals V_F $=10^6$m.s^{-1}. The quantum capacitance is written:

$$C_Q = Ae^2 \frac{dn}{dE_F} = \frac{2Ae^2|E_F|}{\hbar^2 \pi V_F^2} \qquad (4)$$

Where, A is the surface area of the capacitor electrodes [50] and at very low temperatures the electron density n is associated with the Fermi energy:

$$n = \int_0^{E_F} D(E)\,dE = \frac{g\ E_F^2}{4\pi\hbar^2 V_F^2} \quad (5)$$

g is the degeneracy factor which takes into account the double spins and the valleys degeneracy of the Dirac spectrum of the graphene (i.e. g = 4). For zero applied electric field, the chemical potential μ and DOS is low. At low temperatures, the dependence of the chemical potential (i.e. the Fermi energy E_F) upon the electron density n is written:

$$\mu = E_F = \hbar V_F \sqrt{\frac{n\pi}{2}} \quad (6)$$

Thus, the quantum capacitance is relative to the chemical potential μ, which is at zero temperature is equal to the Fermi energy $\mu = E_F$ (equation (6)). It is also proportional to the degeneracy of the system that is associated to spin (up/down) degrees of freedom and the valley degeneracy associated with K and K' points of the Brillouin Zone [48]. Here, the density of states on Fermi energy depends on the electron density n. This property is different to the conventional 2D systems where the density of states is usually constant. Therefore, the contributions of the quantum capacitance can be readily noticeable on top of a constant electrostatic capacitance when measurements of the differential capacitance subjected to different gate voltage will be performed. This effect approved several recent observations of graphene quantum compressibility due to the strong spatial averaging [51].

Indeed, we have investigated quantum capacitance using the properties obtained with the intensity ratio of 2D and G band noted I_{2D}/I_G. Figure 15-a illustrated the mapping of the intensity ratio I_{2D}/I_G distribution, the intensity ratio changes from 0.5 to 1.5. We found a low intensity ratio in the roof and in the foundation area of the bubble. Using the method discussed above of the Ref 19, the electron concentration as well as the position of the Fermi energy level has been investigated using I_{2D}/I_G ratio. Figure 9 b characterizes the electron density distribution across the bubble and the surrounded area. We located an electron concentration variation between 0.75 10^{13} to 3 10^{13} cm^{-2} (Figure 15-b). We found a high electron concentration at the roof and in the foundation of the bubble. The Fermi energy varies from 350 to 700 meV (Figure 15-c). The determined values for the Fermi energy are larger than the temperature at which our measurements have been made. Therefore, the presence of the low temperature dependence of the Fermi energy on the charge carriers is well

verified. Accordingly, the Fermi energy keeps comparable behaviour as the electron density. Therefore; we have determined a capacitance range variation per unit area (C_Q/A) in the range 0.034 to 0.068 F m^{-2}. The obtained quantum capacitance illustrates the shift of the Fermi energy above the Dirac point. The quantum capacitance C_Q is small when the density is very small-hence in this case it is the dominant contribution to the total capacitance. This is the so-called graphene quantum capacitance effect [52].

VI- Conclusion

During this chapter, we revealed a possible way to localise epitaxial graphene. Here, the changes of optical contrast as well as the variation of the surface roughness are the main indexes. Indeed, we have investigated both cases and identified using various technique the amended graphene property, i.e either mechanical or electrical property.

References

[1] A. Ben Gouider Trabelsi , A. Ouerghi , O.E. Kusmartseva , F.V. Kusmartsev , M. Oueslati, Thin Solid Films journal. 539, 377–383 (2013).

[2] Nakashina .S, Harima .H, Raman investigation of SiC polytypes, Phys. stat. sol (a), 162 - p 39 – 64, (1997).

[3] Gary L Harris, Properties of silicon carbide, the institution of Electrical Engineers, London, UK (1995).

[4] Burton JC, Sun L, Long FH, Feng ZC, Ferguson IT, Phys. Rev. B. 59(11), 7282–7284 (1999).

[5] Temple PA, Hathaway CE, Phys. Rev. B. 7(8), 3685-92 (1973).

[6] L.M.Malard, M.A.Pimenta, G. Dresselhaus, M.S. Dresselhaus, L.M. Malard et al, Raman spectroscopy in graphene, Physics Reports 473, 51-87 (2009).

[7] Raman spectroscopy of graphite, Stephanie Reich and Christian Thomsen, Phil. Trans. R. Soc. Lond. A 362, 2271–2288 (2004).

[8] Optical Characterization of Graphene and Highly Oriented Pyrolytic GraphiteR. Kostić, M. Mirić, T. Radić, M. Radović, R. Gajić and Z.V. Popović, Vol. 116 (2009).

[9] F. Tuinstra, J.L. Koenig, J. Compos. Mater. 4, 492 (1970).

[10] François Varchon, Propriétés électroniques et structurales du graphene sur carbure de silicium, universite Joseph Fourier (2008).

[11] Calizoa I, Ghosha S, Baob W, Miaob F, Laub C N and Balandin A, Raman nanometrology of graphene: Temperature and substrate effects, Sol. State Comm. 149 1132-1135 (2009).

[12] Symmetry and Condensed Matter Physics A Computational Approach M. El-Batanouny Boston University F. Wooten University of California, Davis, Cambridge University Press (2008).

[13] Solid-State Spectroscopy, Hans Kuzmany, Springer-Verlag Berlin Heidelberg, (2009).

[14] Group-theory analysis of electrons and phonons in N-layer graphene systems, L. M. Malard, M. H. D. Guimarães, D. L. Mafra, M. S. C. Mazzoni, and A. Jorio, physical review B 79, 125426 (2009).

[15] Ferrari A C and Robertson J, Interpretation of Raman spectra of disordered and amorphous carbon,Phys. Rev. B 61, 14095 (2000).

[16] L.G. Cancado, Pimenta M A, Neves B R A, Dantas M S S and Jorio A, Influence of the Atomic Structure on the Raman Spectra of Graphite Edges, Phys. Rev. Lett. 93, 247401 (2004).

[17] Irene Calizo, Igor Bejenari, Muhammad Rahman, Guanxiong Liu, and Alexander A. Balandinc, Ultraviolet Raman microscopy of single and multilayer graphene, Journal of Applied Physics 106, 043509 (2009).

[18] Dong Su Lee, Christian Riedl, Benjamin Krauss, Klaus von Klitzing, Ulrich Starke, and Jurgen H. Smet, Raman spectra of epitaxial graphene on SiC and of epitaxial graphene transferred to SiO_2, Nano letters 8 (12), 4320-4325 (2008).

[19] J. Yan, Y. B. Zhang, P. Kim, and A. Pinczuk, Electric field effect tuning of electron – phonon coupling in graphene ,Phys. Rev. Lett. 98, 166802 (2007).

[20] C. Casiraghi, A. Hartschuh, H. Qian, S. Piscanec, C. Georgi, A. Fasoli, K. S. Novoselov, D. M. Basko, and A. C. Ferrari, Raman Spectroscopy of Graphene Edges, Nano Lett., Vol. 9, No. 4, (2009).

[21] Nikhil Sharma, Doogie Oh, Harry Abernathy, Meilin Liu, Phillip N. First, Thomas M. Orlando, Signatures of epitaxial graphene grown on Si-terminated 6H-SiC (0 0 0 1), Surface Science 604 84–88 (2010).

[22] Pimenta M A, Dresselhaus G, Dresselhaus M S, Cançado L G, Jorioa A and Saitoe R, Studying disorder in graphite-based systems by Raman spectroscopy, Phys. Chem. Chem. Phys. 9 1276–1291.

[23] T. Georgiou, L. Britnell, P. Blake, R. Gorbachev, A. Gholinia, A.K. Geim, C. Casiraghi, K.S. Novoselov, Graphene bubbles with controllable curvature, Appl. Phys. Lett. 99, 093103 (2011).

[24] Jakob Zabel, Rahul R. Nair, Anna Ott, Thanasis Georgiou, Andre K. Geim, Kostya S. Novoselov, Cinzia Casiraghi, Raman Spectroscopy of Graphene and Bilayer under Biaxial Strain: Bubbles and Balloons, Nano Lett. 12, 617 (2012).

[25] Ferralis N, Maboudian R and Carraro C, Evidence of structural strain in epitaxial graphene layers on 6H-SiC (0001),Phys. Rev. Lett. 101, 156801 (2008)

[26] K.V. Emtsev, A. Bostwick, K.Horn, J. Jobst, G.L. Kellogg, L. Ley, J.L. McChesney, T. Ohta, S.A.Reshanov, J.Röhrl, E. Rotenberg,A.K. Schmid, D.Waldmann, H.B.Weber, T. Seyller, Quantum Hall Effect and Carrier Scattering in Quasi-Free-Standing Monolayer Graphene, Nat. Mater. 8 (2009).

[27] Schwoebe R L and Shipsey E J, J. Appl. Phys. 37 3682, 1966 .

[28] Li X 2008 Epitaxial graphene films on SiC: growth, characterization, and devices PhD Thesis Georgia Institute of Technology

[29] Hallin C, Owman F, Martensson P, Ellison A, Konstantinov A, Kordina O and Janzen E, J. Cryst. Growth 181 241–53, 1997.

[30] Ramachandran V, Brady M F, Smith A R, Feenstra R M and Greve D W, J. Electron. Mater. 27 308–12, 1998.

[31] Losurdo M, Bruno G, Brown A and Kim T H, Appl. Phys. Lett. 84 4011–3, 2004.

[32] Heindl J, Dorsch W, Strunk P P, Muller S G, Eckstein R, Hofmann D and Winnacker A , Phys. Rev. Lett. 80 740–1, 1998.

[33] Sander D, Wulfhekel W, Hanbucken M, Nitsche S, Palmari J P, Dulot F, d'Avitaya F A and Leycuras A, Appl. Phys. Lett. 81 3570–2, 2002.

[34] Georgiou T, Britnell L, Blake P, Gorbachev R, Gholinia A, Geim A K, Casiraghi C and Novoselov K S, Appl. Phys. Lett. 99 093103, 2011.

[35] Ni Z H, Chen W, Fan X F, Kuo J L, Yu T, Wee A T S and Shen Z X, Phys. Rev. B 77 115416, 2008.

[36] Ismach A, Druzgalski C, Penwell S, Schwartzberg A, Zheng M, Javey A, Bokor J and Zhang Y, Nano Lett. 10 1542–8, 2010.

[37] Hass J, Varchon F, Mill´anOtoya J E, Sprinkle M, Sharma N, de Heer W A, Berger C, First P N, Magaud L and Conrad E H, Phys. Rev. Lett. 100 125504, 2008.

[38] Faugeras C, Nerri`ere A, Potemski M, Mahmood A, Dujardin E, Berger C and de Heer W A, Appl. Phys. Lett. 92 011914, 2008.

[39] Das A et al, Nature Nanotechnol. 3 210, 2008.

[40] O'Hare A, Kusmartsev F V and Kugel K I, Nano Lett. 12 1045–52, 2012.

[41] Yan J, Zhang Y B, Kim P and Pinczuk A, Phys. Rev. Lett. 98 166802, 2007.

[42] Hartman J D, Roskowski A M, Reitmeier Z J, Tracy K M, Davis R F and Nemanich R J, J. Vac. Sci. Technol. A 21 394–400, 2003.

[43] Calizo I, Bejenari I, Rahman M, Liu G and Balandinc A A, J. Appl. Phys. 106 043509, 2009.

[44] Lee D Su, Riedl C, Krauss B, von Klitzing K, Starke U and Smet J H, Nano Lett. 8 4320–5, 2008.

[45] Drummond N D, Z´olyomi V and Fal'ko V I, Phys. Rev. B 85 075423, 2012.

[46] Lin YM, Keith J A, Ott J, Dimitrakopoulos C, Farrmer D B, Wu Y Q, Grill A and Avouris P, IEEE Electron Device Lett. 32 1343, 2011.

[47] Yu C, Li J, Liu Q B, Dun S B, He Z Z, Zhang X W, Cai S J and Feng Z H, Appl. Phys. Lett. 102 013107, 2013.

[48] Castro Neto A H, Guinea F, Peres N M R, Geim A K and Novoselov K S, Rev. Mod. Phys. 81 109, 2009

[49] Lee JK et al, Nano Lett. 13 3494–500, 2013.

[50] Yung K C, Wu W M, Pierpoint M P and Kusmartsev F V, Contemp. Phys. 54 233–51, 2013

[51] Hewett T H and Kusmartsev F V, Cent. Eur. J. Phys. 10 602, 2012.

[52] Martin J, Akerman N, Ulbricht G, Lohmann T, Smet J, Klitzing K and Yacoby A , Phys. 5 669–74, 2009.

Chapter 4:

Phonons plasmons coupling

I- Introduction

In this chapter, we will focus on the basic notions of solid-state plasma physics and explain their role in the creation of a capacitance effect at the graphene-substrate interface. In a first part, we recall the characteristics of solid-state plasma such as: the plasma frequency and the dielectric constant. Then, we study the inelastic scattering of light by plasmas in semiconductors. Finally, the case of the inelastic scattering of light by plasmas for graphene will be detailed. Indeed, in this part we will be interested in the phonon-plasmons coupling which occurs at the interface graphene - substrate: silicon carbide "SiC". We have located a capacitance effect at the interface resulting from an intrinsic doping effect of the graphene layer by the substrate.

II- Plasma in the solid state: characteristic and property

Solid state plasmas assigned to free carriers charge that interact with each other in the solid by Coulomb forces. Often, these plasmas can be located in gases, liquids, metals and semiconductors. For semiconductors, plasmas represent a combination of electrons and semiconductor holes that are virtually free, characterized by a free path of negligible size with respect to the sample. This explains the more dilute character of plasmas in semiconductors compared to those of metals. Therefore, the electron density plays no role in determining the properties of the crystal structure. Thus, the study of solid state plasmas in semiconductors is related to intrinsic characteristics, not to the structure of the crystal. In addition, solid state plasmas of semiconductors differ from those of metals by its parameters of interest such as: plasma frequency, cyclotron frequency, Fermi energy, optical phonons and the forbidden band. Indeed, the complementarity of these parameters creates a wide variety of phenomena in the plasmas. In the following, we will describe some characteristics of solid state plasma parameters in semiconductors.

1- Low coupling

The plasma describes the states of the material defined by charged particles ensuring the interactions of electrical and / or magnetic origin. Any external perturbation affecting the plasma is related to the mobility of its constituents; As well as to the strength of the connections between its constituents, or between the constituents and the network, as in the case of a semiconductor. For a particle system behaving similar to plasma, its particle

agitation energy must dominate the binding energy of the particles to the lattice. However, any charged particle system does not meet this criterion. Indeed, in order to have a solid state plasma behavior, the charged particles must verify the following condition:

$$\frac{E_{pot}}{E_c} \langle\langle \quad 1 \qquad (1)$$

Where, E_{pot} corresponds to the potential energy of the interaction between particles and E_c is the kinetic energy. This condition corresponds to the criterion of weak coupling. This weak coupling is verified for the two limiting cases: plasma diluted at high temperature and cold plasmas. Plasmas diluted at high temperature are characterized by particles of thermal energy greater than the average energy of the Coulomb interaction between particles, such as those of gas. However, cold plasma refers to heavily doped metal and semiconductor plasmas. These plasmas are very dense and degenerate. Here, the criterion of the weak coupling is made by comparing the energy of Coulomb with respect to the energy of Fermi E_F of the gas of electrons. In a medium of dielectric constant ε_0, the mean energy of the Coulomb interactions is given by $\frac{e^2}{4\pi\varepsilon_0 l_0}$, such that ℓ_0 is the average distance between the carriers. This energy is expressed as a function of the density $l_0 = n_0^{-\frac{1}{3}}$. Thus, the criterion of weak coupling is written:

$$\frac{E_{pot}}{E_c} \approx \frac{e^2 n_0^{\frac{1}{3}}}{4\pi\varepsilon_0 E_F} \qquad (2)$$

In the case of semiconductors, the Fermi energy of the free electron gas is:

$$E_F = \frac{\hbar^2 k_F^2}{2m^*} \qquad (3)$$

With k_F is the Fermi wave vector given by ($k_F = (3\pi^2 n_0)^{1/3}$) and m* the effective mass.

Equation 2 is rewritten in terms of Bohr radius effective ($a_B^* = \frac{4\pi\varepsilon_0 \hbar^2}{m^* e^2}$), and a length denoted by r_0 defined as the radius of the elementary volume per electron with $\frac{4\pi}{3} r_0^3 = \frac{1}{n_0}$.

We can write the criterion of weak coupling in the following form [1]

$$r_s = \frac{r_0}{a_B^*} \langle\langle 1 \qquad (4)$$

Where, r_s characterizes the strength of the electron - electron interaction in a solid - state plasma of a semiconductor.

1-2 Screening Length

The Coulomb potential of a positive charge (ion) plunged into an electron gas as seen by another positive charge of dense media, such as metals and semiconductors, decreases by an amount of $\exp(-k_D r)/r$. The electron gas accumulates around the positive charge as well as the shielding. This effect is known as electrostatic screening. The shielding behavior of an electron gas as a function of the wave vector is described by its static dielectric function ε (0, k). For a non-degenerate plasma or also called Maxwellian where ($E_F \ll K_B T$), the screening parameter k_D is defined by the following:

$$K_D^2 \equiv \frac{1}{\lambda_D^2} = \frac{4\pi n_0 e^2}{4\pi\varepsilon_0 k_B T} \quad (5)$$

λ_D is the Debye screening length and T is the temperature of the electron gas. λ_D is defined by the penetration distance of the external electrostatic field before it is compensated by the fields induced in the plasma. For a degenerate plasma ($E_F \gg k_B T$), this length is called Fermi - Thomas λFT. It can be determined by replacing the thermal energy λ_{FT} by the energy of Fermi (EF) [2] in equation 5.

This length of screening remains an important parameter for the characterization of plasma. Indeed, it separates the response of the plasma into two different regimes: the first which corresponds to the regime of collective oscillations (obtained for $\lambda > \lambda_D$). The second characterizes the behavior of the individual oscillations (obtained for $\lambda < \lambda D$).

1-2 Plasma Frequency

The plasma frequency ω_p is one of the characteristics of plasmas in the solid state. It separates the high and low frequency domains, within which the plasma acquires different behaviours. Electromagnetic fields with low frequencies with respect to ω_p will be screened. However, the higher frequency fields will be transmitted. For doped semiconductors, there are two plasma modes: a high frequency mode affecting all valence electrons and another low-frequency mode, or only the conduction electrons participate. Each mode is characterized by a plasma frequency which depends on the dielectric constant of the oscillating medium considered: electron gas or positive "background" of the ions. For a semiconductor with simple "SiC" conduction semiconductor, n-type doped, the plasma frequency of the low frequency mode can be obtained in the framework of the Drude model by [3]:

$$\omega_p = \left(\frac{n_c e^2}{\varepsilon 0 m^*}\right)^{1/2} \qquad (6)$$

Where m * is the effective mass of the carriers, n_c is the electron conduction density and ε_0 is the static dielectric constant of the undoped semiconductor. This formula is valid outside the reststrahlen region.

For SiC, the values of the dielectric constants at 300 K are equal to ε_0 = 8.854187 and ε_∞= 6.78 (high - frequency dielectric constant) **[4, 5]**, giving energies of the order of a few tens of meV i.e. $\hbar\omega_p$ <EG, where EG is the forbidden energy gap. It is recalled that EG is of the order of 2.39, 3.023, 3.263 eV respectively for 3C-SiC, 6H-SiC, 4H-SiC at 300 K. Following the quantification of the plasma wave of plasmons characterized by a quantum of $\hbar\omega_p$ appear. Phonon - plasmon coupling remains among the important phenomena in polar semiconductors (SiC). In the remainder of this chapter, we will detail the Raman scattering of plasmons.

1-3 Dielectric Function

The dielectric function of an electron gas ε is defined with the aid of the electric field E and the polarization P in the framework of the classical electrostatic which is expressed as follows:

$$D = \varepsilon_0 E + P = \varepsilon_r \varepsilon_0 E \qquad (7)$$

With D is the displacement vector of the electric field. The dielectric function of an electron gas generally depends on the frequency and on the wave vector ε (ω, k). This function is fundamental for the characterization of plasma: on the one hand ε (ω, 0) provides a description of the plasmons. Whereas, ε (0, k) provides a description of the electrostatic screening of electron - electron interactions and electron - grid interactions in the crystal. The dielectric response of an electron gas ε (ω, 0) to the long wavelength limit (λ >> λD) can be calculated from the equation of motion of a free electron subject to electric field:

$$m\frac{d^2x}{dt^2} = -eE \qquad (8)$$

In the case where x and E are harmonically dependent on time, then equation (8) can be written as:

$$-m\omega^2 x = -eE \text{ and } x = \frac{eE}{mw^2} \qquad (9)$$

The polarization P is defined as the dipole moment per unit volume, it is written:

$$P = -n_0 ex = -\frac{n_0 e^2 E}{mw^2} \qquad (10)$$

The dielectric function at frequency ω is defined from equation (7):

$$\varepsilon(\omega) \equiv 1 + \frac{P}{\varepsilon_0 E} = 1 - \frac{n_0 e^2}{\varepsilon_0 m w^2} \qquad (11)$$

The positive charges have a dielectric constant denoted ε_∞ for the high frequencies. Thus, equation 11 becomes:

$$\varepsilon(\omega) = \varepsilon_\infty - \frac{n_0 e^2}{\varepsilon_0 m \omega^2} = \varepsilon_\infty \left(1 - \frac{\omega_p^2}{\omega^2}\right) \qquad (12)$$

Where ω p is the frequency of the low frequency mode defined previously by Equation 6.

Equations 10 and 11 are obtained by admitting totally free plasma electrons. This is not true for solid-state plasmas, especially in semiconductors. Plasma electrons in the solid state are affected by the potential stress of the crystal lattice containing defects, impurities and phonons. In the following, we will see the application of the formalism of the dielectric function for the determination of the frequencies of the collective propagation modes (plasmons) in polar semiconductors such as the poly 4H-SiC type studied in this connection.

III- Inelastic scattering and plasmons

Since the 1950s, several researchers have focused on the study of plasmons in solids. These studies were based on electron energy loss spectroscopy [6 - 8]. Indeed, it shows a lost of the electrons of an amount equal to an integer multiple of the quantum of energy $\hbar\omega_p$. The high quantity of energy is equal to ten electron volts for the case of simple metals (Al, Ag, Au) [6]. The energies measured by this technique allow the determination of very high frequency plasmons involving all valence electrons. In addition, other collective modes of lower frequencies involving only conduction electrons, they are often observed in doped semiconductors. These waves have characteristic energies of the order of ten meV. But, these energies close to the far infrared are not detectable by the experiments of loss of energy of the electrons. This imposed the use of the Raman scattering study. Indeed, inelastic light scattering remains a powerful tool for the study of low-energy excitations in semiconductors. Thus, the Raman study not only studies the energy spectra obtained by the difference in the

frequencies of the incident and diffused photons ($\Delta\omega = \omega_i - \omega_s$), but also the dispersion of their wave vector defined by the transfer of moment ($\Delta k = k_i - k_s$).

The properties of phonon - plasmon coupled modes in SiC have been reported in several preliminary studies [4, 5]. Figure 1 shows the scattering of electrons or light. The incident beam of wave vector ki and of frequency illuminates plasma which also diffuses a small part of the light in all directions with a wave vector k_s and frequency ω_s . The scattering angle Θ corresponds to the angle at which scattered light of scattering wave vector q = ki − ks is observed.

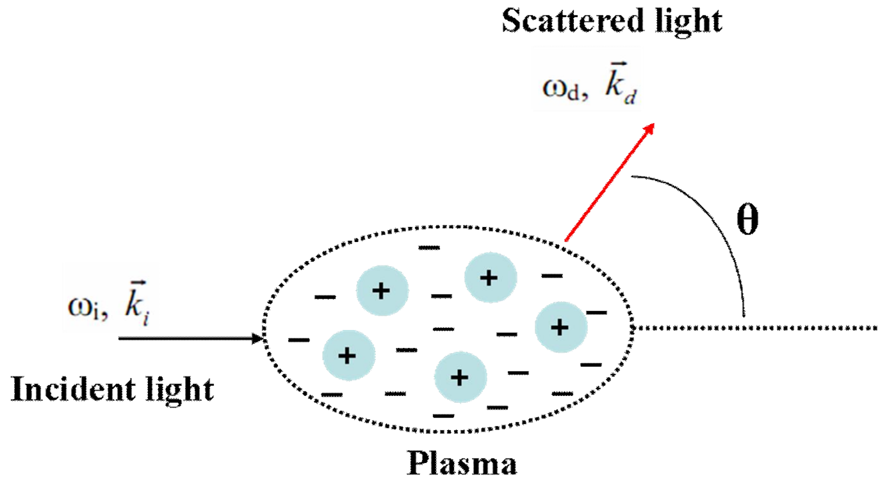

Figure 1: The scattering of electrons or light.

There are two types of electronic excitation: collective excitation and excitation to a particle. For the first excitation, the propagation frequencies are non-zero at q = 0. The second one is characterized by ω = 0 and q = 0. This allows us to determine the excitations to "solid-state plasma" Near the laser in Raman scattering. Figure 2 shows the Raman spectrum of collective excitations (plasmons), where the Stokes (S) and anti-Stokes (AS) lines are distinguished. We will detail in the following the formalism of the dielectric function for a non-degenerate plasma in the long wavelengths k = 0, where the spectrum is dominated by the collective effects (plasmons) and apply it to the phonon-plasmons couplings in the Polar semiconductors such as "SiC".

1- Diffusion of light by electron plasmas in semiconductors

In this part we shall not recall the theory of the inelastic scattering of light by a gas of electrons, where we shall have recourse to N-body physics. But, we will use some known results applied to semiconductors and phonon-plasmons couplings.

1-1 Dynamic structure factor

In this study, we limit ourselves to the case of the plasma of a semiconductor constituted of a single species, whose electrons are in a simple parabolic conduction band with an effective mass tensor m *. The effects of non-parabolicity of the energy bands of electrons are not taken into consideration. The theory of the interaction of the electromagnetic fields incident (i) and diffused with the electrons of the semiconductor allows us to calculate the differential diffusion section, noted $\partial^2\sigma/\partial\Omega\partial\omega$. This diffusion is expressed as a function of the effective mass tensor, the diffusion volume V, the classical electron radius $r_0 = e^2/4\pi\varepsilon_0 mc^2$, the incident frequency ω_i and the scattering frequency ω_s and the dynamic structure factor S (ω, q) such that Frequency of diffusion is previously defined by:

$$\Delta\omega = \omega_i - \omega_s \qquad (13)$$

And the diffusion wave vector

$$q = k_i - k_s \qquad (14)$$

In this case, we will admit a large dynamic structure factor S. This is because the factor is related to the dielectric response of the plasma which contains information about the intensity and shape of the Raman scattering spectra. The dynamic structure factor is given by the fluctuation - dissipation theorem [1, 9]:

$$S(\omega,q) = \frac{\hbar q^2 \varepsilon_0 \varepsilon_\infty^2}{\pi e^2 V}(1 - e^{-\hbar\omega/k_B T})^{-1}\,\mathrm{Im}\left\{-\frac{1}{\varepsilon(\omega,q)}\right\} \qquad (15)$$

ε_0 is the dielectric constant of the vacuum, ε_∞ is the dielectric constant of the grating and $\varepsilon(\omega,q)$ the total longitudinal dielectric constant of the semiconductor. The term $(1-e^{-\hbar\omega/k_B T})$ is the function of the Bose - Einstein statistic. The energies of the characteristic modes of the light scattering spectra are then related to the maximums of the function $\mathrm{Im}\left\{-\frac{1}{\varepsilon(\omega,q)}\right\}$ in equation (15).

1-2 Phonon-plasmon coupling

The phonon - plasmon coupled modes are longitudinal modes associated with the macroscopic electric field. The latter coupled the phonons with the collective excitations of the free carriers. Each coupled mode has its own dispersion relation ω (q) based on the determination of the dielectric function ε (ω, q). However, the dielectric function of the longitudinal modes is deduced from the Maxwell equations for $k \times E = 0$ [2]:

$$\varepsilon(\omega, q) = 0 \qquad (16)$$

The dielectric function is written as a summation of a real part and an imaginary part. For an imaginary part $\mathrm{Im}\left\{-\frac{1}{\varepsilon(\omega,q)}\right\}$ negligible with respect to the real part the term of the equation (14) will be maximal this gives:

$$\mathrm{Re}\{\varepsilon(\omega, q)\} = 0 \qquad (17)$$

Equation (16) is necessary for the determination of the frequency of plasmons (collective modes) and coupled modes. For large imaginary parts, the preceding approximation is no longer valid and equation (15) then imposes solutions with values of ω and k complex. These solutions may be imposed by experimental conditions such as Raman scattering. These conditions imply a real k [10].

In the following, we apply the above results to the polar and degenerate semiconductors such as the cases of doped SiC. In the approximation of the random phase for a q = 0, which is generally the case in most Raman scattering experiments, the total longitudinal dielectric function is written [11]:

$$\begin{aligned}\varepsilon(\omega, q) &= \varepsilon_\infty + \chi_L(\omega) + \chi(0,\omega) \\ &= \varepsilon_\infty + \varepsilon_\infty \frac{\omega_{LO}^2 - \omega_{TO}^2}{\omega_{TO}^2 - \omega^2} - \varepsilon_\infty \frac{\omega_P^2}{\omega^2} \qquad (18)\end{aligned}$$

Where the second and last term respectively correspond to the contribution of the polar network χL (ω) and the free carriers χ (0, ω) to the electrical susceptibility. In equation (18), ω (TO) and ω (LO) are the frequencies of the optical transverse (TO) and optical longitudinal (LO) phonons. Whereas ω p is the plasmon frequency defined in (6). Thus, we obtain the equation of phonon-plasmon modes.

$$\omega_\pm^2 = \frac{1}{2}\left\{(\omega_p^2 - \omega_{LO}^2) \pm [(\omega_p^2 + \omega_{LO}^2) - 4\omega_p^2\omega_{LO}^2]^{1/2}\right\} (19)$$

The variation of the coupled modes ω ± as a function of the carrier density were interpreted in terms of the simple Drude model for the susceptibility of free electrons, that is to say without taking into account the dependence of the wave vector q of the plasma frequency. In fact,

small dispersions of collective modes ($\omega \pm (q)$ and ωp (q)) can be observed in a backscattering geometry. In this geometry, the amplitude of the diffusion wave vector depends on the wavelength of the laser excitation. Under these conditions, the susceptibility of free electrons can be calculated from a hydrodynamic approach [9, 10], whose expression is written:

$$\chi(q,\omega) = -\frac{\omega_p^2}{\omega^2 - \frac{3}{5}q^2 v_F^2} \quad (20)$$

This expression is satisfied for $\omega > qV_F$ and $q < k_F$ for the regime where the "Landau damping" is negligible.

IV- Study of the substrate-graphene interface

1- Raman spectroscopy investigation

Raman spectra analysis across the sample surface describe the degree of homogeneity and the number of graphene layers, **n**. Raman mapping was carried out with a 0.5 µm step in Z_1 and Z_2 . During mapping acquisition, laser beam focusing was checked at each point using an auto focusing adjustment. Figure 3 illustrates the local Raman mappings intensity at D band frequency (ω_D), G band frequency (ω_G) and 2D band frequency (ω_{2D}), correspondingly in Z_1 and Z_2. The Raman mapping of D band displayed weak intensity across the sample surface in Z_1 eliminating a possible nitrogen doping, while it slightly increased in Z_2 (Figure 2-a and -b). This is related to the graphite layers interaction. Local Raman mappings intensity ratio of G and 2D band (I_G/I_{2D}) demonstrate similar behaviour (Figure 2 -g and -h). We have determined based on a well-known meethod the graphene layer number consuming (I_G/I_{2D}) in the both studied zones [12, 13]. The Z_1 is covered with a single (n=1) and bilayer graphene (n=2). Nevertheless, small graphite flakes were located. Z_2 is about an 80% covered with graphite and small bilayer (n=2) flakes. The determination of the graphene layer number is discussed below. We have carry out a Raman investigation in two frequency ranges {(I) = [100 - 1000 cm^{-1}]) and (II) = [1000 - 3000 cm^{-1}])}. The range (I) corresponds to the first order Raman modes of the SiC substrate, while the range (II) is attributed to the second order spectral bands of the SiC substrate and both first and second order Raman modes of graphene. Here, we limited our study to the second range of frequencies. Figure 2 shows the typical Raman spectra of various graphene layers located in Z_1 (Z_{1-1}, Z_{1-2} and Z_{1-3}) and Z_2 (Z_{2-1}). Numerous second order Raman mode of 4H-SiC also exist in the frequency range [1479 - 1905 cm^{-1}] [13]. We identified all the graphene peaks D, G, 2D, G* and (D+G) (Figure 2). We have identified the layer number **n** of epitaxial graphene grown on 4H-SiC using the

integrated intensities ratio of the G and 2D bands "I_G/I_{2D}" [14, 15-16]. Indeed, as reported in the literature[14, 15-16], a ratio less than 0.5 corresponds to single layer graphene, 0.5–1 to a bilayer and 1.8 and above to multilayer ($n > 5$). The Raman mapping intensity ratio of G and 2D band "I_G / I_{2D}" in Z_1 and Z_2 are consistent with the layer number order, **n**, given by this well-known method (Figure 3 -g and -h) [14, 15-16]. In our case, we associate the intensity ratio I_G / I_{2D} of 0.45, 0.8 and <1.8 to single, bilayer and graphite respectively, as appears in the related Raman mapping of I_G / I_{2D} in both the investigated areas.

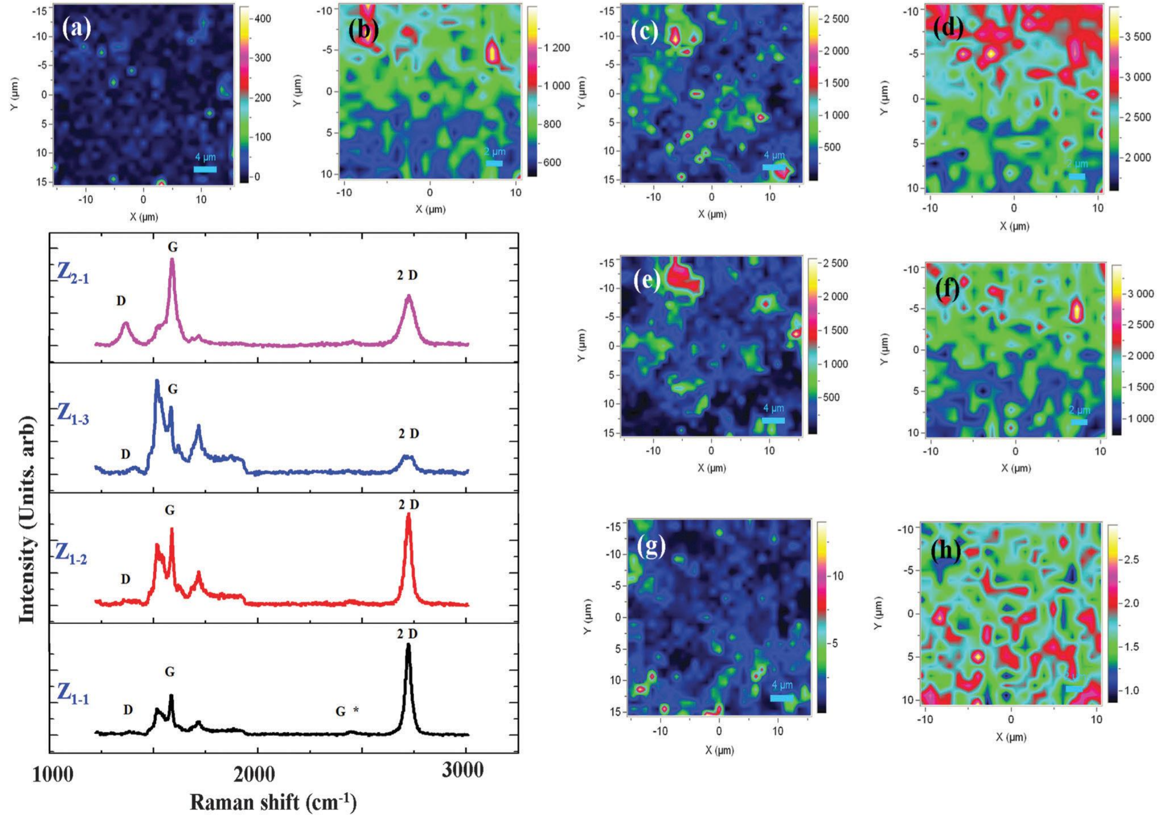

Figure 2: Raman Spectra of: single layer (Z_{1-1}), bilayer (Z_{1-2}) and graphite (Z_{1-3}) obtained in Z1, and (Z_{2-1}) graphite located in Z_2. Raman mapping intensity of: a- and b- D band, c- and d- G band, e- and f- 2D band and g- and h- G on 2D ratio (I_G/I_{2D}) obtained respectively in Z_1 and Z_2.

2- Phonon - Plasmon couplings

We examined the longitudinal optical phonon - plasmon interaction in the 4H-SiC substrate. We illustrate a strong coupling between these two modes. We related the energy shift from point to point on the surface to the carrier density difference in graphene layers studied with other methods [17, 18]. LOPPC modes are bulk substrate properties. This was well documented in n-type SiC, which has been widely investigated [19]. Figure 4 shows Raman spectrum obtained in the frequency range [100 - 1000 cm^{-1}] which corresponds to the major

modes of the 4H-SiC substrate. We clearly distinguish the $E_{2\,(high)}$, E_2, E_1 (TO) and A_1 (LO) observed respectively at 154, 770, 791, 967 cm^{-1} [20 – 22] (Figure 3).

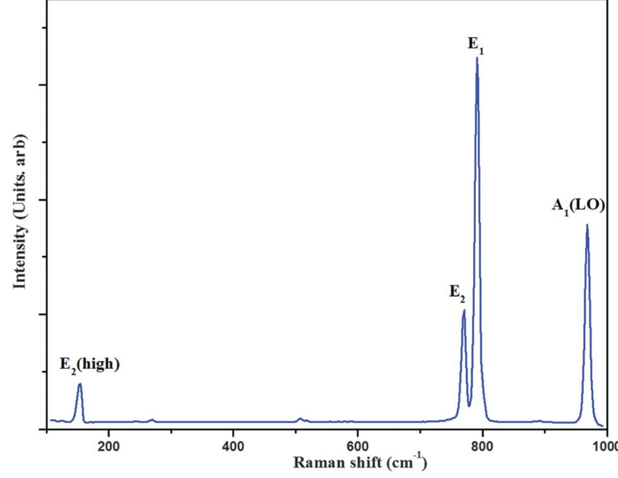

Figure 3: Raman spectrum obtained at the frequency range [1000-3000 cm^{-1}] signature of 4H–SiC (000-1) substrate.

However, we notice a amendement in the A_1 (LO) mode shift position across the sample surface. We have used a 488 nm line of an Ar-ion laser as an exciting probe. Raman spectroscopy is not a surface probe, therefore, we are able to characterise the charge distribution in a whole area of the substrate for few micrometers (µms) thickness. Indeed, we are able to probe to a typical depth of 1 to 2 µm. The small shifts in the Raman lines found across the sample surface are correlated with a local change in residual carrier concentration of the nominally un-doped 4H-SiC substrate located at 962 cm^{-1} [23]. Plasmon waves, induces a charge density fluctuations in the substrate and graphene. They polarize the graphene and excite the LO and TO phonons in the substrate. Both the shift and the line shape of the LOPPC band are investigated using a theoretical model in which the Raman intensity is given by [19, 24]

$$I(\omega)=\frac{d^2S}{d\omega\, d\Omega}\propto A(\omega)\mathrm{Im}\left(-\frac{1}{\varepsilon(\omega,q)}\right), \qquad (1)$$

Where $A(\omega)$ and $\varepsilon(\omega,q)$ are the spectral and dielectric functions, respectively [25]. $A(\omega)$ and $\varepsilon(\omega,q)$ are a function of plasma frequency, ω_p, plasmon damping concentration, γ_p, damping constant of electrons, Γ, high-frequency dielectric constant, ε_∞, Faust-Henry constant, C and phonon frequency, ω_L (ω_T) of the A_1[LO] (E_1 [TO]) 4H-SiC mode. The theoretical curve is obtained using the following fitting parameters: the electron effective mass in SiC is $m^* = 0.29 * m_0$ (m_0 is the free electron mass); the frequency of TO (LO) phonon is ω_T = 774 cm^{-1} (ω_L = 962 cm^{-1}) of a none doped 4H-SiC substrate [27]. We found a blue shift and broadening

of the line width of the LOPPC peak. This may be assigned to the increase of the phonon - plasmon interaction [16]. Indeed, this can't be associated with a heating effect due to the high control of our measurements setup. We reported a typical fitted A_1 (LO) spectra of single layer graphene (Z_{1-1}), bilayer graphene (Z_{1-2}) and (Z_{1-3}) graphite found in Z_1 and also graphite located in Z_2 (Z_{2-1}) (Figure 4).

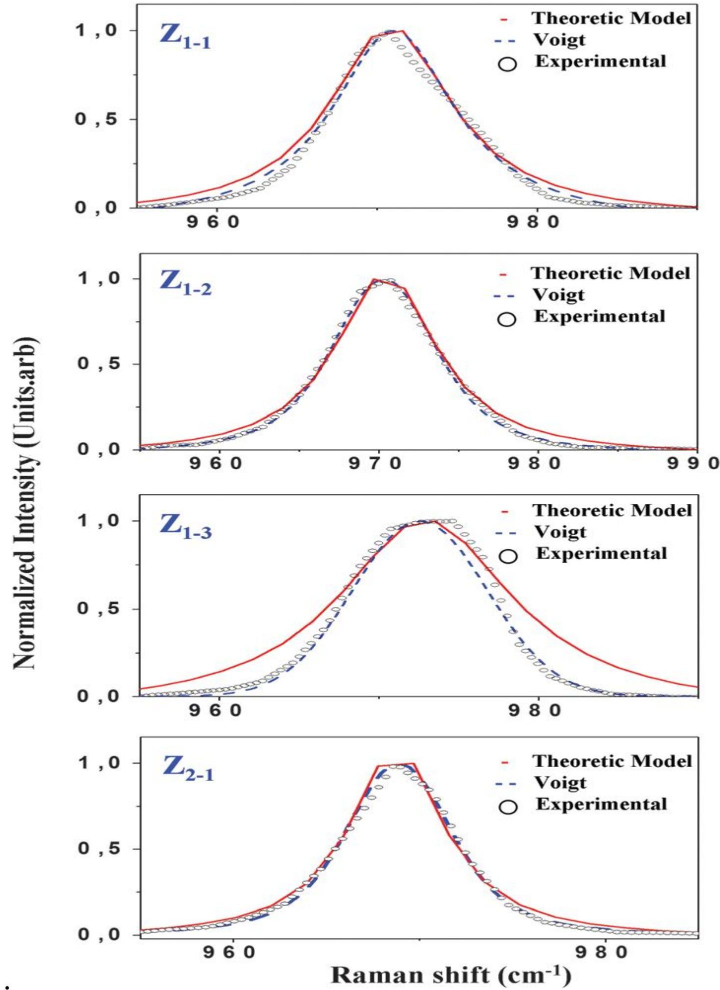

Figure 4: Variation of the line shape of the theoretical (solid line), experimental (points) and Voigt (dashed line) curves of the ''LOPPC'' modes as function of the epitaxial graphene layers for: single layer (Z_{1-1}), bilayer (Z_{1-2}) and graphite (Z_{1-3}) obtained in Z_1, and graphite located in Z2 (Z_{2-1}).

We deduce that A_1 (LO) mode is not fitted properly due to its broadening. This phenomenon is assigned to its high local carrier density as observed in Z_{1-1} and Z_{1-3}. This is dissimilar to weak doping where the A_1 (LO) mode is well fitted (Z_{2-1} and Z_{1-2}). This doesn't affect the value of the frequency ω_p. The theoretical fit generally does not properly adjust the investigated tail of the A_1 (LO) band. A Voigt fit based on a Lorentzian-Gaussian shape curve provides a better fit. This has been used to establish the A_1 (LO) Raman shift position change

across the sample surface respectively in Z_1 and Z_2 (Figure 5 -c and -e). The A_1 (LO) Raman mapping intensity presents a similar behavior to G and 2D band (Figure 5 (a-b) and Figure 2 (c-f)). Here, A_1 (LO) shift changes are sensitive to the local doping. The value of the shift move comparing to the spectral line of the pure 4H-SiC (000$\bar{1}$) substrate i.e. un-doped. The A_1 (LO) discussed is located at 962 cm^{-1}. A high blue shift $\Delta\omega$ is located in Z_1 of 11 cm^{-1} [969 - 973 cm^{-1}] comparing to non-doped substrate (Figure 5-c). On other hand, a maximum shift of 7 cm^{-1} is located in Z_2 [968.4 - 969.4 cm^{-1}] (Figure 5-e). The A_1 (LO) shift varies from 1 to 4 cm^{-1} according to the investigated zones. The high shift in Z_1 is associated with the weak layer number. However, a gradual dissimilarity is observed Z_2 between the Raman mapping intensity and the shift variation of A_1 (LO) in Z_1 (Figure 5 -a and -c). On other hands, we locate a consisting phonons shift variation between substrate and weakly doped graphite layer, as observed in Z_2, (Figure 5 -b and -e). The presence of highly doped graphene layer and the formation of quantum capacitance induce charging or charge redistribution in the system. This charge redistribution creates a high screening of Coulomb forces. This induces a phonon - plasmon coupling as it is observed for high density of excited electron-hole plasma. This was located for the metal graphite in Z_1, where high electrons density does exist and high screening could be noticed. Accordingly, the shift variation of G band of the graphite and the A_1 (LO) of substrate are different (Figure 5 -c and -d). This is also supported by the behavior observed in Z_2 when compared to Z_1 (Figure 5 -e and -f)

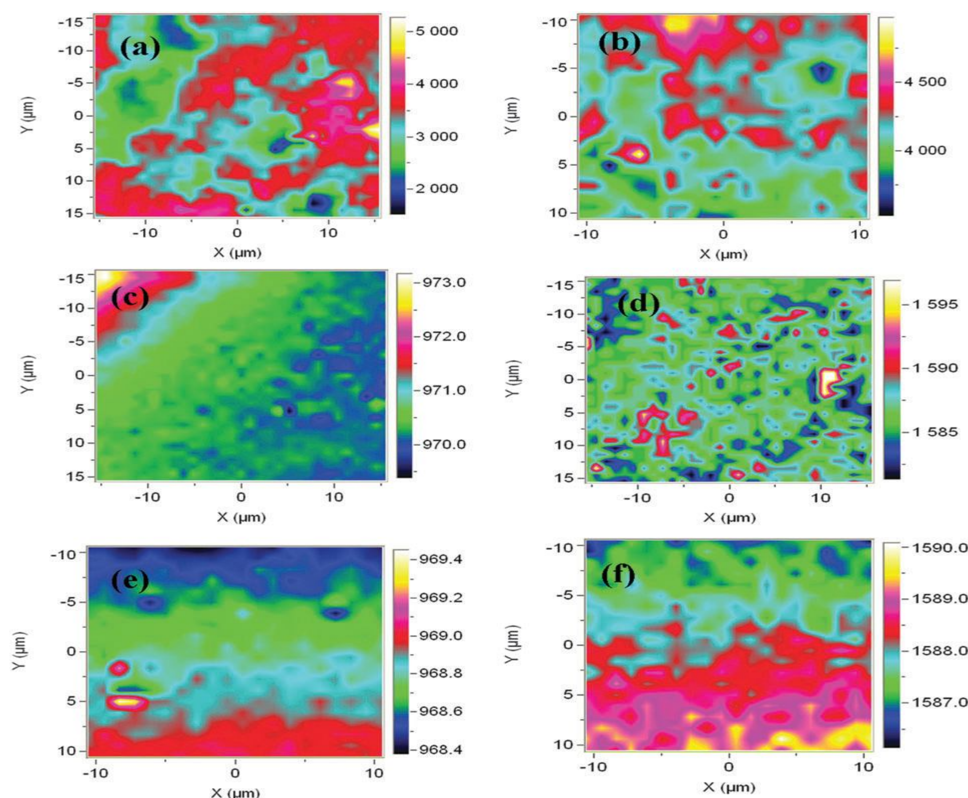

Figure 5: Raman mapping of A_1 (LO): intensity -a in Z1, -b in Z2. Raman mapping of the A_1 (LO) shift variation obtained in -c Z_1 and -e Z_2. Raman mapping of the G band shift variation obtained in -d Z1 and -f Z_2.

We studied a third homogenous area of our sample, Z_3 of 80x80 μm^2 covered with single-, multi-layer graphene and graphite in order to confirm our found (Figure 6). The I_G/I_{2D} ratio indicates a signature of single layer graphene as located in Z_1 (Figure 2). The A_1 (LO) frequency varies between 964 and 967cm^{-1} despite the presence of single layer graphene (Figure 7-f). This shows the sensitivity of our model to the present carrier density. However, a dissimilarity is located between the shift and intensity variations (Figure 6-e and -f). This is regardless of the weak doping existing in this area. Indeed, the A_1 (LO) shift variation is about ≈3 cm^{-1}, similar to Z_1. On other hands, we located dissimilarity between the Raman shift variations of the A_1 (LO) substrate mode and the G mode of the graphene (Figure 6 -f and -g). Such variation is attributed to the large variation of A_1 (LO) frequency position associated the broad fluctuations of the local charge distribution. These fluctuations results a high screening of Coulomb forces between substrate and graphene. Thus, we developed an excellent model to investigate phonon - plasmon coupling for epitaxial graphene. On other hands, we present a high-quality imaging of the epitaxial graphene – SiC interface system.

Here, we become able to estimate the free carrier concentration n to adjust the plasma frequency ω_p in 4H-SiC given by [23]

$$\omega_p^2 = \frac{4\pi ne^2}{\varepsilon_0\varepsilon_\infty m^*} + \frac{3}{5}(qv_F)^2 \qquad \text{(2-a)}$$

The plasmonic excitations in graphene close to the Dirac point for small plasmonic momenta q written [27]

$$\omega_{pgr}^2 = \frac{2n_{gr}e^2}{m}q + \frac{3}{4}(qv_F)^2 \qquad \text{(2-b)}$$

m is the electron effective mass at the bottom of the graphene band, and n_{gr} is the charge carrier density in the graphene layer. An interaction happens between these two branches of plasmonic excitations given in (2-a) and (2-b). This results a weak hybridisation and formation of a polariton excitation spectrum that we will not study here. We limited our study the phonon - plasmon interaction which is relevant for both branches and estimate it using the substrate properties, i. e the LOPPC model as detailed above [27].

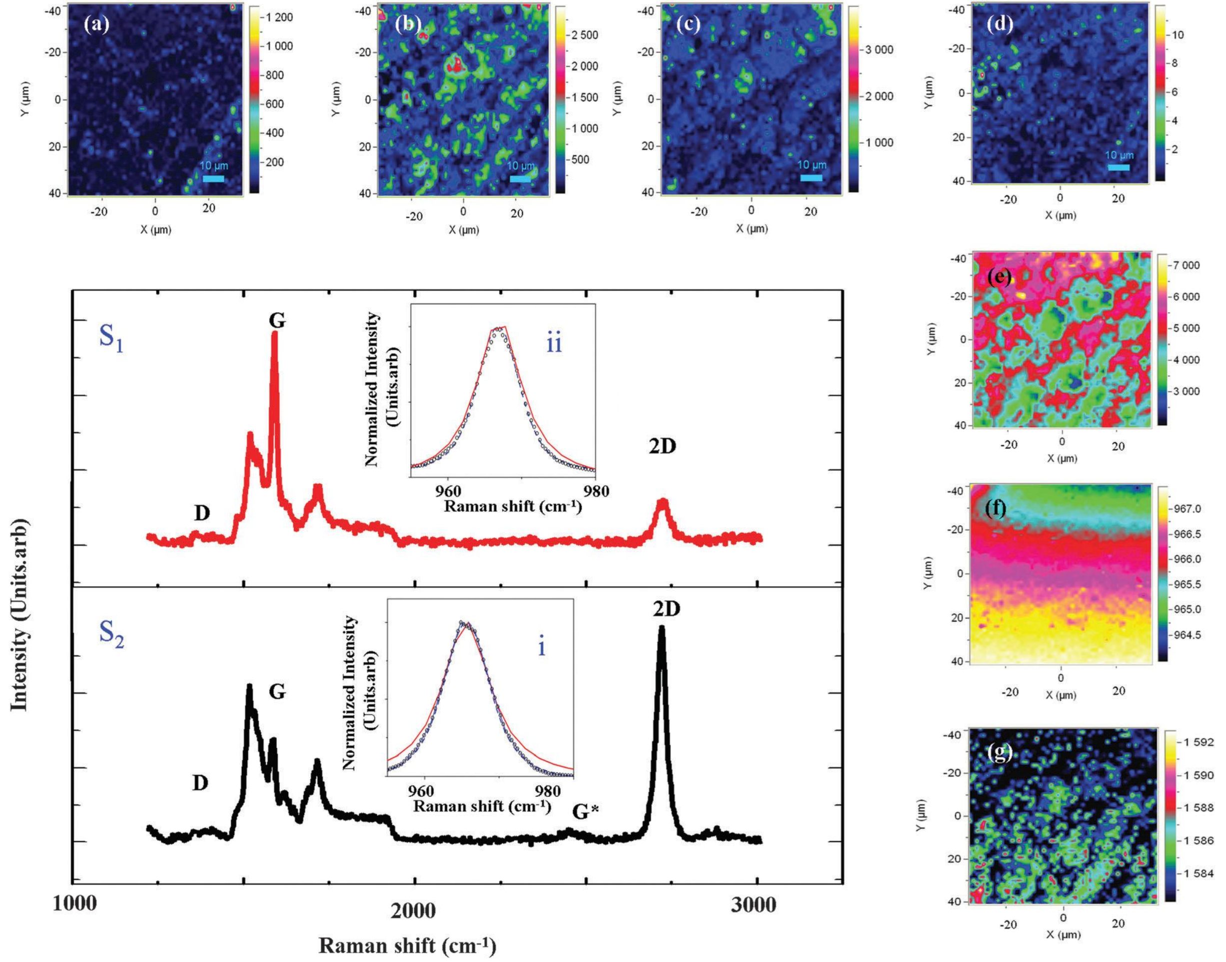

Figure 6: Raman mapping intensity of: -a D band, -b G band, -c 2D band, -d ratio (I_G/I_{2D}), -e A_1 (LO) intensity. The Raman mapping of the shift variation of: -f A_1 (LO) mode, -g G mode. The Raman spectrum of: S_1 – single layer graphene, S_2 – graphite, obtained in Z_3. Insets: The line shape of the theoretical (solid line), experimental (points) and Voigt (dashed line) curves of the ''LOPPC'' modes associated with: (i) single layer and (ii) graphite obtained in Z3.

3. Graphene self-doping

We used an undoped 4H-SiC substrate for graphene growth. On other hands, we limited to the Brillouin zone centre excitations or weak photon excitations with vanishing momentum, q = 0. This approach is limited in order to fit A_1 (LO) bands for high electron concentration in the substrate. This is due to the contribution of the excitations out of the Brillouin zone centre and the non - parabolicity of the bands [24]. Here, the electron concentrations were determined with the adjusted values of the plasma frequency ω_p and the plasmons damping γ_p , of the common substrate for any graphene layer number (see, table 1). We located a density of charge equivalent to $n_{Z1\text{-}1}$= 2.7129 10^{18} cm^{-3}, $n_{Z1\text{-}2}$= 2.5214 10^{18} cm^{-3}, $n_{Z1\text{-}3}$=4.1904 10^{18} cm^{-3} and $n_{Z2\text{-}1}$=1.8857 10^{18} cm^{-3}. However, the initial value on the substrate

without epitaxial graphene layers was $n_{Substrate}$= 3.448 10^{11} cm^{-3}. We located a decrease of the densities of charge with the increasing the graphene layers.

Graphene layers located in Z_1 and Z_2	Plasma frequency (cm^{-1}) ω_p	Plasmons damping (cm^{-1}) γ_p
Single layer Z_{1-1}	199	310
Bilayer Z_{1-2}	185.0	248
Graphite Z_{1-3}	238.5	454
Graphite Z_{2-1}	159.99	129

Table 1: The associated values of fittings parameters of the frequency of plasma oscillations ɣp and the constants of their damping gp obtained in Z_{1-1}, Z_{1-2}, Z_{1-3} and Z_{2-1}.

The original electron density of SiC substrate, $n_{Substrate}$, is very low due to the insulator character of our substrate. We compare the obtained carrier density to previous works of single layer graphene using G band shift variation. We found a shift variation between [1583-1595 cm^{-1}] and [1586 -1590 cm^{-1}], respectively in Z_1 and Z_2. This illustrates a blue Raman shift comparing to the G line position of un-doped monolayer graphene located at 1580 cm^{-1} [28] (Figure 5). In fact, the G band shift increases by increasing the layer number whereas in a conventional case without charge redistribution a red shift must appear [29]. This could be assigned to the association of doping and disorder effect [27, 30]. Previous epitaxial graphene work [17] found an electron density equals $5x10^{12}cm^{-2}$ for a G band shift of 8 cm^{-1}. Here, the G band for typical Raman spectra, as located in Z_1, appears at 1585 cm^{-1}. This shift is associated with $3.0x10^{12}$ cm^{-2}, which confirms our findings [28]. Using our A_1 (LO) model, such a shift indicates an electron density equal to n_{Gr}= $2x10^{12}$ cm^{-2}. Indeed, the charge redistribution in the substrate is very inhomogeneous. It has high density of charge near the graphene layers that decreases by going inside the bulk. The small difference between the two determined electron densities is assigned to the charge inside the bulk. Conceiving of a model capable of determining this charge is a challenge with which epitaxial graphene – substrate system is faced. Accordingly, we found a good an agreement of the charge density obtained with the Raman shift analysis of both A_1 (LO) and G band. Here, we limited our study to single layer graphene of which a typical spectrum was given in Z_1. Due to the electro-neutrality of the system, the total charge accumulated in the graphene-substrate system is equal to zero. Thus, the total charge of the substrate should be equal to the charge in the graphene with an opposite sign. Due to the electron doping of the graphene, it will be charged negatively, whereas the

SiC substrate is charged positively. This condition gives that $n_{Gr} = n_1 L$, where L is the charged layer thickness of the substrate. We locate approximately a thickness L=0.54 µm of the charged surface layer of the substrate. This was found out after the examination of 2857 bi-layers of SiC, knowing that the Si-C bond length in SiC crystal is 1.89A °. Thus, graphene and charged substrate layers form a "capacitor" system that behaves as a resonant cavity for plasmons excitations propagating along the graphene surface. Additionally, it acts as a mirror, limiting and screening the penetration of the electromagnetic radiation to the uncharged volume of the SiC substrate. Here, the given density of charged graphene corresponds to that of the bulk substrate. The surface charge density is determined with the 2D projection from the value n_1. We obtain $n_s \sim (n_1)^{2/3} = 2.x10^{12}\ cm^{-2}$, which is equal to the charge density of the graphene as $n_{Gr} \sim n_s$. This rough estimation gives a close value.

V- Conclusion

We have investigated epitaxial graphene grown on face terminated carbon. Using Raman analysis several graphene characteristics, such as graphene layer numbers and disorder, have been identified. We revealed a possible localisation of the A_1 (LO) phonon– plasmon coupled modes ''LOPPC'' of 4H–SiC. Such a coupling strongly depends on substrate doping. Thus, we define a non-invasive characterisation of the charge density distribution in a graphene– substrate system. This gave a clear description of the epitaxial graphene–substrate interface based on analysis of the phonon– plasmon coupling.

References:

[1] P.M. Platzman and P.A. Wolff "Waves and Interactions in Solid State Plasmas", Academic Press, New-York and London (1973).

[2] C. Kittel "Introduction to Solid State Physics", 7th edition,Wiley & Sons (1996)

[3] P.Y. Yu and M. Cardona "Fundamentals of Semiconductors", third edition, Springer (2001).

[4] Nakashina .S, Harima .H, Raman investigation of SiC polytypes, Phys. stat. sol (a), 162 - p 39 – 64, (1997).

[5] Burton JC, Sun L, Pophristic M, Lukacs SJ, Long FH, Feng ZC et al., Spatial characterization of doped SiC wafers by Raman spectroscopy, Journal of Applied physics 84(11), 6268-6273 (1998).

[6] G. Ruthermann, Discrete energy losses of electrons of medium velocity on passage through thin foils, Ann. Phys. 2, 113 (1948).

[7] D. Pines and D. Bohm, A Collective Description of Electron Interactions.I. Magnetic Interactions, Phys. Rev. 82, 625 (1951).

[8] L. Marton, L.B. Leder and H. Mendlowitz, Advanced in electronic and electron phys, (Ed. by L. Marton) New York, Academic Press, p.183 (1955).

[9] G. Abstreiter, M. cardona and A. Pinczuk, Chap. 2 in Light Scattering in Solids IV. Topics in Physics vol. 54, Ed. M. Cardona and G. güntherodt, Springer-Verlag (1984).

[10] U. Nowak, W. Richter and G. Sachs, LO-Phonon–Plasmon Dispersion in GaAs: Hydrodynamical Theory and Experimental Results, phys. stat. sol. (b) 108, 131 (1981).

[11] A. Das, S. Pisana, B. Chakraborty, S. Piscanec, S. K. Saha, U. V. Waghmare, K. S. Novoselov, H. R. Krishnamurthy, A. K. Geim, A. C. Ferrari & A. K. Sood, Monitoring Dopants by Raman Scattering in an Electrochemically Top-Gated Graphene Transistor, Nature Nanotechnology 3, 210-215 (2008), Nature Nanotechnol. 3, 210 – 215 (2008).

[12] N. Zhan, G. Wang and J. Liu, Appl. Phys. A: Mater. Sci. Process., 105, 341–345, 2011.

[13] C. Li, D. Li, J. Yang, X. Zeng and W. Yuan, J. Nanomater., 2011, 319624, 2011.

[14] D. Yoon, H. Moon, H. Cheong, J. S. Choi, J. A. Choi and B. H. Park, J. Korean Phys. Soc., 55, 1299–1303, 2009.

[15] I. Calizo, I. Bejenari,M. Rahman, G. Liu and A. A. Balandinc, J. Appl. Phys., 106, 043509, 2009.

[16] D. S. Lee, C. Riedl, B. Krauss, K. von Klitzing, U. Starke and J. H. Smet, Nano Lett., 8, 4320–4325, 2008.

[17] A. Das, S. Pisana, B. Chakraborty, S. Piscanec, S. K. Saha, U. V. Waghmare, K. S. Novoselov, H. R. Krishnamurthy, A. K. Geim, A. C. Ferrari and A. K. Sood, Nat. Nanotechnol., 3, 210–215, 2008.

[18] A. Ben Gouider Trabelsi, F. V. Kusmartsev, B. J. Robinson, A. Ouerghi, O. E. Kusmartseva, O. V. Kolosov, R. Mazzocco, M. Gaifullin and M. Oueslati, Nanotechnology, 25, 165704, 2014.

[19] J. Yan, Y. B. Zhang, P. Kim and A. Pinczuk, Phys. Rev. Lett., 98, 166802, 2007.

[20] J. Li, L. Xu, S. Kima and A. A. Shestopalov, J. Mater. Chem. C, 4, 4155–4165, 2016.

[21] S. Nakashima and H. Harima, Phys. Status Solidi A, 162, 39–64, 1997.

[22] J. C. Burton, L. Sun, F. H. Long and Z. C. F. I. T. Ferguson, Phys. Rev. B: Condens.Matter Mater. Phys., 59, 7282–7284, 1999.

[23] S. Heeg, R. Fernandez-Garcia, A. Oikonomou, F. Schedin, R. Narula, S. A. Maier, A. Vijayaraghavan and S. Reich, Nano Lett., 13, 301–308, 2013.

[24] P. A. Temple and C. E. Hathaway, Phys. Rev. B: Condens. Matter Mater. Phys., 7, 3685, 1973.

[25] J. Li, L. Xu, S. Kima and A. A. Shestopalov, J. Mater. Chem. C, 4, 4155–4165, 2016.

[26] D. Yang, A. Velamakanni, G. Bozoklu, S. Park, M. Stoller, R. D. Piner, S. Stankovich, I. Jung, D. A. Field, C. A. Ventrice Jr. and R. S. Ruoff, Carbon, 47, 145–152, 2009.

[27] D. C. Elias, R. R. Nair, T. M. G. Mohiuddin, S. V. Morozov, P. Blake, M. P. Halsall, A. C. Ferrari, D. W. Boukhvalov, M. I. Katsnelson, A. K. Geim and K. S. Novoselov, Science, 323, 610–613, 2009.

[28] C. Faugeras, A. Nerrie´re, M. Potemski, A. Mahmood, E. Dujardin, C. Berger and W. A. de Heer, Appl. Phys. Lett., 92, 011914, 2008.

[29] C. Li, D. Li, J. Yang, X. Zeng and W. Yuan, J. Nanomater., 2011, 319624, 2011.

Chapter 5:

Epitaxial graphene new photo-responses in the visible domain

I- Introduction

Photocurrent in graphene appears owing to hot carriers arising from an optical excitation to energy states greater than the Fermi level. The excited hot carriers are important due to their relaxation via acoustic phonons displaying a bottleneck effect, and via electron-electron scattering creating carrier multiplication which results in a strong decoupling between electron and lattice temperature. On the other hand, photovoltaic effects may also originate due to the thermoelectric effect. Both these photo-responses change under various factors such as the presence of a substrate, the sample geometry, the electrode materials and biasing. This mainly highlights the importance of the present substrate "SiC and SiO_2" to the graphene photo responses, particularly, for the ultrafast domain i.e. terahertz and ultraviolet where a delay appears between the collective behaviour and the photoelectric effect. We revealed new phenomena associated with anomalous photoresistance and photovoltage responses of epitaxial graphene. We present graphene layers grown on 6H-SiC face terminated carbon (6H-SiC (000-1)). The grown layers were unintentionally oxidised with the coexistence of SiO_2 flakes randomly distributed on the termination of the SiC substrate. X-Ray photoelectron spectrometry "XPS", atomic force microscopy "AFM", Raman spectroscopy and magneto-resistance analyses were carried out to illustrate the origin of our discovery.

II- Epitaxial graphene contamination: oxidation and defects localisation

1- XPS measurements

XPS measurements were carried out on epitaxial graphene grown on 6H-SiC (000-1). Oxidised epitaxial graphene were identified using spectrum survey scan. Indeed, figure 1 highlights the most dominant components of epitaxial graphene oxide. We notice SiC substrate and graphene (C1s core level) components (Figure 2-a). The SiC substrate peak appears at 282.38 eV. The C1s spectrum was fitted with three components: the first peak is corresponds to sp^2 hybridised C atoms in graphene sited at 284.41 eV, [1] the second peak is associated with sp^3 hybridised C atoms located at 285.1 eV, and the third peak observed at 286.2 eV is related to the C-O bonds (Figure 2-a). [1-4] The C1s peak illustrates graphene layers across the sample surface. The intensity ratio of sp^3- and sp^2- hybridised carbon components determine the graphene layer number. [2, 5] Here, we found an intensity ratio of sp^3- and sp^2-hybridised carbon components of 0.36 gives. This is a signature of five layers graphene. On other hands, the SiC component is smaller than the main graphene component (C1s) which reveals continuous graphene coverage. Indeed, as the graphene intensity increases the

intensity of the SiC decreases. This is due to the increase of the graphene layers numbers. No buffer layer was observed here due to the face terminated carbon of the studied substrate. The presence of oxygen in this system originates due to the contamination of the graphene layer [1, 4].

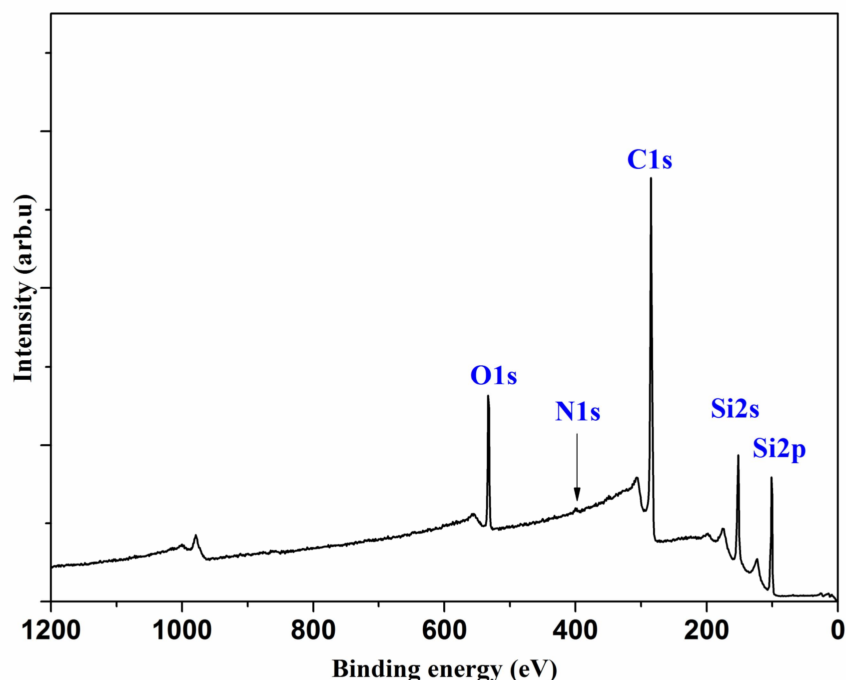

Figure 1: XPS scan survey of epitaxial graphene layers grown on 6H-SiC face terminated carbon 6H-SiC (000-1).

Here, the grown graphene was unintentional oxidised, as reported in previous studies [6]. We located high oxidation of grown graphene layers, where oxygen per cent (at %) reaches 5. This was identified based on the location of both C-O and O=C-O bonds [7]. The oxygen amount present in the graphene layers were inspected (Figure 2-b). We started with the examination of the oxygen peak positioned at 532.33 eV [7]. Its high intensity illustrates the high amount of oxygen in the graphene layers. We further explored the Si2p component located at 100 eV to determine extra Si product or others originating from SiC [6]. We located at 102.5 eV a SiO_2 component [8], illustrating its related flakes on the top layer of the substrate (Figure 2-c). This peak appears due to the high amount of oxygen, which mixes with sublimated silicon atoms trapped on the surface [9]. The unintentional oxidation may occur during earlier steps of our growth. Indeed, it arises occurring the polishing of the residual oxide damage and the native oxide from the substrate. The native oxide rises under the

epitaxial growth process until it reaches an equilibrium state. Nevertheless, we remain unable to specify the associated step inducing this effect.

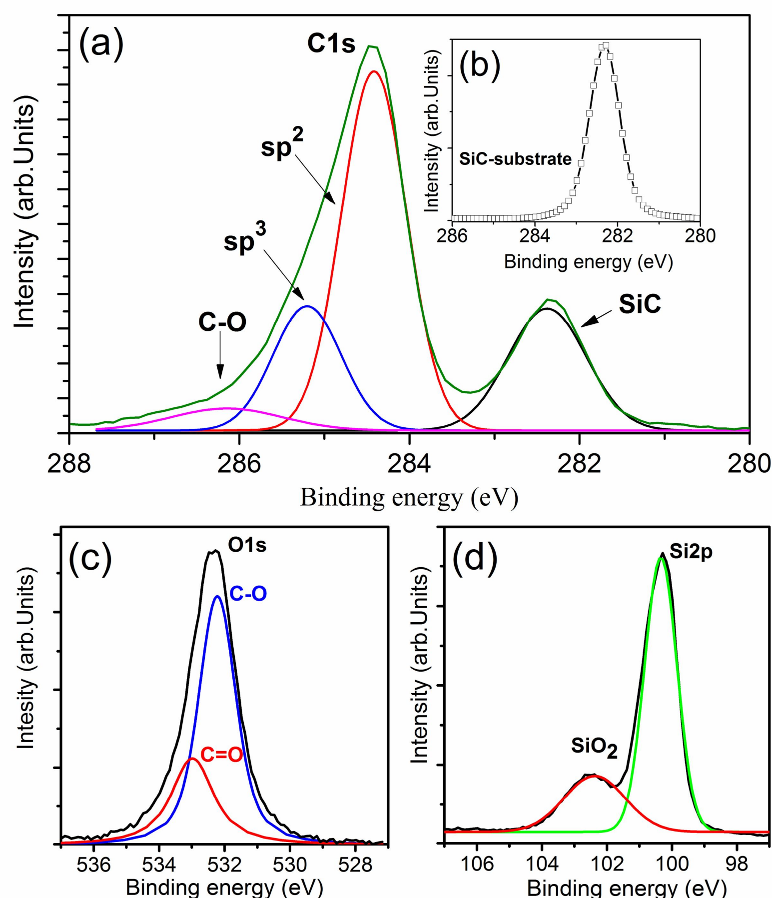

Figure 2: XPS components of epitaxial graphene layers grown on 6H-SiC face terminated carbon 6H-SiC (000-1) respectively a- C_{1s} core level, indicating hybridization sp^2 and sp^3 orbitals, single C-O and Si-C bonds are also shown, b- oxygen levels, deconvolution separates C-O and C=O bond contributions, c-Si2p and SiO_2 peaks.

2- Atomic Force Microscopy

We carried out atomic force microscopy (AFM) measurements in contact mode on our investigated sample in order to analyse graphene layer distribution as well as the surface roughness. Various areas of the sample were considered. In figure 3, we report a typical sample surface of 4.5µm^2 area. The topography of the surface changes across the sample surface to reach a maximum of 1.5 nm (Figure 3-b and 3-c). The high intensities (i. e >1.5nm) correspond to the presence of defects. The height profile varies on the nanometer scale identifying graphene flakes. We located different contrasts from brown to light brown signature of multiple graphene layers inside the flakes. The found graphene layer number

agrees with XPS results. The flake layer numbers and sizes whinge according to its location [10]. Graphene flakes are separated by edge zones, in the proximity of which impurities and defects are often concentrated. The random growth of the graphene layers appearing here represents a common signature of graphene grown on face terminated carbon SiC substrate [10-11]. However, AFM results show preferential orientation in the graphene layer flakes. This is assigned to the terraced of the substrate underneath. In fact, the surface morphology of the substrate influences highly the graphene layer. Thus, imperfection and the flatness of the substrate results plateaus-like features that force particular orientation of the graphene layers. The absence of the buffer layer between the graphene and the substrate as well as the unintentional oxidation of graphene play a further factors on the surface appearance and the distribution of defects and impurities. Indeed, commonly defects are identified using high intensities in the AFM scans (e.g. >1.5nm), where white contrast is found (Figure 3). On other hand, we particularly localise defects near the edge zones of graphene flakes.

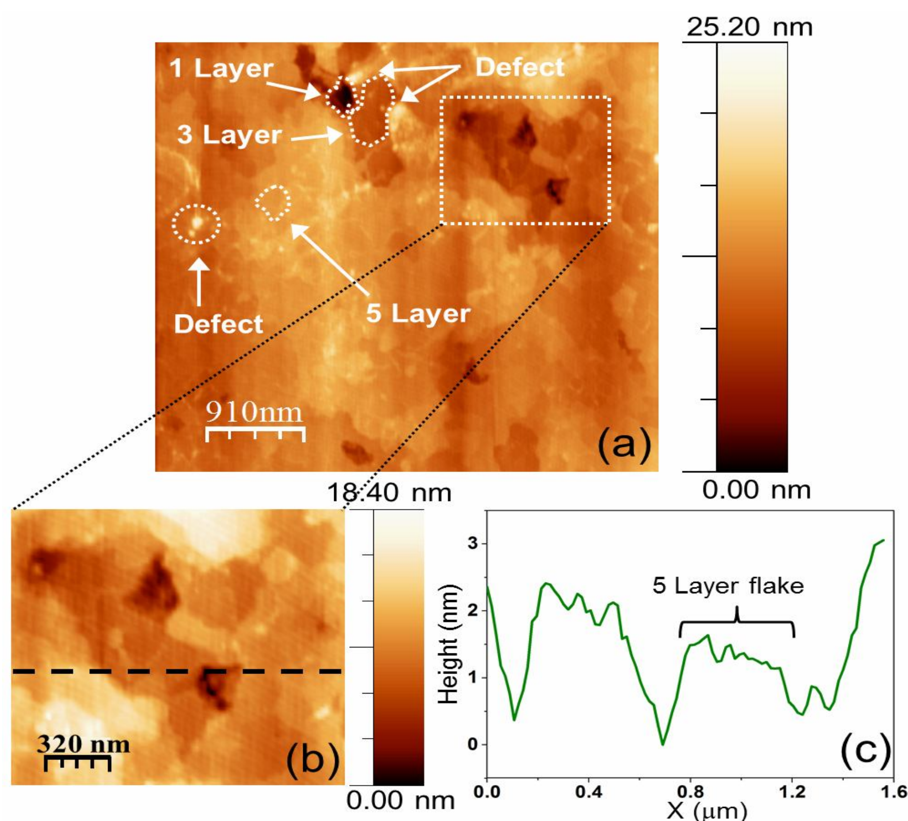

Figure 3: a- AFM measurements of the graphene grown on 6H-SiC (000-1) across a surface area of 4.5x4.5µm reveal the random growth of layers on the sample surface related to the face termination of the substrate. A defect as well as the suggested number of graphene layer flakes (1,3 and 5) are indicated. **b-** Magnification of the AFM image showing two graphene

flakes (layer number -5). **c-** AFM topography image across the 5 Layer graphene flake illustrating homogeneity across a flake. The thickness of the flake corresponds approximately to 5 layers of graphene.

3- Raman mapping investigation

To confirm our results, we further analysed our sample surface morphology using Raman spectroscopy. This helps to determine graphene layer's properties. We represent the Raman mapping in different areas. Indeed, the local Raman spectra identify the homogeneity of the graphene layers. This is based on investigating the amount of defects. We carried Raman mapping using both: small steps of 0.5 µm and an auto-focusing adjustment before each spectrum acquisition. Figure 4 presents the Raman spectra at different points in the sample surface in the frequency range [1000 - 3000 cm^{-1}]. We located graphene Raman modes such as the D, G and 2D bands (Figure 4-a, b, c) [12-14]. G-band is a doubly degenerate (TO and LO) phonon mode at the Brillouin zone centre. The D-band is assigned to phonons on the K point signature of defects [15-16]. The 2D mode is associated to 2TO. We investigated the Raman mapping of the D band. The D-band spectra showed weak intensity (Fig. 4a). This is assigned to oxygen impurities present in epitaxial graphene layers. The enhancement of D-band reflects the structural defects found in epitaxial graphene on face terminated carbon. The local substantial intensity maxima in D-band mapping highlight the structural imperfections.

We investigated graphene layer number distribution across the surface using Raman mapping intensity of the G and 2D bands, respectively, at the frequencies ω_G and ω_{2D} (Figure 4-b and -c). Typically, an I_G/I_{2D} ratio of <0.5 corresponds to single layer graphene (n=1), a ratio of 1.5 relates to four-layer graphene (n=4) and a ratio of 2 denotes five-layer graphene (n=5) [17-18]. The I_G/I_{2D} ratio varies between 0.2 - 4. Various graphene flakes were located, mainly single (n=1), four- (n=4) and five- (n=5) layer coverage was found (Figure 4-d). However, a negligible amount of graphite flakes (I_G/I_{2D} = 2.5, n>5) were also located[18-19]. The mapping intensities illustrates randomly distribution of the graphene flakes. Nevertheless, the graphene quality looks highly homogeneous in each flake. The flakes have common dimensions of 2µm x 2µm. The overlapping graphene flakes supplied the non-homogeneity of the graphene film composition. The flake edges define a different contrast in the intensity maps which define the edge zones between the layers (Figure 4-a). We found large amount of defects appearing close to the edge zones. The obtained results show a good agreement of Raman analyses with the XPS and the AFM data. All characterisation techniques

identify up to five-layered graphene flakes. Particularly AFM measurements demonstrate a random distribution of the graphene layers. However, Raman spectra create a visual map of the defects across the sample surface mainly located at the edge zones of the graphene layers.

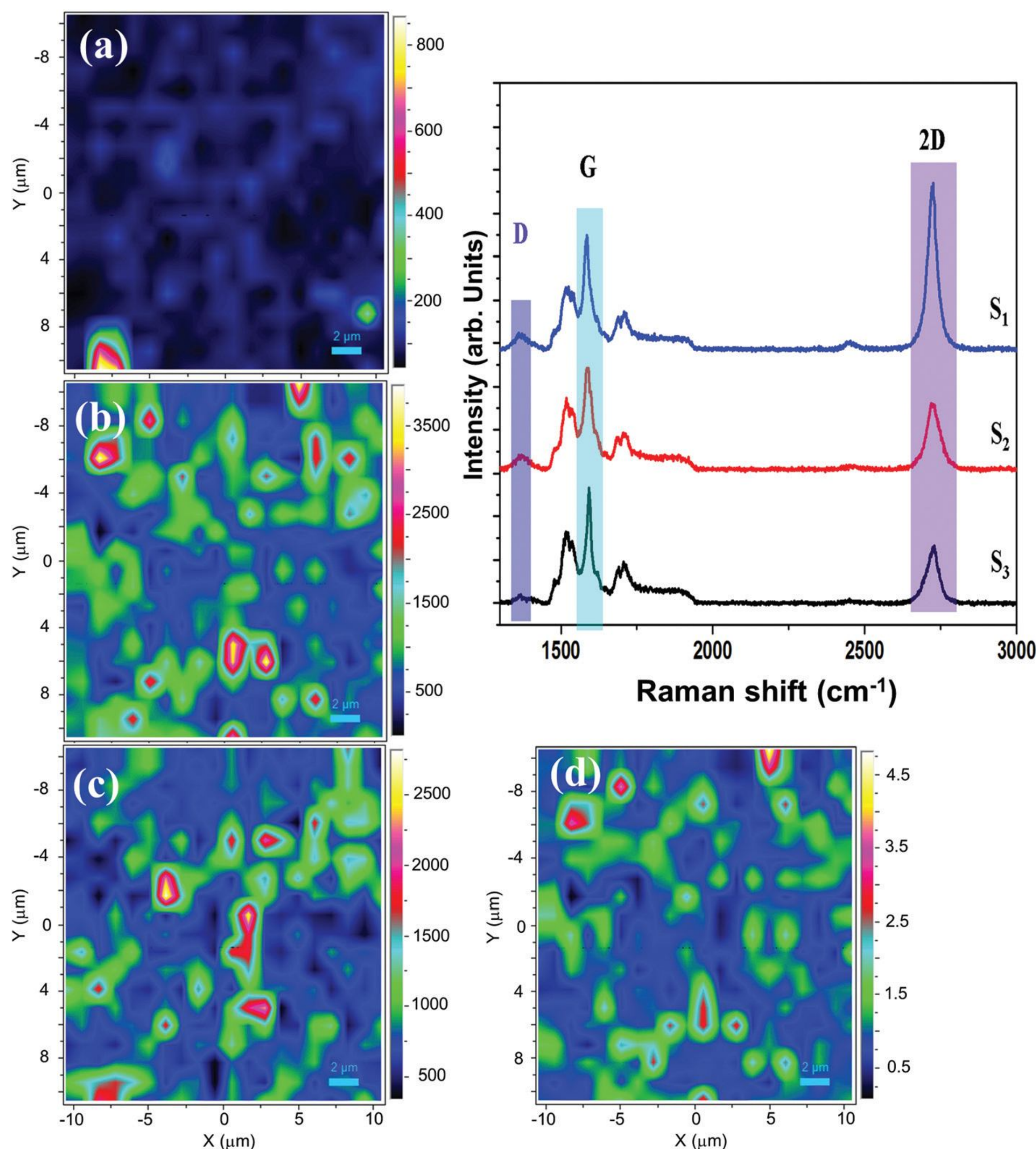

Figure 4: Raman spectra of epitaxial graphene in the frequency range [1000–3000 cm^{-1}] assigned respectively to: S_1 – single layer, S_2 – four layers and S3 – five layers; Raman mapping intensity of a- D band, b- G band, c- 2D band and d- G band normalised by 2D band intensities I_G/I_{2D}. The ratio intensity illustrates the corresponding graphene layer numbers n (intensity ratio < 0.5 implies n = 1, intensity ratio ≈1.5, n = 4).

III- Photo response of epitaxial graphene

1- Epitaxial graphene photoresistance "EGP"

Electrical resistance dependence under continuous light irradiation in epitaxial graphene emerge outstanding physical features. Epitaxial Graphene Photoresistance (EGP) depends on the used light source wavelength. The light illumination has been produced by three lasers of different wavelengths: λ=409 nm (violet), λ=515 nm (green) and λ=625 nm (red), respectively. The dependence of the EGP on time is given in Figure 5-a. To avoid possible heating effect we used lasers having the negligible power (> than 1mW). Photoresistance experiments were investigated using epitaxial graphene grown on 6H-SiC face terminated carbon "6H-SiC (000-1)". We apply van der Pauw method for electrical resistance measurements. We presented the associated optical image of the sample with four contacts (Figure 5-b). EGP clearly appears under the violet light irradiation due to the close photons energy to the gap of the SiC substrate (≈3.03 eV, λ= 409 nm). On other hands, the other two lasers (green and red) photons have smaller energy than the 6H-SiC substrate gap (λ>409 nm). Here, no excitations of electrons in the conduction band and holes in valence band may arise. However, we located an increasing photoresistance as a function of time - although it was much smaller (see, the red and green curves on the Figure 5-a).

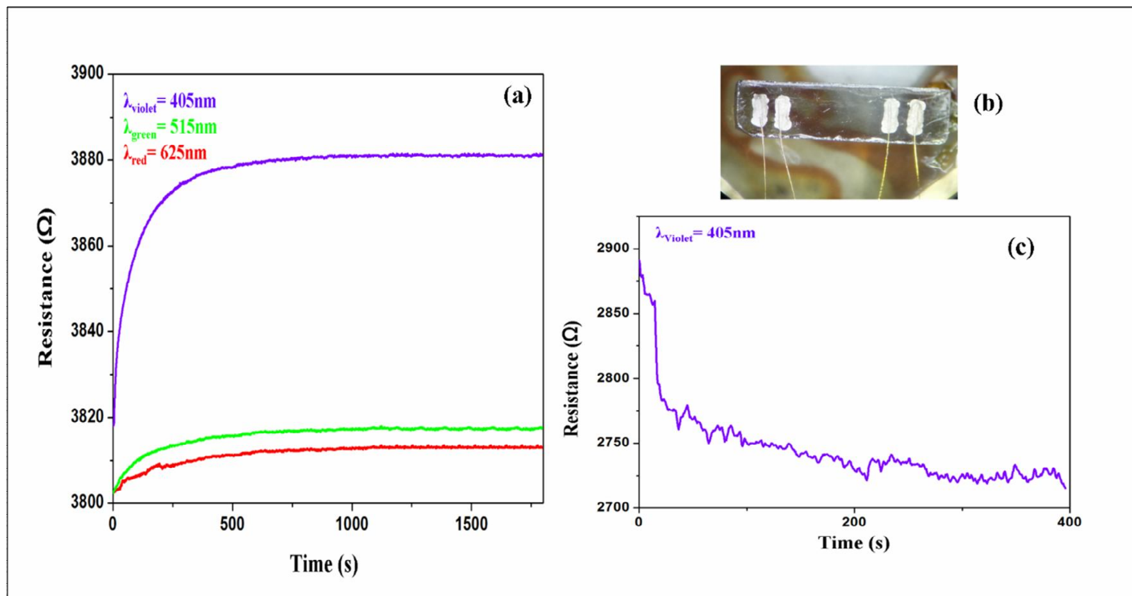

Figure 5: a- The dependence of the photoresistance of epitaxial graphene grown on 6H-SiC face terminated carbon (000-1) on time, under continuous light irradiation: The blue, green and red curves correspond to the different frequencies of the photons, from the violet, green and red lasers, correspondingly; b- Optical image of the sample highlighting the four contact van der Pauw method used in the electrical measurements, c- The dependence of the photoresistance of a 6H-SiC substrate without graphene on time with the same conditions for the light irradiation from a violet laser.

Graphene layers are sensitive to the associated substrate, which force its electrical properties [20-22]. Particular, we believe that photoresistance "PR" generation requires photon energy larger than the SiC bandgap. Insulating substrate possesses impurities and defects that confine electrons and holes in the gap. SiO_2 flakes on the top layer of the substrate act similarly to impurities. They generate a Lifshitz tail in the electron density of states. We concern dopants of energy levels closer to the conduction and valence bands of the SiC substrate. Here, photon energy close to the SiC bandgap is sufficient to activate the PR and electrons supplied the electrical current. Graphene is sensitive to the type of the substrate, where it appears charge redistribution between graphene and substrate. Here, the band structure of the SiC substrate is modified close to the graphene layer. This induces the bending of conduction and valence bands at the vicinity of the graphene which creates the depletion charged area. It provokes an internal electrical field directed perpendicular to the graphene plane. Here, electrons and holes generated by light irradiation are moving in this field in the opposite directions: in the direction and away from graphene or vice versa. The latter depends on the band bending i.e. upwards or downwards with respect to the Dirac point of the graphene layer. The situation recalls the formation of the Schottky barrier on the contact of the semiconductor and metal. Here, electrons and holes are trapped in the charged area. This band bending and Lifshitz tails may effectively reduce the energy gap, with the photons energy close to the substrate gap – as is similar to our case. Indeed, electrons are excited from the valence band under illumination from the light. Epitaxial graphene provides a unique system where there is a strong potential to produce special photoeffects. Indeed, we observe that the EGP varies between 3818 - 3880 Ω. Electrical resistance's change is about 2%, the observed effect is persistent and unexpected. Indeed, the examined graphene photoresponses in literature appear only under excitation energy of 4.7 eV ($\lambda \approx$ 260nm) at the vicinity of M point i.e. ultraviolet and terahertz domain. Our epitaxial graphene effects are opposite to what is expected in the visible domain where resistance change is positive. This varies to the well known behaviour of photoresistance in all existing photo-responsive materials. For the first time for epitaxial graphene, we observe an increase of the resistance under light exposure for the used visible light wavelength (Figure 5-a).

2- Effect interpretation

Photoresistance decreases under light illumination due to an increase in the current carrier density. Such negative photoresistance illustrates to the ordinary response of semi-conductors. We measured such a negative photoresistance for the 6H-SiC (000-1) crystal

under violet laser illumination as reported in Figure 5-c. This highlights how SiC photoresistance without graphene decreases under continuous light excitation. The observed effect is about 6%. This verifies the exposure of the pure substrate to the light enhances the carrier density. This results a spectacular decrease of the resistance. This effect can be simply described using one band Drude model, where the electrons resistance is given by:

$$\rho = \frac{m}{ne^2\tau} \quad (1)$$

n corresponds to the charge carrier density, τ is the scattering time, and m is the electron effective mass.

Under incessant photo-excitation the carrier density n enhanced. This induces a decrease of the resistivity. This indicates a variation of both the effective mass m and scattered time τ. Equation (1) describes the observed PR behaviour of the insulating 6H-SiC (000-1) crystal. This is in a strong dissimilarity to the positive graphene photoresistance (EPG) found for the substrate. That is, the newly discovered EGP reacts in an opposite way. The resistance increases under light excitation [17-18]. Here, together with the current carriers the light irradiation results localised charge centres. They may originate due to trapping of the electrons and holes produced by light by impurities, by defects both in graphene and in SiC and SiO_2 flakes. Indeed, we do not expect a change of the oxygen impurities under light illumination. We examined oxygen percentage before and after light illumination using XPS measurement and no changes were found. Oxidised epitaxial graphene is characterised by a stable state remains consistent under light illumination. In fact, oxygen impurities may localise electrons and therewith induce a high density of negatively charged centres. The current carriers scatter on these centres and the scattering time τ is reduced due to the Coulomb interaction. Here, scattering process create additional resistance for the electronic transport in graphene. Indeed, epitaxial graphene has n-type doping while at the substrate it is unintentionally p-doped. This originates from charge redistribution between the graphene and SiC substrate. The Fermi level of the graphene is located in the band gap of the SiC. Under light illumination, free electrons and holes are formed in SiC. Regarding the field direction in the depletion area near the graphene these electrons or holes may migrate to the graphene layer. This increase or decrease its current carrier density n. This results a change of the Fermi level position in graphene. On other word, if the Fermi level rises a reduction of the resistance is expected. However, the opposite situation is observed here. This unique photoresistance may appear due to two factors: 1- The Fermi energy in graphene is reduced; 2- The creation of a new scattering mechanism under light irradiation. The excited electrons are trapped close

or inside in the graphene layers, which separated them from the holes created by light. Consequently, it appears a charge centres which will scatter charge carriers and resulting a short scattering time τ. The morphological imperfection of epitaxial graphene layers, such as: impurities, defects, different grain sizes and edge zones between the layers, act as traps for electrons or holes. These imperfections capture electrons or holes and induce new scattering mechanism that accordingly results in the novel EGP response. Furthermore, the presence of small insulated SiO_2 flakes form barriers for electron migration from the substrate to graphene. Moreover, they help in the formation of the charge redistribution between graphene and the substrate. These charge centres scatter the charge carriers and favour the EPG. Furthermore, the unintentional oxidation of the graphene films contributes on this effect. Oxygen impurities inside the system isolate excited electrons and holes from each other. This forms some charged scattering centres. This reduces both the scattering time and the resistance. Figure 6 describes the resistance enhancement mechanism for monolayer graphene, which could be generalised for various graphene layer numbers.

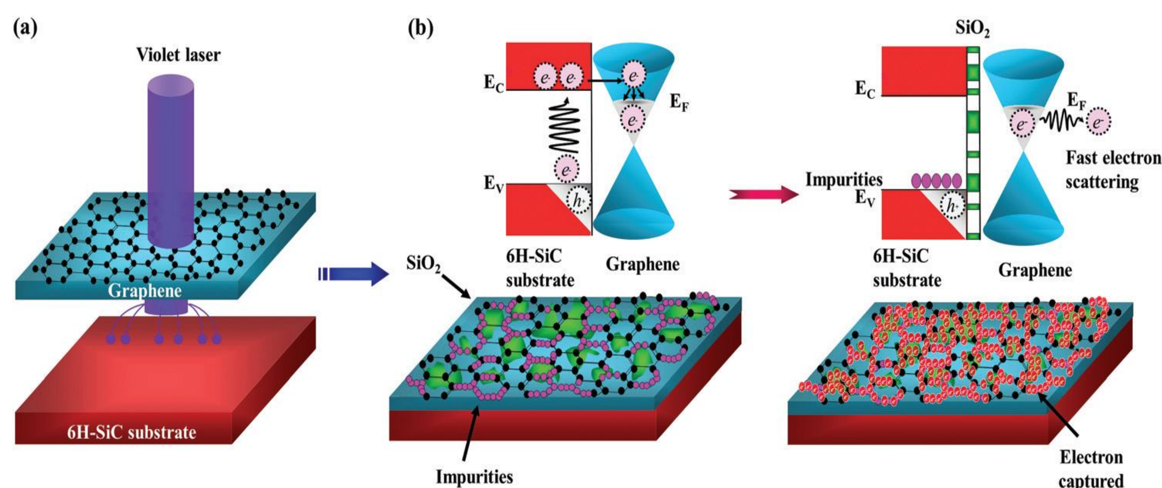

Figure 6: Photoresponse process: a- initial state of epitaxial graphene i.e. at equilibrium, b- violet laser irradiation of the sample surface, creating charged centres on impurities and defects, leading to the trapping and scattering of electrons and holes. The modified band structure and unconventional electron transport result in novel photoresistance and photovoltage effects.

The oxygen contribution was checked using ordinary epitaxial graphene sample grown on 4H-SiC face terminated carbon (4H-SiC (000-1)). We present photoresponse of non-oxidised layers (n>5) of epitaxial graphene grown on 4H-SiC (000-1) (Figure 7). We investigated photoresistance. Nevertheless, no increase of resistance was observed and similar behaviour to the majority of semiconductors was established. Here, the photoresistance in epitaxial graphene grown on 4H-SiC (000-1) decreases. This reveals the impact of the

presence of oxygen impurities on the photoresistance. The both samples are grown on face terminated carbon that has the same morphological imperfections. However, only the presence of oxygen results contrary behaviour to the ordinary case of epitaxial graphene grown on face terminated carbon. This shows the effect of oxygen atoms on the photoresistance. On the other hand, the morphological imperfections of the face terminated carbon partially contribute in the located photo effects. Oxygen impurities are placed at the edge zones of the layers, which increases the local amount of defects, as observed in AFM and Raman measurements. The increase of the photoresistance response is detailed with the Drude model. The resistivity is given also by equation (1). The scattering time τ could be given by:

$$1/\tau=1/\tau ee+1/\tau le, \quad (2)$$

τ_{le} is the time associated with the scattering on the charge centres and τ_{ee} is the scattering time of the charge carriers when only the charge density changed with the light or due to electron-electron interaction. The τ_{le} is determined using the scattering theory which is proportional to the charges of impurity centres over the square of the energy of the charge carriers. 47 This latest could be very large when energy decreases, that is, when we are moving to the Dirac point having zero energy. Consequently, the estimated cross section is very large and the associated value τ_{le} can be very small. Substituting this shortest scattering time into the equation (2), we obtain very short total scattering time τ. Furthermore, the resistivity of the system increases by substituting the obtained value in equation 1. This verified our suggestion regarding the increase of photoresistance in epitaxial graphene due to the creation of the charge centres.

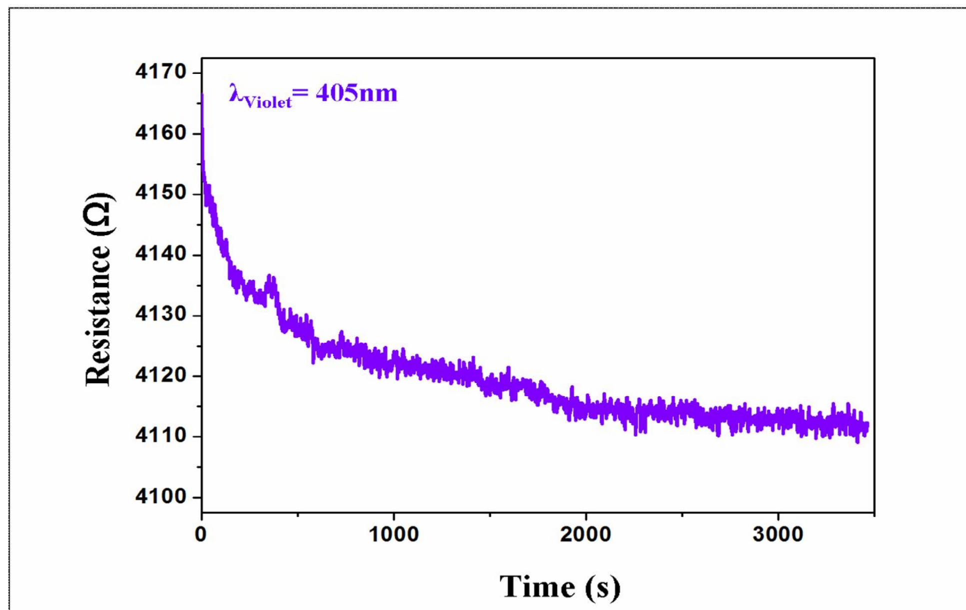

Figure 7: Photoresistance of five layers of epitaxial graphene grown on face terminated carbon - 4H-SiC (000-1) - under violet laser excitation.

3- Temperature Dependent Resistance Measurements

We investigated the epitaxial graphene temperature dependent resistance "EGTDR" to demonstrate our found (Figure 8). The EGTDR was determined based on a pulse tube cryo-cooler. The resistance displayed a descending tendency, where it decreases from [6828 – 3841 Ω] as the temperature range increases between [4–300 K]. The resistance variation was about 40%, which is a huge variation. Such EGTDR variation is distinctive. Commonly, the maximum temperature dependence of graphene is usually about 7%, except for graphene quantum dots where a giant variation also appears [23]. As temperature decreases the number of excited electrons decreases while resistance increases. The high roughness of epitaxial graphene results diverse domain sizes i.e. grains. This appears more for the face terminated carbon, where various numbers of layers may exist in the same area (Figure 3). The different grain sizes and graphene layer flakes enhance local impurity effects due to oxygen, and defects. The presence of SiO_2 flakes in-between the graphene layers and at the top layer of the SiC substrate increases morphological imperfections. Different resistive interface regions produced at the edges of the graphene layers where high impurities amount exist [24]. On other hands, excited electrons are Stokesed at the boundary interface in low temperature. Consequently, the scattering time of mobile electrons on these trapped charges is very small. The accumulation of charges increases the resistance of the system when the temperature is going down (Figure 7). This indicates important role of the local impurities in the observed resistance depending on the temperature behaviour. The EGRDR obtained here is similar to a semiconductor. However, its photoresistance signal differs to that of semiconductors i.e. 6H-SiC. Therefore, the analysis of correlations between the photoresistance and resistance dependent temperature measurements may shed light on the origin of the obtained behaviour, which is mainly associated with the epitaxial graphene layers.

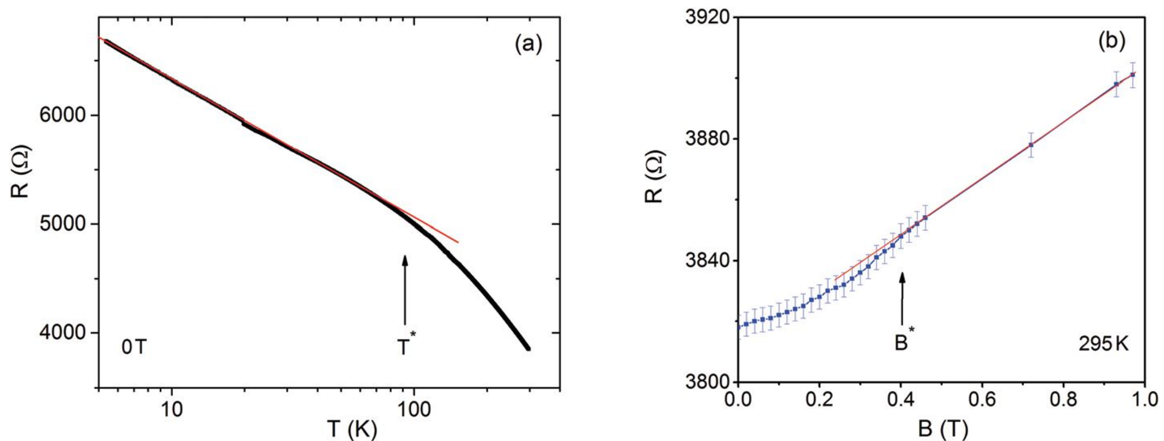

Figure 8: a- Temperature dependence of the resistance in non-illuminated epitaxial graphene layers grown on 6H-SiC (000-1) between [4-300 K]. At low temperature 4–100 K the resistance follows a strong logarithmic behaviour. The crossover temperature T* characterising the deviation from the logarithmic dependence is indicated and corresponds approximately to $T^* \approx 100$ K. b- Magnetoresistance in epitaxial graphene at 295 K in a magnetic field between 0–1 T. Until a field of $B^* \approx 0.4$ T the magnetoresistance is quadratic in field. The logarithmic low-temperature resistance as well as the quadratic magnetoresistance are consistent with the Altshuler–Aronov effect. Surprisingly for fields exceeding $B > 0.4$ T the magnetoresistance changes to a pronounced linear dependence.

4- Photovoltage "PV"

Motivated by the unique photoresistance response, we have examined the photovoltage effect, focusing specifically on the epitaxial graphene photovoltage time dependence "EGPVTD". To the best of our knowledge the EGPV was not reported so far in the literature. The photovoltage responses investigated here were measured only under violet laser (λ=409 nm) illumination. Figure 9 depicts the EGPVTD signal recorded with (on) and without (off) photo-excitation. The EGPVTD response varies about 6×10^{-7} V. Here, electrons are excited from surface states towards the conduction band, which decreases the deflection of bands in the surface region. These electrons, after reaching the conduction band of the SiC substrate, pass to the graphene layers to occupy new levels of energies. This in turn causes an increase in the PV value [18]. Excited electrons try to reach a quasi-equilibrium state inside the system. Here, the photovoltage value becomes constant. This was demonstrated during our EGPVTD measurements (Figure 9). In fact, the EGPVTD signal reaches the maximum voltage average when the photo-excitation is on. However, the maximum voltage is not stable. It fluctuates until the system reaches its stable state. These fluctuations could also be associated with the trapping of electrons by impurities, until all the electrons find their equilibrium. A quasi-periodic EGPV signal behaviour was observed on many time intervals, such as 60s, 200s and 1500s. Nevertheless, photo-voltage stabilised after 1500s, illustrating a quasi-equilibrium state. This quasi-equilibrium state is verified from the EGPR measurements, where resistance reaches its maximum after some finite time (Figure 9). However, the fluctuations of the excited electrons that stimulate the photo-responses change are better seen with EGPVTD measurements.

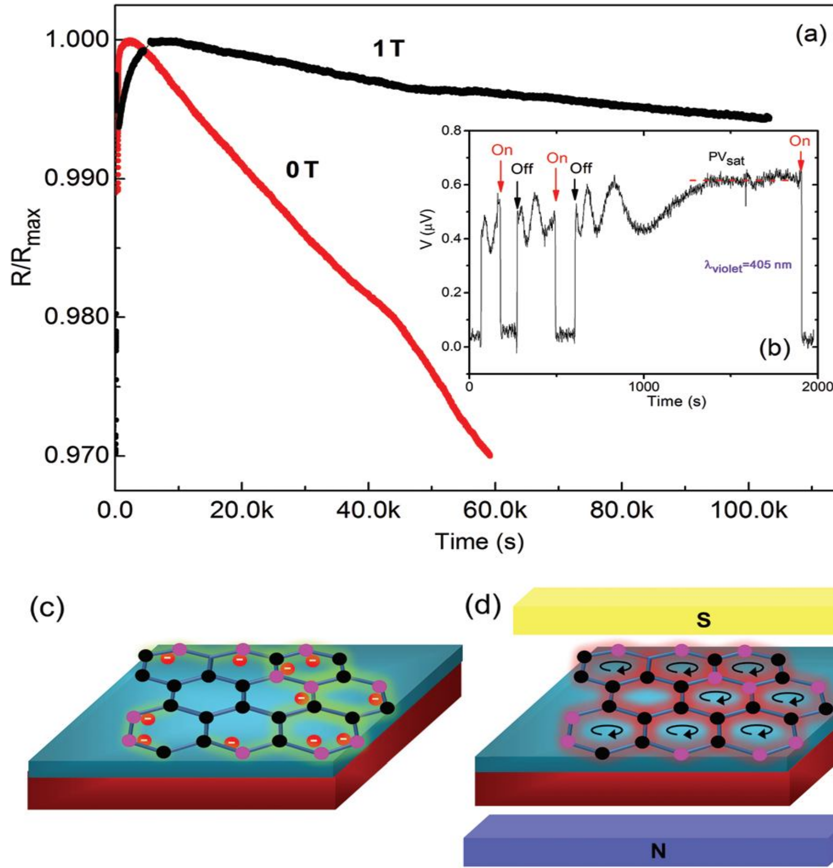

Figure 9: a- Photoresistance decay time without a magnetic field effect (B = 0 T) and with magnetic field (B = 1 T). b- Photovoltage measurements of epitaxial graphene layers grown on 6H-SiC (000−1) under violet laser excitation. The red lines indicate the case of the laser (on), while black lines correspond to the switch off of the laser. The saturation voltage reaches values of PVsat ≈ 0.6 μV for λ = 405 nm laser. c- Excitation of electrons from the EV to EC of the 6H-SiC substrate and migration of the electrons to the graphene layers (locations of vacancies/impurities are indicated in pink). d- Trapping of holes by vacancies and impurities which induces persistent currents around flake edges and correspondingly a short transport relaxation time τtr under a magnetic field. Together, these lead to positive magnetoresistance and considerably slowed decay times in magnetic fields as shown in (a).

5- Magnetic dependence of photo resistance decay

To determine a consistent description of the impurities (defects)-related lifetime degradation, we studied epitaxial graphene photoresistance decay under magnetic fields (Fig. 8a). These measurements show an electron recombination process strongly depends on the applied magnetic field. Resistance variation under the influence of an applied magnetic field was considered. First, we illuminate the sample surface using violet laser until reaching a stable value of the resistance. Here, the resistance decay was recorded as the light turned off in two cases: 1- without the magnetic field and 2- with a high magnetic field B=1 T. These two cases have very different time-dependent behaviour. The photoresistance excitation and decay is presented in Figure 8. We have

described the photo-excitation of epitaxial graphene above. However, we limited our investigation to the relaxation process occurring in these cases with and without magnetic field. Without the magnetic field the relaxation time is relatively shorter and excited electrons recombine faster. We notice a long relaxation time ($\tau \approx 17$ hours) in comparison to an ordinary semiconductor. This long decay time of the excited charge carriers in the graphene layers is assigned to lattice defects, including the surface states. Here, electrons can not recombine directly, especially with the current morphological properties of epitaxial graphene. This illustrates the existence of various relaxation processes. Epitaxial graphene is characterised by its roughness, high amount of defects, high oxygen impurities and grain boundaries between the graphene flakes. These latest increases the electron life-time in the graphene layers. Thus, the decay time or the process of the photoresistance decay observed under a magnetic field is much longer than that without the magnetic field. Magnetic field has a dramatic influence on graphene flakes, where graphene flakes transform into topological insulators under its presence [24-26]. The topological state is characterised by the formation of persistent currents on flake edges[52] and the corresponding opening of an insulating gap inside their bulk. Because of this gap in the energy spectrum the relaxation is slowed down. In the bulk the charges are localised and resist taking part in the recombination process. Here photoresistance decay is mainly associated with non-uniform edge persistent currents where the mobile charge carriers are concentrated near the flake edges (Fig. 9-c and 9-d). Therewith, the magnetic field then slows down the recombination processes between the electrons and holes. Thus because of the complex topology of the edge persistent currents, the relaxation process cannot be generally described by a single exponential function. This is also the case for zero magnetic fields. In both cases a decay of photoresistance follows some power-law (or linear), function which cannot be described by a single relaxation time. We do not consider the decay shape or details of the decay process. Here, magnetic measurements highlight the role of the morphological imperfections in epitaxial graphene. The observed behaviour demonstrates the dramatic reduction of the charge recombination rate under a magnetic field. This is expected due to the graphene flakes are topologically insulating. The photoresistance decay lasts significantly longer. Under the magnetic field the edge currents are formed or enhanced. Mobile electrons are expelled from the bulk to the edges of the graphene flakes, where most of the defects exist [25-27]. The magnetic field arises the Coulomb interaction between excited electrons

and separates hole and electron charge carriers. Both factors slow down the recombination rate between holes and electrons, leading to longer decay times τ. Other elementary excitations, like phonons, may need to be included to attain fuller understanding of the mechanisms involved.

On other hand, similar transformation of the graphene flakes into topological insulators is responsible for the magnetoresistance (MR) observed here (Figure 8-b). It appears that the MR increases nearly linearly when the magnetic field rises from 0.4 to 1 T. This behavior is associated with the creation of persistent currents which form a nontrivial topology. In fact, such a linear increase of the MR may be associated with a formation of a two phase system [19]. These latest are dictated by the nature of the topological insulator created from graphene flakes by magnetic field. The bulk of the flake is insulating and the edges are conducting. We notice that magnetoresistance and photo-resistance decay time measurements are complementary. They highlight the nontrivial effects and the photo-physical properties of epitaxial graphene.

5. Conclusions

We revealed new photoresistance and photovoltage responses in epitaxial graphene grown on 6H-SiC face terminated carbon (6H-SiC (000-1)). We showed for the first time an increase of epitaxial graphene photoresistance under light illumination. The detailed measurements were done for a violet laser of wavelength λ= 409 nm due to its close energy to the 6H-SiC substrate gap. We have observed the most prominent photo-response in graphene grown on C-terminated 6H-SiC substrate, which we believe to be due to the non-trivial roughness of its surface topology. We argue the observed effects with the morphological imperfections characterising epitaxial layers grown on face terminated carbon. Our findings will attract attention for photovoltaic applications of the epitaxial graphene oxide grown on face terminated carbon, despite its random growth and well-known imperfections. We have shown that the morphological texture is responsible for the creation of the unique photo effects. These stable, long-lifetime phenomena create the possibility for using epitaxial graphene in new photo detector technologies.

References

[1] A. C. Ferrari, J. C. Meyer, V. Scardaci, C. Casiraghi, M. Lazzeri, F. Mauri, S. Piscanec, D. Jiang, K. S. Novoselov, S. Roth and A. K. Geim, Phys. Rev. Lett., 97, 187401; 2006.

[2] Z. Luo, T. Yu, K.-J. Kim, Z. Ni, Y. You, S. Lim, Z. Shen, S. Wang and J. Lin, ACS Nano, 3, 1781–1788, 2009.

[3] N. Z. Wang and J. Liu, Appl. Phys. A: Mater. Sci. Process., 105, 341–345, 2011.

[4] A. Ben Gouider Trabelsi, F. V. Kusmartsev, D. M. Forrester, O. E. Kusmartseva, M. B. Gaifullin, P. Cropper and M. Oueslati, J. Mater. Chem. C, 4, 5829–5838, 2016.

[5] C. Li, D. Li, J. Yang, X. Zeng and W. Yuan, J. Nanomater., 2011, 2011, 319624.

[6] C. Yan, J. Wang and P. S. Lee, ACS Nano, 9(2), 2130–2137, 2015.

[7] K. J. Tielrooij, L. Piatkowski, M. Massicotte, A. Woessner, Q. Ma, Y. Lee, K. S. Myhro, C. N. Lau, P. Jarillo-Herrero, N. F. van Hulst and F. H. L. Koppens, Nat. Nanotechnol., 10, 437–443, 2015.

[8] R. L. Liboff, Introductory Quantum Mechanics, Addison-Wesley, p. 805, 1998.

[9] Y. Liu, Z. Liu, W. S. Lew and Q. J. Wang, Nanoscale Res. Lett., 8, 335, 2013.

[10] J.-H. Chen, L. Li, W. G. Cullen, E. D. Williams and M. S. Fuhrer, Nat. Phys., 7, 535–538, 2011.

[11] Y. Gong, M. Long, G. Liu, S. Gao, C. Zhu, X. Wei, X. Geng, M. Sun, C. Yang, L. Lu and L. Liu, Phys. Rev. B: Condens.Matter, 87, 165404, 2013.

[12] B. L. Altshuler, A. G. Aronov and P. A. Lee, Phys. Rev. Lett., 44, 1288–1291, 1980.

[13] A. A. Kozikov, A. K. Savchenko, B. N. Narozhny and A. V. Shytov, Phys. Rev. B: Condens. Matter, 82, 075424, 2010.

[14] B. Jouault, B. Jabakhanji, N. Camara, W. Desrat, C. Consejo and J. Camassel, Phys. Rev. B: Condens. Matter, 83, 195417, 2011.

[15] S. Lara-Avila, A. Tzalenchuk, S. Kubatkin, R. Yakimova,T. J. Janssen, K. Cedergren, T. Bergsten and V. Falko, Phys. Rev. Lett., 107, 166602, 2011.

[16] J. Jobst, D. Waldmann, I. V. Gornyi, A. D. Mirlin andH. B. Weber, Phys. Rev. Lett., 108, 106601, 2012.

[17] J. Jobst and H. B. Weber, Nat. Phys., 8, 352–352, 2012.

[18] C. Berger, Z. Song, X. Li, X. Wu, N. Brown, C. Naud,D. Mayou, T. Li, J. Hass, A. N. Marchenkov, E. H. Conrad, P. N. First and W. A. de Heer, Science, 312, 1191–1196, 2006.

[19] S. A. Bulgadaev and F. V. Kusmartsev, Phys. Lett. A, 342, 188–195, 2005.

[20] K. V. Emtsev, A. Bostwick, K. Horn, J. Jobst, G. L. Kellogg, L. Ley, J. L. McChesney, T. Ohta, S. A. Reshanov, J. Röhrl, E. Rotenberg, A. K. Schmid, D. Waldmann, H. B. Weber and T. Seyller, Nat. Mater., 8, 203–207, 2009.

[21] A. O′Hare, F. V. Kusmartsev and K. I. Kugel, Nano Lett., 12, 1045, 2012.

[22] A. Ben Gouider Trabelsi, F. V. Kusmartsev, B. J. Robinson, A. Ouerghi, O. E. Kusmartseva, O. V. Kolosov, R. Mazzocco, M. Gaifullin and M. Oueslati, Nanotechnology, 25, 165704, 2014.

[23] B. L. Altshuler and A. G. Aronov, in Electron-Electron Interactions in Disordered Systems, ed. A. L. Efros and M. Pollak, North Holland, p. 628, 1985.

[24] V. Krstic, D. Obergfell, S. Hansel, G. L. J. A. Rikken, J. H. Blokland, M. S. Ferreira and S. Roth, Nano Lett., 8, 1700–1703, 2008.

[25] Y. Liu, R. P. Tiwari, M. Brada, C. Bruder, F. V. Kusmartsev and E. J. Mele, Phys. Rev. B: Condens. Matter, 92,235438, 2015; (also see the references therein).

[26] D. M. Forrester and F. V. Kusmartsev, Nanoscale, 6, 7594–7603, 2014.

[27] F. V. Kusmartsev, Phys. Rev. B: Condens. Matter, 52,14445–14456, 1995.

Conclusion

Conclusion

The first part of this report presented generalities on the physical properties of graphene and its applications. We have shown the properties of graphene epitaxy and the interest of its realization for the electronic and optoelectronic applications taking into consideration these two polarities. The graphene developed in the framework of this thesis is characterized by techniques presented in chapter II.

We studied the optical properties of the different poly-type SiC substrate. We distinguished each SiC poly-type using its first-order Raman modes observed between [100-1000 cm^{-1}]. SiC polytypes are characterized with a set of Raman modes. The Raman modes correspond to the 3C-SiC (100) / Si (100) are the T_2 (TO) and T_2 (LO) which appear respectively in 796.55 cm^{-1} and 972.41 cm^{-1}. The main Raman modes of the 4H-SiC are located at 270, 770, 791, 967 cm^{-1}, they are assigned to E_1 (low), E_2, E_1 (TO), A_1 High), A_1 (low) and A_1 (high), respectively. The signature Raman modes of 6H-SiC are E_2, E_2, E_1 (TO), A_1 (LO) observed respectively at 765, 787, 795, 964, 154, 245, 507 and 516 cm^{-1}. The Raman characterization of the first order modes of each polytype ensures better identification of all structural changes during graphitization processes. On other hands, we distinguished the Raman mode of graphene in the frequency range between [1000-3000 cm^{-1}]. We localise the D, G, 2D G* and (D+G) modes.

On other hands, we give an experimental proof of epitaxial layer changing into bubbles and domes existing on graphene intrinsically grown on 4HSiC face terminated carbon. Theses structures have been sited using optical microscopy, AFM, UFM and Raman mapping. The use of UFM also helped us to measure the nanomechanical stiffness of these dome and bubble structures. Our Raman analysis showed no dependence on the strain effect. Moreover, we have noted strong charge redistribution between the graphene layer and the rest of the substrate. For the first time, we give in detail the doping distribution inside the intrinsically grown epitaxial bubbles. The charged nature of these domes and bubbles may arise a local mini gap in the electronic spectrum. The minigap may also influence electron mobility.

Furthermore, we illustrated a spontaneous charged quantum capacitance in epitaxial graphene grown on 4H–SiC face terminated carbon. We found a capacitance originating of mutual charge redistribution between graphene and the substrate. The associated capacitance consists of both quantum and classical capacitance. The formation of the quantum capacitor is associated with the spatial separation of the graphene layer from the rest of the 4H-SiC (000-1)

doped substrate. The found capacitor was self-charged and a mini-band gap has been determined. This opens a new direction for the study of self-created capacitor effects and their associated gap openings. Furthermore, new approach has been used A1 (LO) phonon–plasmon coupled modes ‘‘LOPPC’’ of 4H–SiC substrate have been investigated. Such a coupling strongly depends on substrate doping. Thus, a non-invasive characterisation of the charge density distribution in a graphene-substrate system has been developed.

Moreover, we have revealed new photoresistance and photovoltage responses in epitaxial graphene grown on 6H-SiC face terminated carbon (6H-SiC (000−1)). Indeed, we showed a particular of epitaxial graphene photoresistance increasing under light illumination. Full study was done for a violet laser of wavelength $\lambda = 409$ nm due to its close energy to the 6H-SiC substrate gap. We have observed the most prominent photo-response in graphene grown on the C-terminated 6H-SiC substrate, which we may assign to the non-trivial roughness of its surface topology. We argue that the observed effects are associated with the morphological imperfections characterising the epitaxial layers grown on face terminated carbon. Here a range of measurement techniques were used: X-ray photoelectron spectrometry, atomic force microscopy, Raman spectroscopy, and magneto-photoresistance decay analyses. We expect that our findings may attract attention towards photovoltaic applications of the epitaxial graphene oxide grown on face terminated carbon, despite its random growth and well known imperfections. Here, we have shown that its morphological texture is responsible for the creation of its unique photo-effects. These stable, long-lifetime phenomena create the possibility of using epitaxial graphene in new photo-detector technologies.

Finally, we developed a complete study of epitaxial graphene. We revealed, for the first time, unique properties such as: mechanical properties, new epitaxial graphene structures like bubbles and domes, new approach based on substrate characteristic to determine the density of charge and the phonon plasmons coupling and new photoresponse of epitaxial graphene.

Publications List:

1- Morphological imperfections of epitaxial graphene: from a hindrance to the generation of new photo-responses in the visible domain, **A. Ben Gouider Trabelsi**, F. V. Kusmartsev, M. B. Gaifullin, D. M. Forrester, A. Kusmartseva and M. Oueslati, ***Nanoscale***, c6nr08999b, 2017.

2- The emergence of quantum capacitance in epitaxial graphene, **J. Mater. Chem. C,** 2016, C6TC02048H. **A. Ben Gouider Trabelsi**, F. V. Kusmartsev, D. M. Forrester, O. E. Kusmartseva, M. B. Gaifullin, P. Cropper and M. Oueslati.

3- Charged nano-domes and bubbles in epitaxial graphene, ***Nanotechnology*** 25 (2014) 165704 (16pp), ***IOP Publishing.*** **A. Ben Gouider Trabelsi**, F. V. Kusmartsev, B. J. Robinson, A. Ouerghi, O. E. Kusmartseva, O. V. Kolosov, R. Mazzocco, Marat Gaifullin and M. Oueslati.

4- Raman spectroscopy of four epitaxial graphene layers: Macro-island grown on 4H-SiC (000-1) substrate and an associated strain distribution, ***Thin Solid Films*** 539 (2013) 377–383**. A. Ben Gouider Trabelsi**, A. Ouerghi, O.E. Kusmartseva, F.V. Kusmartsev, M. Oueslati